

Electromechanical investigations and quench experiments on sub-size HTS cables for high field EU-DEMO Central Solenoid

Présentée le 27 avril 2022

Faculté des sciences de base
SPC - Groupe Supraconductivité
Programme doctoral en physique

pour l'obtention du grade de Docteur ès Sciences

par

Ortensia DICUONZO

Acceptée sur proposition du jury

Prof. H. Brune, président du jury
Prof. A. Fasoli, Dr D. Uglietti, directeurs de thèse
Dr V. Corato, rapporteuse
Dr R. Heller, rapporteur
Prof. I. Furno, rapporteur

Acknowledgements

During these years, I grew up a lot, thanks to work-related and personal challenges.

Without the support of the people that were with me during this journey, it would have not been the same.

Thanks Davide, for your patience in supervising me, and especially for your very close support during the writing of this thesis. Thanks to you, I have finally acquired some experimental knowledge. I am very grateful for your bold mindset: I have learnt a lot, from the scientific and personal point of view.

Thanks Ambrogio, because feeling your trust in me, when I did not have it, I have felt more confident.

Thanks Pierluigi, for your technical suggestions, and to have shared your human side when I needed it.

Thanks Kamil, for your kindness and your essential support with the THEA code.

Thanks Andrea, for your discussion about the Quench Experiment. It was cool this “back-to-university” feeling.

Thanks to all the people on the first floor, for the vibrant scientific discussion, the professional support and for the cozy time spent together outside the office, in front of a beer or cheering up the Switzerland team during the world cup.

Merci viel mal to all the technicians and SULTAN operators: with you I had a deep immersion of the real and tangible experimental life. Thanks for the great support during the Quench Experiment.

Thanks to all the friends, who remained until the end and who did not. With all of you, I had a lot of fun and I shared the lightheartedness that I welcomed in my life.

Thanks to Miren, Vlad and Thibault for the shared home-office: without you, I would have been just office without the warmth of home.

Thanks Chiara and Lidia, for the deep and brave discussions about the meaning of life. I am very lucky to have met two souls like you.

Thanks to my family, for your unconditional love and trust in me.

Thanks to Thibault. My life shines with adventures and passion every day with you.

And thanks to me: I was courageous enough to start to look at the complexity of life with curiosity and a gentle smile.

Abstract

The aim of this thesis is to investigate the mechanical and thermal behaviour of HTS coated conductor cables for EUROfusion DEMO magnets.

One of the issue in large HTS magnets is the safety against a quench. A quench is a sudden thermal runaway in which the energy stored in the magnet is turned into heat in a localized volume of the magnet. If no countermeasures are applied, the localized temperature increment might damage the magnet. A Quench Experiment has been carried out to provide experimental data on the full quench evolution in sub-size HTS cables for fusion application. The SULTAN facility has been upgraded, replacing the superconducting transformer with current leads connected to a 15 kA power supply. This upgrade allows us to provide large power to the conductor for indefinite time. Previously, the maximum power was limited to few W for few seconds. Four different sub-size conductors designed for the Central Solenoid magnet of EU DEMO have been fabricated with REBCO coated conductors. All the cables are based on a triplet of round strands, each strand is composed of two half-round copper profiles surrounding a stack of tapes. The copper profiles and the tapes are soldered together. The triplet is insert in steel jacket to obtain forced-flow conductors. The quench is triggered by sending hot helium in the conductor and the temperature evolutions of the conductor components (jacket, helium) have been measured up to temperatures of 150 K. Due to the gradients between cable, He and jacket, the maximum estimated temperature value on the cable is above 200 K, depending on the specific cable design. The experimental results of the different conductors have been interpreted with the support of a multi-physics code (THEA). It has been seen that decreasing the transverse thermal resistance between strand and jacket of one order of magnitude (from 0.2 to 0.03 Km/W) leads to a decrease in the temperature rise rate from tens of K/S to just few K/s: the heat produced in the cable can be better absorbed by the large thermal inertia of the jacket. The he multi-physics model indicates that, in case of the quench is caused by hot helium flow, the voltage rises much faster in case of homogenous magnetic field, leading to a lower hot spot temperature at the quench detection.

The combination of large current and high magnetic field results in very large transverse stress on the cable during the magnet operation. The superconducting ceramic material is brittle, and the mechanical limit for coated conductors depends widely on the direction of the force. When the limit is exceeded, the current carrying ability of the cable is compromised. In the second part of the thesis the critical transverse pressure at which the performance of the cable is decreased is quantified. Various round strands were fabricated, exploring different reinforcement options. The critical transverse pressure is measured on a strand by testing it at liquid nitrogen temperature, applying the force thanks to an anvil. The measured critical transverse pressure values indicate which strand designs should be discarded, i.e. when the measured critical transverse pressure values are lower than the nominal ones foreseen in the full cable design. For one of the reinforcement options, a finite element mechanical model was developed to better understand the mechanics and to propose improvement to the cable design. It was found that the performance might be improved by wrapping the strand with a wire whose thermal expansion coefficient is higher than the one of copper. In this way, the strand is pre-compressed during the cool down and the tensile stress that might cause the rupture of the REBCO tapes is decreased.

Keywords: Coated Conductors, Quench Experiment, Transverse pressure test, THEA

Zusammenfassung

Ziel dieser Arbeit ist es, die mechanischen und thermischen Eigenschaften für ein REBCO-Kabel für EU DEMO zu untersuchen.

Eines der Probleme bei großen HTS-Magneten ist die Sicherheit gegen ein Quench. Ein Quench ist ein plötzlicher thermischer Ausbruch, bei dem die Magneten gespeicherte Energie in einem lokal begrenzten Volumen des Magneten in Wärme umgewandelt wird. Wenn keine Gegenmaßnahmen ergriffen werden, kann der örtlich begrenzte Temperaturanstieg den Magneten beschädigen. Es wurde ein Quench-Experiment durchgeführt, um experimentelle Daten über die vollständige Quench Entwicklung in einem HTS-Kabel für Fusionsanwendungen zu erhalten. Die SULTAN Anlage wurde aufgerüstet, indem der supraleitende Transformator durch Stromdurchführungen ersetzt wurde, die an eine 15 kA Stromversorgung angeschlossen ist. Diese Aufrüstung ermöglicht es uns, den Leiter für unbestimmte Zeit mit hohem Strom und hoher Leistung zu versorgen. Zuvor war die maximale Leistung auf wenige W für wenige Sekunden begrenzt. Für den Central Solenoid von EU DEMO wurden vier verschiedene Leiter mit REBCO coated conductors hergestellt. Alle Kabel basieren auf einem Tripel von Rundlitzen, die aus zwei halbrunden Kupferprofilen bestehen, die einen Stapel von Bändern umgeben. Die Kupferprofile und die Bänder sind miteinander verlötet. Das Triplett wird in einen Stahlhülse (Jacket) eingelegt, um Leiter mit Zwangsströmung zu erhalten. Die Quench wird durch Einleiten von heißem Helium in den Leiter ausgelöst, und die Temperaturentwicklung der Leiterkomponenten (Stahlhülse, Helium) wurde bis zu Temperaturen von 150 K gemessen. Aufgrund des Temperaturgefälles zwischen Kabel, Helium und Jacket liegt der geschätzte Maximalwert für die Temperatur am Kabel bei über 200 K, je nach der spezifischen Kabelkonstruktion. Die experimentellen Ergebnisse der verschiedenen Leiter wurden mit Hilfe eines Multiphysik-Codes (THEA) interpretiert. Die Ergebnisse des multiphysikalischen Modells werden im Rahmen der Abschrecksicherheit diskutiert.

Die Kombination aus großem Strom und hohem Magnetfeld führt zu einer sehr großen Querbelastung des Kabels während des Magnetbetriebs. Das supraleitende keramische Material ist spröde, und die mechanische Grenze für beschichtete Leiter hängt stark von der Richtung der Kraft ab. Wird diese Grenze überschritten, nimmt der Strom unwiderruflich ab. Im zweiten Teil der Arbeit haben wir den kritischen Querdruck ermittelt, bei dem die Leistung des Kabels verringert. Es wurden verschiedene runde Strand hergestellt, um unterschiedliche Verstärkungsoptionen zu untersuchen. Der kritische Querdruck wird an einer Strand gemessen, indem sie bei der Temperatur von flüssigem Stickstoff geprüft wird und die Kraft mit einem Amboss anzuwenden wird. Die gemessenen Werte für den kritischen Querdruck zeigen an, welche Strandkonstruktionen verworfen werden sollten, wenn die gemessenen Werte für den kritischen Querdruck niedriger sind als die nominalen Werte, die in der vollständigen Kabelkonstruktion vorgesehen sind. Für eine der Verstärkungsoptionen wurde ein mechanisches Finite Elemente Modell entwickelt, um die Mechanik besser zu verstehen und Verbesserungen für das Kabeldesign vorzuschlagen. Es wurde festgestellt, dass die Leistung verbessert werden könnte, indem die Strand mit einem Draht umwickelt wird, dessen Wärmeausdehnungskoeffizient höher ist als der von Kupfer. Auf diese Weise wird die Strand während des Abkühlens vorgepresst und die Zugspannung, die zum Reißen der REBCO-Bänder führen könnte, wird verringert.

Stichwörter: Coated Conductors, Quench Experiment, Transverse pressure test, THEA

Sommario

Lo scopo di questa tesi è di studiare le caratteristiche meccaniche e termiche di un cavo costruito con nastri REBCO per il Tokamak di EU DEMO.

Uno dei problemi nei grandi magneti HTS è la sicurezza contro un quench. Un quench è un improvviso fenomeno termico in cui l'energia immagazzinata nel magnete si trasforma in calore in un volume localizzato. Se non vengono applicate contromisure, l'aumento di temperatura localizzato potrebbe danneggiare il magnete. Un esperimento di quench è stato condotto per fornire dati sull'evoluzione completa del quench in un cavo HTS per applicazioni nei magneti per la fusione. L'impianto SULTAN è stato rinnovato, sostituendo il trasformatore superconduttore con discensori di corrente collegati a un'alimentatore da 15 kA. Questo permette di fornire una potenza elevata al conduttore per un tempo indefinito. In precedenza, la potenza massima era limitata a pochi W per una durata di pochi secondi. Quattro diversi conduttori in scala ridotta del magnete del solenoide centrale di EU DEMO sono stati fabbricati con nastri REBCO. Tutti i cavi sono basati su una tripletta di elementi rotondi, ogni elemento è composto da due profili di rame semicilindrici che circondano un pacchetto di nastri. I profili di rame e i nastri sono saldati insieme. La tripletta è inserita in una camicia d'acciaio (jacket) per ottenere conduttori a flusso di elio forzato. Il quench è innescato dall'invio di elio caldo nel conduttore e le evoluzioni di temperatura dei componenti del conduttore (jacket, elio) sono state misurate fino a temperature di 150 K. A causa del gradiente tra cavo, He e jacket, il valore massimo di temperatura stimato sul cavo è superiore a 200 K, a seconda del tipo di cavo. I risultati sperimentali dei diversi conduttori sono stati interpretati con il supporto di un codice multifisico (THEA). I risultati del modello sono discussi con obiettivo la sicurezza del magnete durante il quench.

La combinazione di corrente elevate e alto campo magnetico provoca uno stress trasversale molto grande sul cavo durante il funzionamento del magnete. Il materiale ceramico superconduttore è fragile, e il limite meccanico per i nastri REBCO dipende dalla direzione della forza. Quando il limite viene superato, la capacità di trasporto della corrente del cavo è compromessa. Nella seconda parte della tesi abbiamo quantificato la pressione critica trasversale, alla quale le prestazioni del cavo peggiorano. Sono stati fabbricati vari strand rotondi, esplorando diverse opzioni di rinforzo. La pressione critica trasversale viene misurata su un elemento testandolo alla temperatura dell'azoto liquido, applicando la forza grazie ad una pressa meccanica. I valori di pressione trasversale critica misurati indicano quale tipo di elemento dovrebbero essere scartato, cioè quando i valori di pressione trasversale critica misurati sono inferiori a quelli nominali previsti nel cavo. Per una delle opzioni di rinforzo, è stato sviluppato un modello meccanico agli elementi finiti per capire meglio la meccanica e proporre un miglioramento del disegno cavo. Si è scoperto che le prestazioni potrebbero essere migliorate avvolgendo il l'elemento con un filo il cui coefficiente di espansione termica è superiore a quello del rame. In questo modo, l'elemento viene precompresso durante il raffreddamento e lo stress che potrebbe causare la rottura dei nastri REBCO viene diminuito.

Parole chiave: Coated Conductors, Quench Experiment, Test a pressione trasversale, THEA

Contents

Acknowledgements	Error! Bookmark not defined.
Abstract.....	vii
Zusammenfassung.....	viii
Sommario	ix
List of Figures.....	xii
List of Tables.....	xviii
List of Equations	19
Chapter 1 Introduction.....	22
1.1. Energy demand and production	22
1.1.1. Nuclear fusion	23
1.2. Superconductivity.....	24
1.2.1. The Quench	25
1.3. REBCO coated conductor: from tape to conductor	26
1.3.1. The coated conductors.....	26
1.3.2. The cables	29
1.4. Scope of the thesis.....	30
Chapter 2 The Quench Experiment.....	33
2.1. The motivation	33
2.2. The Quench Experiment Conductors.....	34
2.2.1. The conductors.....	34
2.2.2. The sample instrumentation	35
2.3. The test campaign	36
2.4. The DC characterization.....	37
2.4.1. Check of the expected conductor performance.....	37
2.4.2. The Conductors scaling law.....	41
2.4.3. The initial conditions for the Quench Experiment	42
2.4.4. The I_c distribution if the High Field Zone	43
2.4.5. The loss of performance.....	43
2.5. The Quench Analysis.....	44

2.5.1. The Cable temperature estimation	44
2.5.2. Comparison between the different shots	48
2.5.3. Estimation of the Normal Zone Propagation Velocity	54
2.6. The comparison with the THEA code.....	56
2.6.1. The model	57
2.6.2. The results.....	60
2.7. The effect of the magnetic field profile	68
Chapter 3 Strands transverse pressure tests.....	71
3.1. Cable designs	71
3.2. Transverse pressure tests	72
3.3. The mechanical model.....	78
3.4. Conclusions.....	83
Chapter 4 Conclusions.....	85
Appendix A.....	86
References.....	87
Curriculum Vitae.....	91

List of Figures

Figure 1:1. The fraction of energy source to produce the total energy in average in the world in 2019 [1].	22
Figure 1:2 The ITER machine. Picture taken from [10].	24
Figure 1:3 The engineering current density for several superconductors vs the magnetic field. The J_e of the Bi2223 and REBCO is with the field along the c axis. The engineering current density useful for magnet applications for fusion applications is highlighted. Below this value the superconductor does not carry enough current (compared to cooled copper) to justify its use. Data taken from [17].	25
Figure 1:4 The engineering current density vs temperature for the Nb_3Sn , the Bi2223 and the REBCO (with the field along the c axis) at 12 T. The scaling laws of the Nb_3Sn and REBCO are adapted from [18]. The data for the Bi2223 are taken from [16]. A representative operational current density J_{op} is highlighted to graphically illustrate the concept of ΔT_{margin} in the case of REBCO.	26
Figure 1:5 Artistic cross section of a REBCO tape. The a, b and c axis are highlighted. The figure is not in scale. Reported thicknesses in the figure are just an example.	27
Figure 1:6 The normalized critical current vs the angle between the tape ab plane and the magnetic field. The data are taken for the Superpower tape from [26]. The tape depicted is the transverse cross section.	28
Figure 1:7 The normalized critical current vs the longitudinal strain. The measurements is done on a Shanghai Superconductor Technology (SST) tape at 77 K, self field.	29
Figure 1:8 On the top the TSTC SPC 2015 cable prototype, taken from [39]. In the bottom left corner, the cross section of a strand (picture taken from [40]). In the bottom right corner, an artistic sketch of the strand.	30
Figure 1:9 a) The sketch of the CroCo strand. b) The ENEA slotted-core cable-in-conduit-conductor. Picture taken from [37].	30
Figure 2:1. The evolution of the temperature (left axis) and voltage (right axis, black and red curve) after that the quench is triggered in the Conductor#3 at 15 kA by warming up the inlet helium through a heat pulse (blue curve). The maximum voltage that can be reached by the usual SULTAN set up to charge the primary (using the transformer TRAFO) is depicted by the black dashed line. The red part of the voltage curve highlights the voltage range that the SULTAN upgrade allows to observe.	34
Figure 2:2. The fountain solder bath used to solder the strand.	35
Figure 2:3 The sketch of the sample instrumentation and the Sultan magnetic field distribution along the sample length. The zero of the z coordinate is placed at the He inlet of the sample. The HFZ is highlighted. Voltage taps in blue, temperature sensors in red. The He temperature sensor is shown in the bottom left corner.	36
Figure 2:4 Conceptual scheme of the model to compute the critical current and self-field distribution at 77 K.	38
Figure 2:5 a) The self-field of one strand of the Conductor#1. b) The I_c distribution in the stack of the strands belonging to the Conductor#1. For the strands of the other conductors, the B and I_c distribution are very similar but the values are slightly different.	38
Figure 2:6: Sketch of the instrumentation with the voltage taps label and the distances (in mm) used to measure the strand of the conductors at 77 K, s.f.	39
Figure 2:7 Measured I_c along the length in different regions (Figure 2:6) at 77 K, strand self-field for the different conductors. The symbols denote in a certain region the sum of the three strands belonging to the same conductor. The error bar on each symbol represents the repeatability of the measurement. The dashed lines represent the mean on the different regions for each conductor. The shaded area is the standard deviation on the different regions for each conductor.	39

Figure 2:8 The relative ratio in percentage of the measured critical current with respect the one expected at 77K, self-field for the different conductors. The value considered for the ratio is the sum of the critical current on the strands belonging to the same conductor.	39
Figure 2:9 The I_c of REBCO tapes measured at different magnetic fields at 4.2 K a) with the fit obtained by the scaling law. The scale for both axis is logarithmic.	40
Figure 2:10. The relative ratio in percentage of the measured critical current with respect the expected one at 7 K, 10.78 T.	41
Figure 2:11 The I_c of the a) Conductor #1, b) Conductor #3, c) Conductor #4 vs temperature. The dashed lines is the value obtained by the scaling law at constant magnetic fields. The blue dots represent the DC SULTAN measurements, while the triangular points the expected I_c computed from the tapes measurements	42
Figure 2:12 The I_c distribution along the conductor length in the a) Conductor#1, b) Conductor#3 and c) Conductor#4 in the HFZ, delimited in the picture.	43
Figure 2:13 The critical current of the a) Conductor#1, b) Conductor#3 and c) Conductor#4 vs temperature. The dashed lines is the value obtained by the scaling law at constant magnetic fields after the quenches and EM loads, obtained by the blue dots, the DC SULTAN measurements. The continuous lines denote the scaling law at the beginning of the test campaign.	44
Figure 2:14. The critical current vs temperature at the magnetic field selected for each conductor for the Quench Experiment at full current-low field. a) Conductor #1. b) Conductor #3. c) Conductor #4.	45
Figure 2:15. Electrical resistivity of copper as function of temperature for several RRR at zero magnetic field (lines, data from [58]). The values measured on the copper profile sample are indicated by open circles.	45
Figure 2:16. The magneto resistance as function of temperature for different magnetic fields (data from [58]). R_0 is the resistance at 0 T.	46
Figure 2:17 The resistivity used for the solder of the solder-filled conductor as function of temperature. The red dots represent the values found for the $\text{Bi}_{58}\text{Sn}_{42}$ in [53]. The blue dots are the data taken from [59].	46
Figure 2:18. The sketch of the electrical circuit of the conductor. The nodes A and B are the voltage taps in the HFZ.	47
Figure 2:19. The cable temperature profile along the conductor length for the Conductor#4 at the instant at which the maximum electric field is ~ 1 V/m, with the slow heating triggering the quench at full current, at $B = 6.5$ T. The cable, jacket and solder temperatures are computed considering the current sharing between the copper, stainless steel and solder, whose redistribution is shown by histograms.	48
Figure 2:20. The resistance per unit length of the materials involved in the Conductor#4 cable temperature estimation.	48
Figure 2:21 The quench triggered in two ways on the Conductor#4: a) the heat pulse ; b) the slow heating.	48
Figure 2:22 a) The $E_{hot-spot}$ evolution for the shots at 15 kA in the Conductor#1. b) The $T_{cable hot-spot}$ evolution for the shots at 15 kA in the Conductor#1.	49
Figure 2:23 a) The total voltage evolution for the shots at 15 kA in the Conductor#1. b) The total voltage vs the $T_{cable hot spot}$ for the shots at 15 kA in the Conductor#1.	50
Figure 2:24 The He temperature profiles of the Conductor#1 in the shot analysed for several times (at which the $E_{hot spot}$ is: 0.03, 0.1, 0.2, 0.3 and 0.65 V/m). (a) shot #161101; (b) shot #161103; (c) shot #161105; (d) shot #181101. The lines are interpolation between the temperature sensors location. The 0 is at the inlet of the helium in the conductor.	50
Figure 2:25 The E profiles of the Conductor#1 at different shots analyzed for several times (at which the $E_{hot spot}$ is: 0.03, 0.1, 0.2, 0.3 and 0.65 V/m). (a) shot #161101; (b) shot #161103; (c) shot #161105; (d) shot #181101. The width of the bar represents l_e length between the voltage taps. The 0 is at the inlet of the helium in the conductor.	51

Figure 2:26 a) The normalized Sultan field profile. The vertical red dashed lines are at the intersection of the 4% homogeneity of the field; b) the normalized I_c of the Conductors of the QE 7 K-3.5 T and 50 K-6.5 T along the length of the conductor, computed taking into account the SULTAN magnetic field profile; c) the normalized I_c for the Nb₃Sn at 10T maximum field for several temperatures computed taking into account the SULTAN magnetic field profile. The 0 is at the inlet of the helium in the QE conductor. The horizontal dashed lines are at 4% difference with respect to the max of the magnetic field, (minimum of the I_c). 52

Figure 2:27 The temperature and I_c profiles in the Conductor #1 for different shots. The temperature of copper, He and jacket are depicted at the instant when the $E_{hot-spot}$ is 0.65 V/m. The I_c (blue bars) is shown at the when the $E_{hot-spot}$ is 0.2 V/m ($t=0$ s). 53

Figure 2:28 The total voltage evolution in the Conductor#1 for two shots at 15 and 9.5 kA. 53

Figure 2:29 The total voltage (a) and the $E_{hot spot}$ (b) evolution for the three conductors at 15 kA operating current, with heat pulse heating mode and mass flow rate of 1.5 g/s. Namely the 161101 shot for the Conductor#1, 170808 for the Conductor#3, 140809 for the Conductor#4. 54

Figure 2:30 The temperature evolution in the hot spot for the Conductor#1 (a), Conductor#3 (b), Conductor#4 (c), at the 15 kA operating current, with heat pulse heating mode and mass flow rate of 1.5 g/s. The hot spot location is where the maximum E (and so T_{cable}) is measured. The T_{He} and T_{Ja} are the measured temperature by the closest thermometer. 54

Figure 2:31 The evaluation of the normal zone propagation velocity in the case of the Conductor#4 for the shot 140809. In the legend in the bottom plot, the position of the middle point of the regions across which the voltage was measured. As an example, the evaluation of the NZPV in the region, VH4-V10, whose middle point is at 795 mm. 55

Figure 2:32 The NZPV for the three conductors along the length. In the bottom part of the plot, the coloured lines indicate the hot spot location for the conductor with the same colour. The two bases of the plotted rectangles indicate the maximum and minimum value of the NZPV evaluated for the considered region among the three electric field thresholds. The HFZ is highlighted. The NZPV was estimated in the case of 15 kA in the a) heat pulse scenario (161101 for the Conductor#1, 170808 for the Conductor#3, 140809 for the Conductor#4); b) the slow heating (161103 for the Conductor#1, 190807 for the Conductor#3, 190808 for the Conductor#4). 56

Figure 2:33. The I_c distribution along the length for the three strands of the Conductor#1 at 3.5 T at an average temperature of 44 K. 57

Figure 2:34. Thermo-physical properties used for the solder of the solder-filled conductor as function of temperature. The red dots represent the values found for the Bi₅₈Sn₄₂ in [59]. a) The thermal conductivity; b) the specific heat. 58

Figure 2:35. The temperature evolution (on the left axis) recorded by the sensors in the HFZ in the Conductor #4, in a slow heating shot, a high B and low I . On the right axis, the evolution of the heater used to trigger the quench (in blue) and the total voltage (in black). 58

Figure 2:36 The simulated temperature evolution of the strand and the jacket in the hot spot of the Conductor #1, with and without the He. 59

Figure 2:37. The heat capacity of the different materials of which the Conductor#1 is made of as function of temperature. 59

Figure 2:38. The parametric study on the copper RRR of the simulated results of the quench development of the Conductor #1. a) The total voltage on the conductor vs the hot spot temperature. b) The temperature evolution of the strand and the jacket in the hot spot. 60

Figure 2:39. a) The normalized electric field profile in the HFZ, simulated vs experimental. b) The total voltage of three simulated cases with three different R_{th} between strand and jacket and the experimental one. 60

Figure 2:40 a) The diffusion time in the jacket of the Conductor#1 as function of temperature. The temperature ranges in the jacket used in the simulations with the 15 kA and 9.5 kA operating current are highlighted; b) The evolution of the strand and jacket temperature (simulated and experimental) for the

Conductor#1 in 15 kA and 95 kA operating current shots; c) The simulated strand and jacket temperature evolution for different strand-jacket thermal resistances are compared to the experimental one. ...61

Figure 2:41 The division of the jacket into two shells, in order to model the radial thermal gradient in the thickness. 62

Figure 2:42 The temperature evolution of strand and jacket, simulated both with one or two shells. The two models have the same $R_{th\ strand} - J_{aext}=0.12\text{ K}\cdot\text{m}/\text{W}$. The simulated results are compared with the experimental ones. 62

Figure 2:43 a) The evolution of the strand and jacket temperature in the hot spot of the Conductor#1 for both 15 and 9.5 kA. The simulated results (obtained for several $R_{th\ strand} - J_{aext}$, whose values are reported in the frame d)) are compared with the experimental ones. b) The heat capacity per unit length for the different components of the Conductor#1 as function of time. c) The simulated relative current evolution in the Conductor#1 at 15 kA-3.5 T by varying the $R_{th\ strand} - J_{aext}$ d) The error (computed as relative norm) between the simulated and experimental strand temperature as function of $R_{th\ strand} - J_{aext}$, for both 15 kA and 9.5 kA shots. 63

Figure 2:44 The electric field as function temperature (simulated and experimental) in the hot spot of the Conductor#1 for both 15 and 9.5 kA. 64

Figure 2:45 a) The temperature evolution in the hot spot of the conductor#3 at 15kA-6 T and 11kA-10T. b) The electric field vs strand temperature in the hot spot the conductor#3 at 15kA-6 T and 11kA-10T. 64

Figure 2:46 a) The temperature evolution in the hot spot of the conductor#4 at 15kA-6.5 T and 11kA-10.8T. b) The electric field vs strand temperature in the hot spot the conductor#4 at 15kA-6.5 T and 11kA-10.8T. 65

Figure 2:47 a) The simulated temperature evolution in the hot spot of the Conductor#4 at 15 kA-6.5 T for the several thermal components of the conductor. b) The simulated evolution of the relative current with respect to the operating one in the different electric components of the Conductor#4 at 15 kA-6.5 T. 65

Figure 2:48 The simulated temperature evolution in the hot spot of the Conductor#1 and #3 at 15 kA in the strand and jacket. The same $R_{th\ strand} - J_{aext}$ is set for both the conductors. 66

Figure 2:49. The tape bent in the easy bending a) and hard bending direction b). 66

Figure 2:50 a) The simulated and experimental temperature evolution in the hot spot of the Conductor#1, #3 and #4 at 15 kA in the strand. The solid line is the strand temperature of the Conductor#4 without the solder and having set the same jacket cross section as in the Conductor#1 and #3. b) The simulated hot spot strand temperature derivative in time with respect to the strand temperature in the Conductor#1, #3 and #4 at 15 kA. The solid line is the strand temperature of the Conductor#4 without the solder and having set the same jacket cross section as in the Conductor#1 and #3. c) The relative current repartition in time among the cable and the jacket in the Conductor#4 without solder and with the jacket having the same cross section of the Conductor#1. 67

Figure 2:51 The simulated current carried by the copper in the hot spot in the Conductor #1, #3 and #4 with respect to the strand temperature. The conductors have the materials with the same cross section. 67

Figure 2:52 The quench development comparing the strand temperature (a) and the electric field (b) along the conductor length, at different times. 68

Figure 2:53 a) The normal length propagation in the B_{SULTAN} case and uniform one. The dashed lines point the hot spot; b) the NZPV in the B_{SULTAN} case and uniform one along the conductor length. 69

Figure 2:54 a) The total voltage evolution in the B_{SULTAN} case and uniform one. The red dashed line indicates the detection threshold voltage (0.1 V); b) the total voltage vs the strand hot spot temperature in the B_{SULTAN} case and uniform one. The red dashed line indicates the detection threshold voltage (0.1 V); c) The strand temperature evolution in the hot spot. 70

Figure 3:1 a) The experimental set-up for the transverse pressure test, picture from [31]; b) the anvil, positioned on the TSTC on flat core sample; c) the sketch of the different orientation of the transverse force applied during the taste the experimental results. 73

Figure 3:2 The strand for the 6 around 1 cable assembled for the transverse pressure. The regions tested to have the results at different orientations are highlighted.	74
Figure 3:3 The critical current relative to pristine one of the not-annealed strand as function of the pressure at the midplane ($p_{midplane}$). The force was applied along three different directions. The set degradation threshold (0.98) is highlighted, as the cable nominal pressure. The error bar indicates the reproducibility of the measurements, being the standard deviation obtained by several of them.	74
Figure 3:4. The electrical resistivity of copper as function of the temperature for different RRR at 0 and 10 T.	74
Figure 3:5 a) The critical current relative to the pristine one of the annealed strand as function of the pressure at the midplane ($p_{midplane}$). The force was applied along three different directions. The degradation threshold (horizontal dashed line) and the nominal value of the pressure at the midplane in the cable (vertical dashed line) are highlighted. The error bar indicates the reproducibility of the measurements, being the standard deviation obtained by several of them. b) The relative critical current degradation at 90° to show the irreversibility of the results obtained going back to 0 MPa.	75
Figure 3:6 The history of strand critical current from the strand assembly to the tapes extraction. The strand critical current before assembly and after extraction tapes are computed from the measured tape I_c , while the others are measured.	75
Figure 3:7 The dummy strand wrapped by the steel tape when straight (a), bent on a radius of 320 mm in the compression side $R=320$ mm (b),), bent on a radius of 320 mm in the tension side(c).	76
Figure 3:8 a) The sketch of the new strand design for the Rutherford like cable, made of not- soldered stack and wrapped by the steel wire ; b) the strand prepared for the transverse pressure test.....	76
Figure 3:9 The critical current relative to the pristine one of the not-soldered reinforced annealed strand as function of applied force per unit length for different direction of the force. The cable nominal force is highlighted. The error bar indicates the reproducibility of the measurements, being the standard deviation obtained by several of them. The numbers indicate the measurement sequence.	77
Figure 3:10 The deformation of the strand after the application of the transverse load.	77
Figure 3:11 a) The stack on the edge of the copper core before the solder filling; b) The sample after the solder filling; the sketch of the edge c) and bottom d); e) The critical current relative to the pristine one of the new annealed strand as function of applied pressure. The cable pressure and the one at which the irreversibility limit is reached, are highlighted.....	78
Figure 3:12 The sketch of the domain in the 90° and 45° orientation.	79
Figure 3:13 The thermal expansion coefficient of the Alu alloy, copper and steel as function of temperature.	79
Figure 3:14 Tensile stress-strain curve for the materials considered in the model.	80
Figure 3:15 The cumulative of the fraction of the stack cross section vs the tensile strain along the x axis in the 90° orientation. The copper outer diameter is 5.5 mm, the wire wrapped around the copper is in Alu alloy of 0.75 mm diameter and the pretension force on the wire is 30 N. The cross section of the strand is illustrated in the bottom right corner, with the values of the tension along the x axis shown in the stack. The coloured bar in the plot have the same colours illustrated in the stack cross section	80
Figure 3:16 The cumulative of the fraction of the stack cross section vs the tensile strain along the x axis in the 90° orientation, for different wire materials, wire and copper shell outer diameter. SS stands for stainless steel. The dashed red line represents the limiting value of delamination tension for the tapes and it is taken from [25]. In all the scenarios with a wire, the tension applied on the wire during the wrapping (before the cool down) is 30 N. In the bottom right corner, the cumulative fraction of the stack cross section at the limiting value of delamination tension is shown for the various cases considered. The colour code is the same of the plot on the left side.....	81
Figure 3:17 The cumulative of the fraction of the stack cross section vs the tensile strain along the x axis in the 45° orientation when the maximum force is applied, for different wire materials, wire and copper shell outer	

diameter. SS stands for stainless steel. The dashed red line represents the limiting value of delamination tension for the tapes and it is taken from [25]. In all the scenario with a wire, the tension applied on the wire during the wrapping (before the cool down) is 30 N. In the bottom right corner, the cumulative fraction of the stack cross section at the limiting value of delamination tension is shown for the various cases considered. The colour code is the same of the plot on the left side.....81

Figure 3:18 The cumulative of the fraction of the stack cross section vs the shear stress in the 45° orientation when the maximum force is applied, for different wire materials, wire and copper shell outer diameter. SS stands for stainless steel. The dashed red line represents the limiting value of shear stress for the tapes and it is taken from [25]. In all the scenario with a wire, the tension applied on the wire during the wrapping (before the cool down) is 30 N. In the bottom right corner, the cumulative fraction of the stack cross section at the limiting value of shear stress is shown for the various cases considered. The colour code is the same of the plot on the left side.....82

Figure 3:19 The plastic deformation in mm/mm in the wire and strand at the maximum force at 77 K in the case with 0.75 mm a) soft Alu alloy (100 MPa yield stress at 77 K) and b) with harder Alu alloy (324 MPa yield stress at 77 K). The undeformed wire shape (no pressure, RT) is shown (black line). The deformation is amplified 2.9 times. In figure a) it is possible to see that a gap opens. In c) the tension along the x axis in the stack in the case of soft Alu alloy wire, while in d) with the hard Alu alloy one, at the same temperature and force conditions of a) and b) picture.....82

Figure 3:20 The cumulative of the fraction of the stack cross section vs the tensile strain along the x axis, in the 90° orientation exploring the effect of the annealing and the diameter of the copper shells and the wrapping of the strand with the Alu alloy wire. The dashed red line represents the limiting value of delamination tension for the tapes and it is taken from [25]. On the right, the cumulative fraction of the stack cross section at the limiting value of delamination tension is shown for the various cases considered. The colour code is the same of the plot on the left side.83

Figure A:0:1 The I_c along the length of the different REBCO spools, provided by the producer, used to manufacture the Quench Experiment conductors. The I_c is measured at 77 K, s.f.. a) spool #34, b) spool #35, c) spool #36, d) spool #37, e) spool #38, f) spool #39. Here, the length dedicated to each conductor is highlighted, together with the integral mean of the I_c and the standard variation.86

List of Tables

Table 1:1 Characteristics of the commercial SC. Data taken from [16].	25
Table 1:2 Mechanical strength of REBCO tapes for several stress. Data taken from [25].	28
Table 2:1 The list of the conductors for the Quench Experiment and the full size conductor.	35
Table 2:2. The summary of all the values of the parameters used during the Quench Experiment.	37
Table 2:3. Features of REBCO tapes purchased by SST.	37
Table 2:4 Conductor stack composition (number of tapes from each spool, the total number of tapes in one conductor is 75).	37
Table 2:5. The parameters of the scaling law for the tapes obtained by the measurement on the tapes at different field at 4.2 K, in perpendicular direction.	40
Table 2:6. The parameters of the scaling law for the conductors obtained by the DC measurement.	42
Table 2:7 The selected fields for each conductor to perform the Quench Experiment at 15 kA, 7 K.	42
Table 2:8 The selected fields for each conductor to perform the Quench Experiment at lower current, starting from 7 K.	43
Table 2:9 The $f(T_{cable}, T_{ja})$ used in Equation 2:6 for different materials.	47
Table 2:10 The list of the shots analysed for the Conductor#1 with their specifications.	49
Table 2:11 The list of the shots analysed for the Conductor#3 with their specifications.	49
Table 2:12 The list of the shots analysed for the Conductor#4 with their specifications.	49
Table 2:13. Cross section of the thermal domains composing the conductors.	57
Table 2:14 The n of strands at 4.2 K for the several conductors and for the cable at 7 K.	57
Table 3:1 The design featured of the different designs considered for a the CS in DEMO. The TSTS on flat core sketch is an artistic representation. The drawing for the 6 around 1 and Copper-core Rutherford cables are taken from [69].	72
Table 3:2 The feature of the TSTC on flat core sample for the transverse pressure test.	77
Table 3:3 The yield stress at 77 K and RT for the materials considered in the model.	79
Table 3:4 The list of the pressure limits and margin from the cable operating one for the different cable designed analysed.	84

List of Equations

Equation 1:1 - The power law for the electric field as a function of current density.....	24
Equation 1:2- The power law for the electric field as a function of temperature.....	26
Equation 2:1- The self-field in the stack B is computed as the curl of the magnetic vector potential A38	
Equation 2:2- The scaling law equation for the critical current as function of magnetic field and temperature.	40
Equation 2:3- The computation of the I_c in the cable starting from the I_c in the tape	40
Equation 2:4- The RRR evaluation.....	45
Equation 2:5- The electric field of the equivalent electric system.	47
Equation 2:6-The equivalent resistance per unit length of the circuit with i in parallel. For the specific problem all the T_i can be obtained as function of T_{cable} , T_{ja} . The fT_{cable} , T_{ja} are in Table 2:8.	47
Equation 2:7- The current flowing in the i^{th} path.....	47
Equation 2:8- The transverse thermal resistance across the shells	62
Equation 2:9- The average joule dissipation power in the current sharing regime evaluated as integral average between T_c and T_{cs}	68

Chapter 1 Introduction

1.1. Energy demand and production

Human activities are the main cause of climate change, because of greenhouse gas emissions. Greenhouse gases prevent infrared radiation emitted by the earth's surface from escaping the atmosphere. As a consequence, an increase of greenhouse gas concentration in the atmosphere leads to the increase of temperature, both in the air and in the water, causing devastating environmental consequences, like desertification, melting of the glaciers, rising of sea level. This affects modern human society, leading to a lack of resources, food and lands, that which eventually cause even military conflicts. The most important greenhouse gases are water, CO_2 , methane. According to [1], the energy sector (electricity, industrial and domestic heat and transport) is responsible for 73% of the emitted greenhouse gases (in 2016), because it is mainly based on combustion of fossil fuels, emitting CO_2 (see Figure 1:1). One way to decarbonize the energy sector is to replace as much as possible fossil fuels with carbon-free source of electricity.

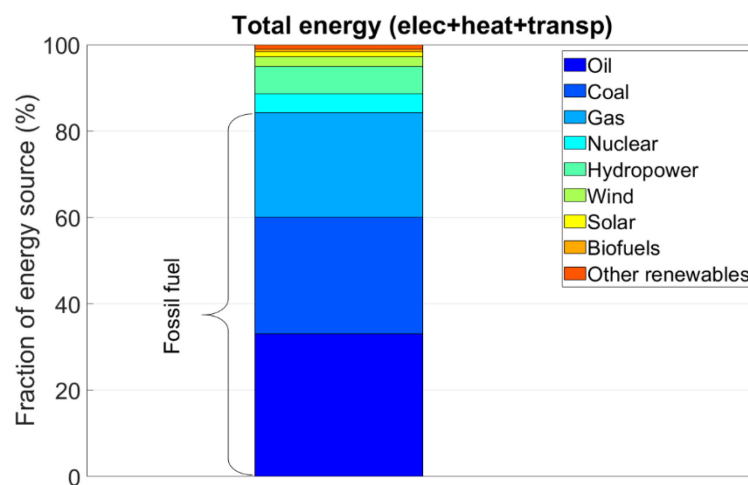


Figure 1:1. The fraction of energy source to produce the total energy in average in the world in 2019 [1].

It is then fundamental to decarbonize the electrical energy sector, especially because the energy demand is foreseen to increase in the future following the increase in urbanization, industrialization, mobility as well as world population. The Intergovernmental Panel on Climate Change IPCC issued in October 2018 the special report “Global Warming of 1.5°C” [2], as requested in the Decision of the 21st Conference of Parties (COP21) of the United Nations Framework Convention on Climate Change. In this report, the most stringent strategy requires to limit global warming to 1.5°C more than preindustrial temperatures, reducing by 45% by 2030 the CO_2 emissions from human activities with respect to 2010 and to reach the net zero emissions around 2050. This goal was barely kept alive in the last COP26 in Glasgow.

Moreover, fossil fuels are not evenly distributed around the world and are not renewable. In around 100 years [3], the world will run out of the most common energy resource. The change cannot wait any longer. There are different ways to produce energy without emitting CO_2 : by renewables (photovoltaic, hydro, wind), by nuclear power plants, or, as a transition process, by adding to the conventional fossil fuel power plants a Carbon Capture Storage (CCS) system [4]. All of them produce electricity, but the renewables produce it in an intermittent way. This makes it difficult to cover the base load needs of a country, at least as long as storage technologies have not yet reached a sufficient development level. Nuclear fission plants produce energy in a continuous way without producing CO_2 , but with the problem of high level and long lived (half-life of tens of thousands of years) radioactive wastes disposal. Another disadvantage of nuclear fission is that its fuel, uranium, is a limited resource. Finally, nuclear fission technology is not well socially accepted, because of the fear of a nuclear accident.

Nuclear fusion is intrinsically safer than fission (it will switch off if control fails), its fuel is several orders of magnitudes more abundant than coal and uranium and does not produce long-lived radioactive wastes. However, at present, it is not yet available as practical electric power plant alternative, because technologically challenging. The most promising fusion reaction for energy use is the deuterium-tritium (D-T) reaction, whose products are high energy neutrons (14.1 MeV) and alpha particles (3.5 MeV) [5]. The deuterium can be easily obtained from water. Tritium is not available in nature (it is radioactive with around 12 years of half-life) but can be bred in the reactor in a closed fuel cycle. Breeding takes place in a blanket containing lithium, which reacts with the fusion-produced

neutron to give tritium, an alpha particle, and additional energy ($\text{Li}_6 + n \rightarrow \alpha + \text{T} + 4.8 \text{ MeV}$) [6]. Lithium is found in the earth's crust and water. Even if it is not especially abundant, it is a hundred times more abundant than uranium, and fusion reactions need much less fuel than fission. The high energy neutrons coming from the reaction, while slowing down, produce heat that can be removed by a coolant. The coolant transforms heat into mechanical energy in a turbine. A generator is attached to the turbine shaft to produce electricity.

1.1.1. Nuclear fusion

Significant amounts of D-T fusion reactions only occur at temperatures of the order of several tens of millions of degrees. At such high temperatures, matter is in the form of plasma, a mix of ions and electrons. There are several ways to confine plasmas. The one discussed in this section is magnetic confinement: as the plasma is composed of charged particles, a magnetic field can be used to trap the ions and electrons. The easiest way to confine the particles by a magnetic field is in a toroidal configuration. So far, the best configuration is based on the superposition of toroidal and poloidal fields, produced either by complicated coil systems (Stellarator), or by a combination of Toroidal Field (TF) coils and currents in the plasma [7]. The machine that realizes the latter configuration is called Tokamak. The plasma current is induced by a time varying magnetic field created by the Central Solenoid (CS) coil. The CS can be intended as the primary of a transformer, while the plasma is the secondary. For this reason, the Tokamak is a pulsed machine [8].

In contrast to most electric power plants, Tokamak fusion plants would need a considerable amount of electricity (hundreds of MW) for functioning. This is the so-called "recirculating power". Since the final goal is the electricity production, it is important to increase the output power as much as possible with respect to the input electrical power. The use of superconducting magnets makes it possible to obtain high magnetic fields in the plasma with much less electrical energy consumption than using normal conductors, such as copper. Without superconductivity, it would almost be impossible to reach net electrical gain [9].

The largest tokamak project in the world is ITER ([10]Figure 1:2), whose goals are to prove that is possible to obtain a gain Q (ratio between fusion power and input power to the plasma) higher than 10, with at least 500 MW of fusion power and, to demonstrate the integrated operation of technologies for a safe nuclear fusion power plant. The demonstration of electricity production, although not at the price of commercial power plants, will be addressed in EUROfusion (European consortium for the development of nuclear fusion) with the Tokamak demonstration reactor DEMO by 2060 [11]. DEMO must demonstrate the necessary technologies for safely generating electricity, for the generation of the tritium fuel and for regular, fast, and reliable maintenance of the plant. The design of the plant must take into account not just physics demand, but also engineering and technological limitations. The goal for DEMO is the generation of 300–500 MW of electrical power with a closed tritium fuel-cycle. One of the key problems in advancing fast enough with respect to the deadlines settled by the COP21, is the size of the Tokamak machine, which determines significant technological challenges. The present version of EU DEMO Tokamak is roughly 1.5 times bigger than ITER, leading to severe problems in the scalability of the different components [12]. According to the EUROfusion roadmap to fusion electricity, commercial power plants will be deployed around the end of the century [13]. In response to the urgency of CO_2 emission reduction, several private companies (like Tokamak Energy and Commonwealth Fusion Systems) are investigating compact, modular high field Tokamak and Stellarators. The idea is to reduce the difficulties in building enormous machine, reducing the construction time. These reactors are significantly smaller than the EUROfusion DEMO Tokamak. For example, the Affordable Robust Compact reactor proposed by MIT [14] is 19 times smaller than the EU DEMO, in its 2018 version [15]. The target for demonstrating electricity production is set between 2030 and 2040, followed by commercialization. In high field and compact Tokamaks, the magnets are built with High Temperature Superconductors (HTS), instead of Low Temperature Superconductor (LTS), which were used for ITER magnets and will be used for most of the DEMO magnets. The meaning of LTS and HTS is explained in the following section.

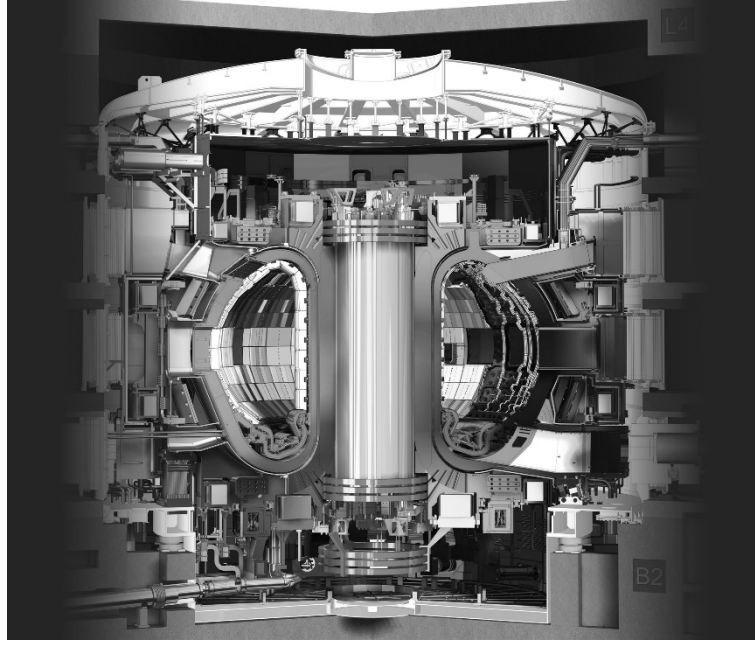


Figure 1:2 The ITER machine. Picture taken from [10]

1.2. Superconductivity

Superconductivity is the property of certain materials to manifest zero electrical resistance and perfect diamagnetism. A material is superconducting if the operating conditions in terms of temperature, magnetic field and current density are below a critical surface. The critical temperature T_c , at 0 T, is the temperature at which the superconductor does not carry current anymore. The magnetic field at which the superconductor carries zero current at a given temperature is called the critical field B_c . At a given temperature, magnetic field and, for some superconductors, strain ε and angle ϑ with respect to the magnetic field direction, the current density at the critical surface is called critical current density, J_c . Practically, it is determined as the current density at which the electric field overcome a certain threshold E_0 (usually, 1e-5 V/m in LTS and 1e-4 V/m in HTS, but 1e-5 V/m is used sometimes also for HTS). The electric field is function of the current, according to the power law relationship in Equation 1:1.

$$\frac{E}{E_0} = \left(\frac{J}{J_c(B, T, \varepsilon, \theta)} \right)^n$$

Equation 1:1 - The power law for the electric field as a function of current density.

In magnet applications, the superconductor should carry large current in high magnetic field; therefore, the operating temperature T_{op} is usually much lower than the critical temperature, even for high temperature superconductors. Superconductors are divided in Type I and Type II. Only Type II superconductors may carry large current in high magnetic field, therefore are the only ones that can be used in magnets. Among thousands of Type II superconducting materials, only a few are today available in the form of wire or tape and with a length of hundreds of meters [16]. They are the so-called technical superconductors: NbTi, Nb₃Sn, MgB₂, Bi2212, Bi2223, REBCO (see Table 1:1). These superconductors are sold as composite: the superconductor is mixed with other materials that have different functions, such as the stabilization and recovery from the loss of superconductivity, mechanical reinforcement or to provide elements to the final superconducting material. The engineering current density, J_e is the critical current divided by the total strand cross section. Depending on the value of T_c , the superconductors are traditionally classified Low Temperature Superconductors, Middle-High Temperature Superconductors (MHTS) and High Temperature Superconductors. All commercial magnets are built with LTS. The HTS have the advantage that they can sustain much higher magnetic fields than LTS, if used at same operating temperature and current density (see Figure 1:3). Alternatively, HTS can be operated at higher temperature, with some cryogenic advantages. In traditional forced flow conductors for fusion magnets, the operating temperature is about 5 K (supercritical helium). By using HTS, it could be possible to cool down a fusion magnet even by liquid hydrogen (around 20 K). The EUROfusion R&D in HTS fusion cables considers He as the coolant and an operating temperature of about 5 K, because HTS is used together with LTS. Instead, compact high field Tokamaks (Commonwealth Fusion Systems, Tokamak Energy) are designed to operate at 20 K. One of the advantages of HTS materials is to generate fields higher than about 16 T, the limit for Nb₃Sn. However, a higher magnetic field leads to

higher electromagnetic forces; in very large magnets, traditional structural materials may not be able to sustain such high loads. In tokamaks, the advantages of using a high magnetic field are:

- High fusion power density ($\propto B^4$), and better plasma stability if used in TF;
- High magnetic flux to increase the plasma burn duration or to reduce the size of the machine, if used in the CS;
- High temperature margin against the thermal instability (quench) at the operational condition, in both TF and CS.

SC	Material	T_c (K)	B_{c2} (T)	Kind of SC
NbTi	Ductile, alloy	9.8	10.5 (4.2 K, measured)	LTS
Nb ₃ Sn	Brittle, intermetallic	18.2 K	24.5 (4.2 K, measured)	LTS
MgB ₂	Brittle, metalloids	39 K	35 (estimated field) 60 (estimated \perp field)	MHT
Bi2212	Brittle ceramic	~80 K	>100 (0 K, estimated)	HTS
Bi2223	Brittle ceramic	~110 K	>100 (0 K, estimated)	HTS
REBCO	Brittle ceramic	93 K	150 (0 K, estimated)	HTS

Table 1:1 Characteristics of the commercial SC. Data taken from [16].

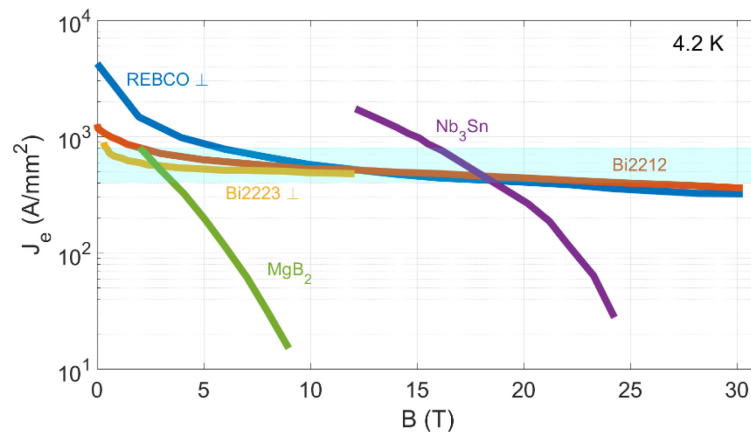


Figure 1:3 The engineering current density for several superconductors vs the magnetic field. The J_e of the Bi2223 and REBCO is with the field along the c axis. The engineering current density useful for magnet applications for fusion applications is highlighted. Below this value the superconductor does not carry enough current (compared to cooled copper) to justify its use. Data taken from [17].

1.2.1. The Quench

In a superconducting magnet, heat disturbances can deposit sufficient energy in the winding to trigger a positive heating feedback, the so called quench. Even a very small amount of energy may trigger a quench, because the heat capacity of the materials below 10 K is extremely small. In fusion magnets, the energy perturbation can be nuclear heat load, wire motions, and AC losses. The current sharing temperature T_{cs} is the temperature at which, at a given magnetic field and operational current density J_{op} , the superconductor (SC) starts to become resistive, (superconducting transition). Practically, it is defined as the temperature at which the electric field in the conductor goes above a certain threshold E_0 (usually, $1e-5$ V/m in LTS and $1e-4$ V/m in HTS, but $1e-5$ V/m is used sometimes also for HTS). The temperature margin, ΔT_{margin} , is the difference between the current sharing temperature T_{cs} and the operational temperature T_{op} (see Figure 1:4). In case the temperature increases above T_{cs} , the superconductor starts to develop an electric field according to a power law (Equation 1:2).

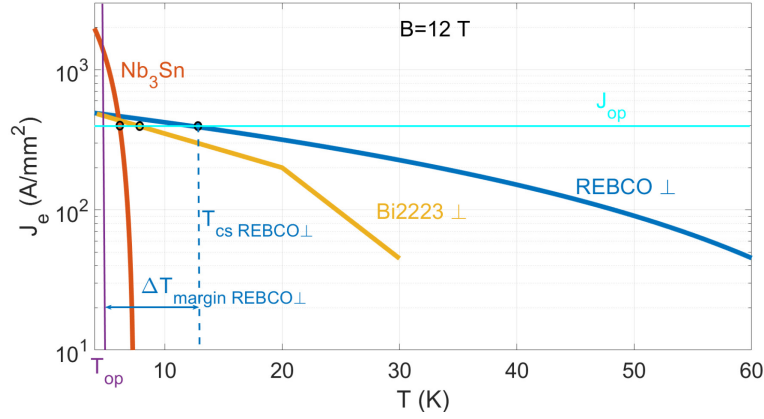


Figure 1:4 The engineering current density vs temperature for the Nb₃Sn, the Bi2223 and the REBCO (with the field along the c axis) at 12 T. The scaling laws of the Nb₃Sn and REBCO are adapted from [18]. The data for the Bi2223 are taken from [16]. A representative operational current density J_{op} is highlighted to graphically illustrate the concept of ΔT_{margin} in the case of REBCO.

$$\frac{E}{E_0} = \left(\frac{T}{T_{cs}} \right)^m$$

Equation 1:2- The power law for the electric field as a function of temperature

Copper has a smaller resistance than the superconducting material when it is not in superconducting state. If copper is placed in parallel with the superconductor, depending on the cooling conditions, the copper cross section and the electrical resistance between copper and superconductor, the positive heating feedback is diminished, and the composite (Cu+SC) can recover its superconducting state, i.e. the superconductor is stabilized against the perturbation. This happens if the energy deposited in the superconductor is lower than a Minimum Quench Energy (MQE). If the energy is larger than the MQE, the normal zone expands irreversibly. This is a quench. In this case, copper has the role of protection of the SC, because, in this way, the temperature rises slowly (reduced Joule heating, because of the lower resistance). In the LTS fusion magnets built so far, the quench is detected by measuring the voltage drop across the coils. If the voltage stays above a certain threshold for a sufficiently long time (validation time), the quench is detected and the current is dumped on an external resistor, with a time constant that depends on the inductance and the total resistance of the circuit. It is critical to extract the stored energy of the magnet and dump it into an external resistor, in order to limit the temperature in the hot spot.

Regarding the quench, the HTS have a much higher ΔT_{margin} , and MQE than LTS, making the quench event less probable. However, the high margin is also the reason that makes difficult to detect the quench. The normal zone expands slowly, confining the hot spot in a tiny fraction of the magnet volume and slowing the rise in voltage. Therefore, when the quench is detected, the temperature in the hot spot might be already so high to damage the magnet. For this reason is essential to study the quench for HTS, in order to understand to which extent the traditional voltage detection system is safe, or other strategies are necessary (for example optical fiber [19], cowound with a LTS [20] [21], acoustic detection, or magnetic techniques [22]).

1.3. REBCO coated conductor: from tape to conductor

1.3.1. The coated conductors

There are three commercially available HTS: Bi₂Sr₂Ca₂Cu₃O_x (Bi2223), Bi₂Sr₂CaCu₂O_x (Bi2212), and Rare-Earth Barium Copper Oxide (REBCO). The superconducting material in the three cases is ceramic. The Bi2223 and REBCO are sold ready to be used and in the shape of tapes, while the Bi2212 needs a heat treatment at 890°C, in oxygen atmosphere. Among the three HTS, REBCO coated conductors have the highest engineering current density and the highest mechanical limits in terms of longitudinal and transverse compression tensile stress and bending strain. Coated conductors became industrially available in 2000s, while Bi2223 and Bi2212 production started in the 90's. Thus, REBCO is the newest HTS and the one with largest margin of improvement. Moreover, there are more than ten suppliers of coated conductors with a combined production capacity of several tons/year. Instead, there are only two companies producing small amount of Bi2212 wire and only one for Bi2223 tapes. For all these reasons, most HTS fusion cable designs are based on REBCO coated conductors.

REBCO ceramic can carry very large electrical currents only if the grains are biaxially textured along the c axis and in ab plane (see Figure 1:5), with a misalignment $<5^\circ$ [23]. The only process so far to produce long length of biaxially textured REBCO starts with a thin tape, the substrate. It is usually in Hastelloy, a nickel alloy having high mechanical performance, high flexibility and a non-magnetic. Its thickness could be customized usually between 30 and 100 μm , and is typically 12 mm (half inch) wide. Buffer layers are deposited on the substrate, which function as texture base, on which the superconductor grains grow with no misalignments. Buffer layers act also as a diffusion barrier between the REBCO and the substrate. The ceramic is deposited on the textured buffer and grows with the same texturing. A REBCO superconducting tape can be considered as a quasi-single crystal several hundred meters long. The superconducting ceramic occupies less than 5% of the cross section. A silver layer allows oxygen to diffuse into the REBCO during a subsequent annealing. The 12 mm tape can be slit in narrower tapes, down to 2 mm. Finally, the copper is electroplated on the conductor, with a customized thickness up to about 20 μm . More detailed on the manufacturing of REBCO tapes can be found in [24].

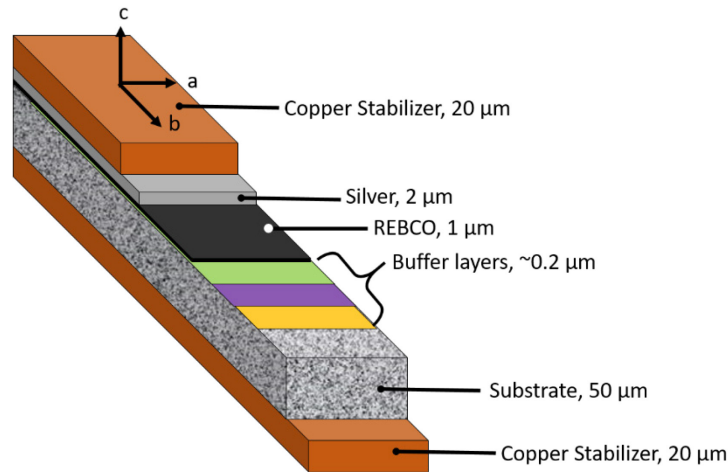


Figure 1:5 Artistic cross section of a REBCO tape. The a, b and c axis are highlighted. The figure is not in scale. Reported thicknesses in the figure are just an example.

The mechanical and electromagnetic properties of coated conductors are strongly anisotropic. Coated conductors are very strong in longitudinal tensile and transverse compressive directions. However, the layered structure (that can be thought as adhesive-copper-REBCO and REBCO-Hastelloy joints) makes them weak against shear, peeling and cleavage (see Table 1:2). Moreover, their critical current depends on the angle between the ab plane (wide face of the tape) and the magnetic field, with a variation up to a factor six at 4.2 K, 12 T (see Figure 1:6). The critical current varies only a little with longitudinal strain, but drops abruptly for strain above 0.4%-0.6 % (see Figure 1:7), due to ceramic nature of the SC. The strain arises during the cabling and the magnet winding, because these steps require bending of the tape. All these aspects make the transition from LTS to HTS cabling, treated in the section of 1.3, difficult. In Nb_3Sn wires the critical current is more sensitive to strain than in REBCO. However, during the cabling process, the wire is still ductile, because the Nb_3Sn is not yet formed. Instead, REBCO coated conductors are already supplied with the brittle ceramic phase completely formed. During the cabling and winding process the strain accumulates after every step.

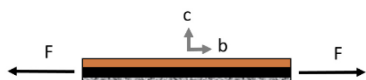
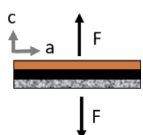
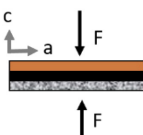
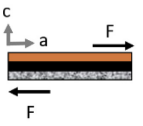
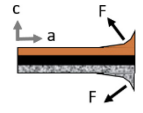
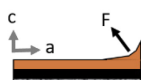
Type of stress		Limit (MPa)
Axial tensile		>700 MPa
Transverse tensile		10-100 MPa
Transverse compressive		>400 MPa
Shear		>19 MPa
Cleavage		<1 MPa
Peel		< 1 MPa

Table 1:2 Mechanical strength of REBCO tapes for several stress. Data taken from [25].

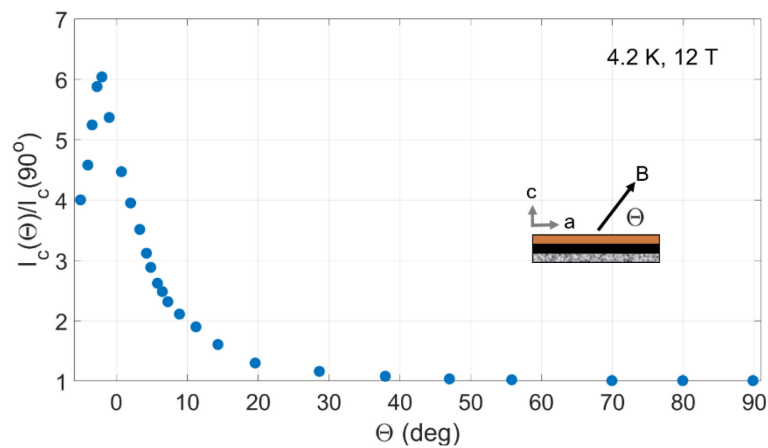


Figure 1:6 The normalized critical current vs the angle between the tape ab plane and the magnetic field. The data are taken for the Superpower tape from [26]. The tape depicted is the transverse cross section.

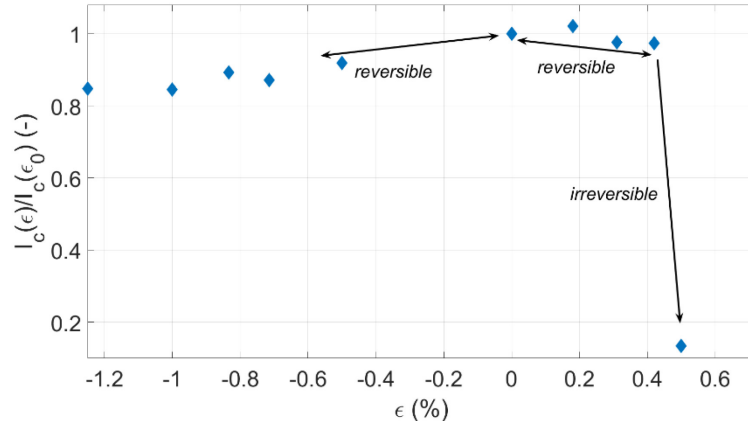


Figure 1:7 The normalized critical current vs the longitudinal strain. The measurements is done on a Shanghai Superconductor Technology (SST) tape at 77 K, self field.

1.3.2. The cables

Superconducting magnets should have a low self-inductance L in order to have a fast charge/discharge time constant τ ($\tau \propto L$) and to reduce the voltage (max 10 kV). At a given magnetic energy stored in the magnet, the voltage is inversely proportional to the current in the conductor ($V=2E/(It)$). Therefore, in large magnets, cables with large values of ampere/turn must be used. Because of the large operating current, hundreds of tapes should be assembled in the cable. One way to do it is to use the Twisted Stacked-Tape Conductor (TSTC), proposed by MIT in 2012 [27]. A stack of tapes is twisted longitudinally and contained in a rigid structure, made of stabilizing material (usually copper). This unit is called strand. Many strands are then cabled together around a core to form a large current cable. Finally, the cable is wound in a magnet. A complete review of other HTS cable options for fusion application can be found in [28] and [29]. In the Swiss Plasma Center (SPC) TSTC strand design, the stack of tapes is placed between two half cylindrical copper profiles (with a rectangular groove), resulting in a round strand. The copper profiles are annealed, resulting in a much lower elastic limit. This is beneficial to the cabling process, because the copper profiles plastically deform. Afterwards, the strand is twisted and soldered. In this way, the strain is kept lower than first soldering and then twisting [30]. The soldered junction between the two half copper shells is called split line. The soldering reduces the inter-tape and stack-copper electrical resistance, distributing evenly the current in the stack and facilitating the path for the current in the current sharing regime [31]. Moreover, this facilitates the redistribution of the current in case of tape defects [32]. The strands are then cabled around a flat copper core. The final conductor has then two twist pitches: one at the strand level and one at cable level. The conductor is cooled by forced flow helium, passing in the voids around the strands. SPC fabricated and tested in 2015 a 60 kA / 12 T prototype conductor [33] based on the twisted stack concept, see Figure 1:8. The initial I_c was within a few percent of the value expected from tapes I_c . The electromechanical test in SULTAN showed the strand mechanical limits under cyclic loading: I_c degraded progressively under electromagnetic cycling. The limitations of the 2015 conductor are that the peak tensile strain on the ceramic too close to the critical limit (about 0.6%) and the transverse load stress in operation (10 MPa), only marginally lower than the critical value (20 MPa) [34]. Two modified designs were proposed, which might be used in the Hybrid CS EU DEMO design proposed by SPC. In the hybrid CS, the cross section and type (REBCO, Nb_3Sn , $NbTi$) of superconductor is adjusted upon the value of the magnetic field seen by the different layers of the magnet [35]. This type of magnet is called graded.

This cable concept has also been adopted by KIT, designing the CrossConductor (CroCo) [36], in which the current density is increased by the use of two different tapes width, allowing to better fill the round strand cross section, as sketched in Figure 1:9 a). The stacking, twisting and soldering it is done in one single manufacturing step. Electromechanical tests (bending and transverse pressure) were done on the strands, and the design and manufacturing of the full cable is under development.

The cable design of ENEA is different. Instead of manufacturing strands, a round slotted aluminium core is extruded continuously and the stacks are placed in the slots. In the middle of the core, there is a hole for the helium flow [37], see Figure 1:9 b). The tapes are not soldered. In [38] was showed that the intertape electrical resistance is kept low. The concept of slotted core was pursued also by Commonwealth Fusion Systems (CFS). In this case, the core is in copper and the stacks are soldered by vacuum pressure impregnation (VPI) solder process after magnet winding. The vacuum pressure impregnated, insulated, partially transposed, extruded, and roll-formed (VIPER) cable was tested in SULTAN in 2019, and showed very good mechanical performance under cyclic loading.

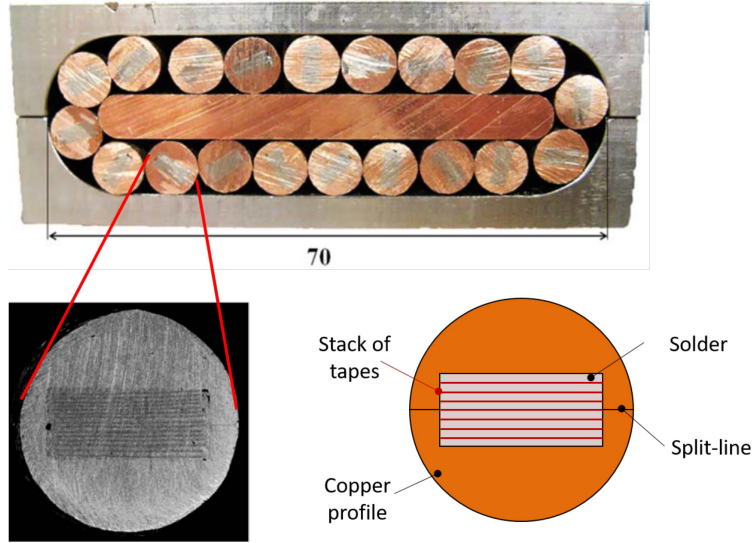


Figure 1:8 On the top the TSTC SPC 2015 cable prototype, taken from [39]. In the bottom left corner, the cross section of a strand (picture taken from [40]). In the bottom right corner, an artistic sketch of the strand.

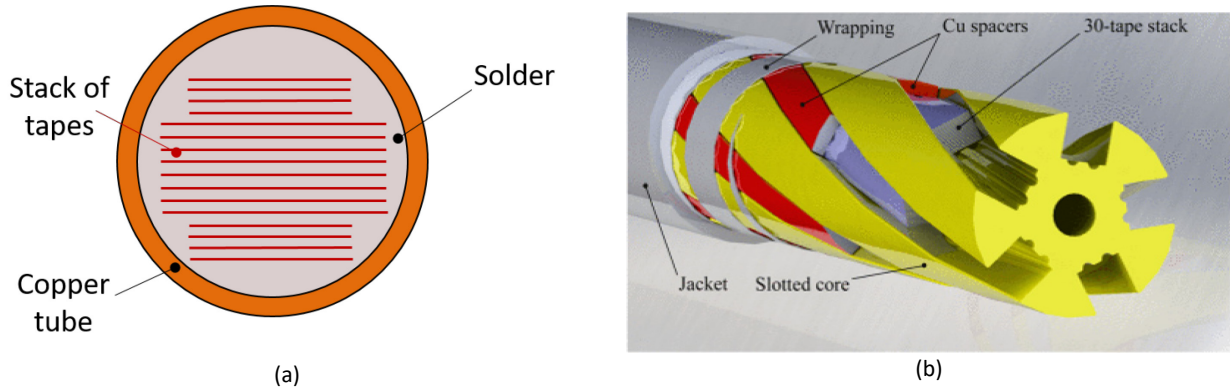


Figure 1:9 a) The sketch of the CroCo strand. b) The ENEA slotted-core cable-in-conduit-conductor. Picture taken from [37].

1.4. Scope of the thesis

This thesis is focused on the twisted soldered stack conductor concept developed by SPC, for the application in EUROfusion DEMO Hybrid Central Solenoid. Two independent aspects are treated:

- Quench** (Chapter 2). The aim is to observe the quench in an HTS conductor, reaching high temperature (above 200 K on the strand) and high voltage (~ 0.8 V on 3.6 m). Four REBCO conductors have been manufactured and tested. They are sub-size versions of the cable designed for the EU DEMO Hybrid CS. Their quench behaviour is studied in a Quench Experiment campaign in the upgraded SULTAN facility, to evaluate the safety of the conductor designs in terms of rising speed of the temperature. Moreover, this experiment is used to validate multi-physics code, which is an essential tool in magnet design. The upgrade of the SULTAN facility, needed to provide enough power during the experiment, is presented. The manufacturing of the cables and the instrumentation of the sample are described. The $I_c(B, T)$ and $T_{cs}(B, I)$ of the conductor are measured to characterize the conductor. The evolution and distribution along the length of the temperature and electric field during the quench are reported. A multi-physics model is used to interpret the experimental results and to assess the quench behaviour in case of a uniform magnetic field.
- Mechanical robustness** (Chapter 3). The goal is to quantify the mechanical limit against the electromagnetic force that the cable has to face under operation. Several strand designs are tested under transverse pressure in liquid nitrogen and self-field. This test is crucial, because it allows quantifying the critical pressure at which the critical current reduction under transverse pressure is irreversible before manufacturing a full size cable. A finite element mechanical model is developed to explain qualitatively the effect of few design parameters and to guide the design towards a better performance. First,

the cable designs are presented. Then, the results of the transverse pressure tests are reported. Finally, the mechanical model of the soldered strand is illustrated and the results discussed.

Chapter 2 The Quench Experiment

After providing the background and the motivation for the Quench Experiment, the upgrade of the SULTAN facility is reported. The section 2.2 describes the peculiarities, the manufacturing and instrumentations of the Quench Experiment conductors. After the explanation of the variables explored during the test campaign (section 2.3), the DC performance is assessed in the section 2.4: the $I_c(T, B)$ and $T_{cs}(I, B)$ are measured and compared with the expected ones, coming from the tapes measurements and the scaling law of the conductors estimated. In the section 2.5, the results of the Quench, in terms of temperature (cable, He and jacket) and electric field evolution and distribution along the length are presented. The normal zone propagation velocity in the different conductors is estimated. The results of a model built using the THEA code are compared to the Quench Experiment data in the hot spot, to further understand the physics of the experiment (section 2.6). The code is used to confront the quench in case of a confined magnetic field (like in SULTAN) and the more realistic scenario for the CS of uniform magnetic field (section 2.7).

2.1. The motivation

To operate a magnet safely, it is crucial to design a reliable quench detection system. A voltage detection system may not be effective for HTS magnets, because the normal zone propagation velocity is about one/two orders of magnitude slower than in LTS [16] due to the high temperature margin. Therefore, the hot spot temperature may have reached very high values, able to damage, even to burn, the magnet, before the quench is detected. Consequently, the quench in HTS magnets is less probable than in LTS but more difficult to detect. Till this moment, the quench evolution was addressed, especially by multi-physics codes. Some of the analysis were done using commercial or in house codes in high current cables [41] [42] [43] and in Tokamak [44] [45] and Helical reactor magnets [46] to study the hot-spot temperature evolution in the case of exponential current discharge after the quench detection. Experimentally, the quench was studied mostly on low current conductors [47] and just a few experiments were performed on high current cables in a prototype magnet for accelerator [48]. Quench experiments on Nb₃Sn were performed in SULTAN in the 90's, called QUELL (QUEnch on Long Lengths), using the horizontal access port [49], necessary because of the bigger than usual sample dimensions. This configuration, that requires several months for the sample installation, is not necessary for the Quench Experiment considered in this work. Quench tests were carried out on VIPER, a high current HTS fusion conductor for DC Tokamak magnets [50], but only the initial quench phase could be investigated [19], because the SULTAN superconducting transformer, which routinely charges the sample, can sustain very little voltage (i.e. sample resistance should be < few nΩ). As soon as the sample resistivity increases, which is the case during the quench, the transformer current drops to zero, not allowing the observation of the fully developed quench (see Figure 2:1). As a consequence, the work reported in this section has the aim to finally provide to the fusion community a Quench Experiment (QE) on HTS sub-size conductors for fusion application, whose copper-steel cross section ratio and copper current density are relevant for the EU-DEMO CS. The quench was sustained till high temperature (above 200 K) in the hot spot of the cable are reached. At such temperatures, the quench is fully developed. This allows to estimate the temperature rate of increase in the hot spot and the normal zone propagation velocity. These results are discussed in the framework of the safety of the magnet in case of voltage detection system. Moreover, the QE can finally provide the data to validate the multi-physics codes, to be then used as predictive tools in the magnet design phase. Due to the SULTAN transformer limitation exposed before, the facility had to be upgraded, replacing the transformer with a power supply (18 kA, 10 V). The sample is connected to the power supply through 15 kA current leads. The current leads can carry a maximum of 15 kA due to space restriction in the sample holder. Further details about the SULTAN upgrade are reported in [51]. Four REBCO conductors (forced-flow, up to 15 kA) have been manufactured at SPC, based on the same twisted stack concept that was considered in [35] for the EU-DEMO Central Solenoid. One of the four conductors (#1, the reference conductor) is simply a scaled down version (only three strands, 15 kA instead of 51 kA) of the conductor in [35], while each of the other three conductors has one specific layout modification.

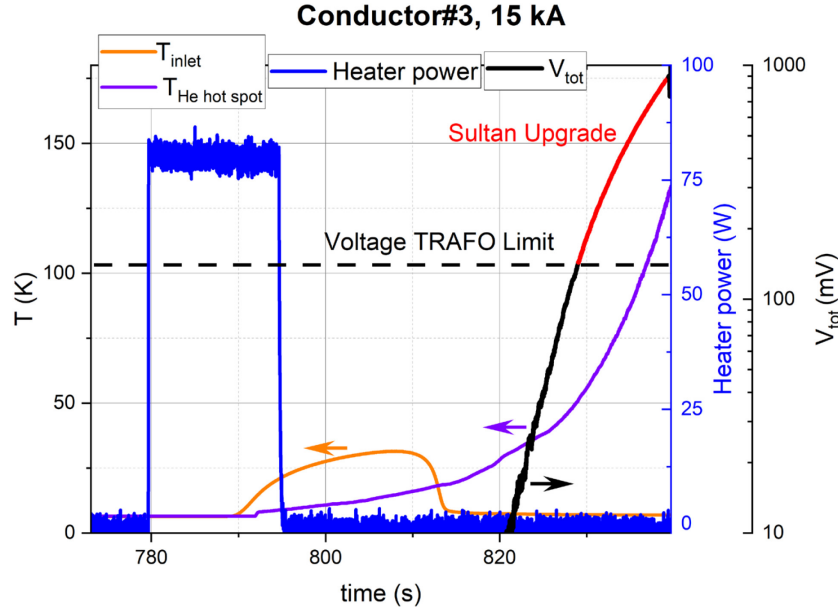


Figure 2:1. The evolution of the temperature (left axis) and voltage (right axis, black and red curve) after that the quench is triggered in the Conductor#3 at 15 kA by warming up the inlet helium through a heat pulse (blue curve). The maximum voltage that can be reached by the usual SULTAN set up to charge the primary (using the transformer TRAFO) is depicted by the black dashed line. The red part of the voltage curve highlights the voltage range that the SULTAN upgrade allows to observe.

2.2. The Quench Experiment Conductors

2.2.1. The conductors

The conductors used for the Quench Experiment are sub-size conductors based on the SPC TSTC concept, as presented in the section 1.3.2. Sub-size means that the critical current should not exceed 15 kA at 11 T. The copper and steel cross sections are scaled-down as well, in order to keep the same current density in the copper as in the full size conductor and the same steel/Cu ratio [41], see Table 2:1. The sub-size cables are made of a strand triplet, whose twist pitches (in twisted conductors, #1, #2, #4) are: 400 mm at the strand stage, 1000 mm at the cable stage. To manufacture the strands a fountain solder bath is used (Figure 2:2). The solder used is $\text{Sn}_{40}\text{Pb}_{60}$.

As shown in Table 2:1, four REBCO conductors were manufactured. The first conductor, the “reference” one (#1), has twisted, soldered strands. The second one (#2) has twisted but not-soldered strands (tapes are not soldered together). The third (#3) has not-twisted, soldered strands, with the tapes wide face perpendicular to the magnetic field. The fourth (#4) is twisted and solder-filled ($\sim 135 \text{ mm}^2$ of solder) in the space between strands and steel jacket. The four conductors were assembled in three SULTAN samples. A test campaign was dedicated to each SULTAN sample.

The He cross section in all the conductors is 93 mm^2 . It is in direct contact with the strands, flowing between them in all the conductor design, except for Conductor #4, where there is a dedicated channel. The REBCO tapes ($50 \mu\text{m}$ Hastelloy substrate, $10 \mu\text{m}$ copper per side, width of 3 mm, 25 tapes per stack) were purchased from Shanghai Superconductor Technology. The copper shells are not-annealed and the tape face is perpendicular to the split-line, the soldered junction between the copper shells. It has been experimentally proven that this configuration allows the strand to sustain better the transverse pressure [34]. Only the edges between the copper shells are soldered in the not-soldered strands, the solder is absent from the inner space where the tapes are placed. Instead, the ends of the strands are filled by the same solder as used in the termination of the conductor.

The triplet was cabled and inserted in the jacket (an 8.5 mm thick stainless steel tube). Then the jacket was compacted by crimping to close the insertion gap. The conductors’ termination (length 450 mm) are fabricated inserting the triplet in a copper sleeve, later crimped and filled by $\text{Bi}_{57}\text{Sn}_{42}\text{Ag}_1$ solder, whose melting temperature of $137\text{-}139 \text{ }^\circ\text{C}$ is lower than that of $\text{Sn}_{40}\text{Pb}_{60}$ ($183\text{-}191 \text{ }^\circ\text{C}$) to ensure that the solder in the strands doesn’t melt while the termination is filled. The $\text{Bi}_{57}\text{Sn}_{42}\text{Ag}_1$ solder is selected to fill the solder-filled

conductor because it does not change volume during solidification and it has low thermal expansion coefficient [53]: the risk of detachment of the cable + solder body from the jacket during the sample's cool down is reduced. The He inlet is placed above the bottom termination and the outlet before the upper termination (see Figure 2:3). The terminations are therefore cooled just by conduction.



Figure 2:2. The fountain solder bath used to solder the strand.

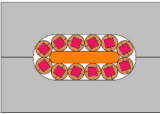
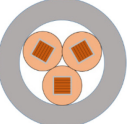
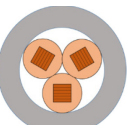
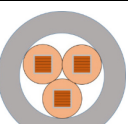
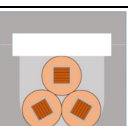
	Conductor	SULTAN Sample	Cu cross section (mm ²)	J_{cu} (A/mm ²)	I_{op} (kA)	Steel cross section (mm ²)	Cu/steel ratio (-)
	Full size	/	574	89	51	2588	0.22
	Reference (#1)	1 and 3	150	100	15	715	0.21
	Not-Soldered (#2)	1	150	100	15	715	0.21
	Not-Twisted (#3)	2	150	100	15	715	0.21
	Solder-filled (#4)	2	150	100	15	652	0.23

Table 2:1 The list of the conductors for the Quench Experiment and the full size conductor.

2.2.2. The sample instrumentation

The SULTAN sample is made of two conductors, called “legs”. Each leg is cooled independently. The inlet pressure in the sample is 10 bar. Two heaters per leg are attached to the He pipe upstream to the inlet. These heaters are used to heat up the helium that triggers the quench in the conductors. The mass flow rate is measured at the outlet. The inlet and outlet pressure are also measured. Under normal conditions, the Helium provided by the cryoplant slightly heats up before it reaches the test well. The minimum inlet temperature of the sample is about 6 K at the maximum mass flow rate.

The two legs of the SULTAN sample are electrically connected in series by a joint at the bottom of the sample (see Figure 2:3). At the top, the sample is connected to the current leads. The sample is instrumented with temperature sensors (Cernox®) and voltage taps. The distance between voltage tap pairs is 200 mm outside the High Field Zone (HFZ), whose length is 440 mm. The quench will likely start in the HFZ. Therefore, to have a better localization of the hot spot and description of the electric field profile close to it, the

distance is shortened to 100 mm inside of the HFZ. An array of four pairs of voltage taps across the whole HFZ is used to assess the T_{cs} and I_c , in case of non-equipotentiality, by averaging the signals. Both the helium and the jacket temperature were measured, in order to quantify the temperature gradient in the cross section, that was qualitatively evaluated in the numerical simulations reported in [41]. The helium and jacket thermometers are located at the same longitudinal position of the sample, according to instrumentation sketch in Figure 2:3. The jacket [54] thermometers are simply glued to the steel. On the other hand, the helium thermometers are intrusive into the conductor: first, six holes were drilled in the jacket. Then a protruding threaded part was welded. Afterwards, the thermometers were inserted in the holes and fixed (and leak-tight) by screwing a Swagelok® fitting [55]. In this way, the thermometer measures the temperature of the flowing helium. In the solder-filled conductor, they are located on the opposite side of the helium channel, to measure the temperature closer to the strands. In addition, the temperature is measured also in the inlet, outlet, and at the top termination, for each leg (see Figure 2:3). It was not possible to have a finer spatial discretization for the voltage taps and thermometers, due to the maximum allowed number of channels in the Data Acquisition System.

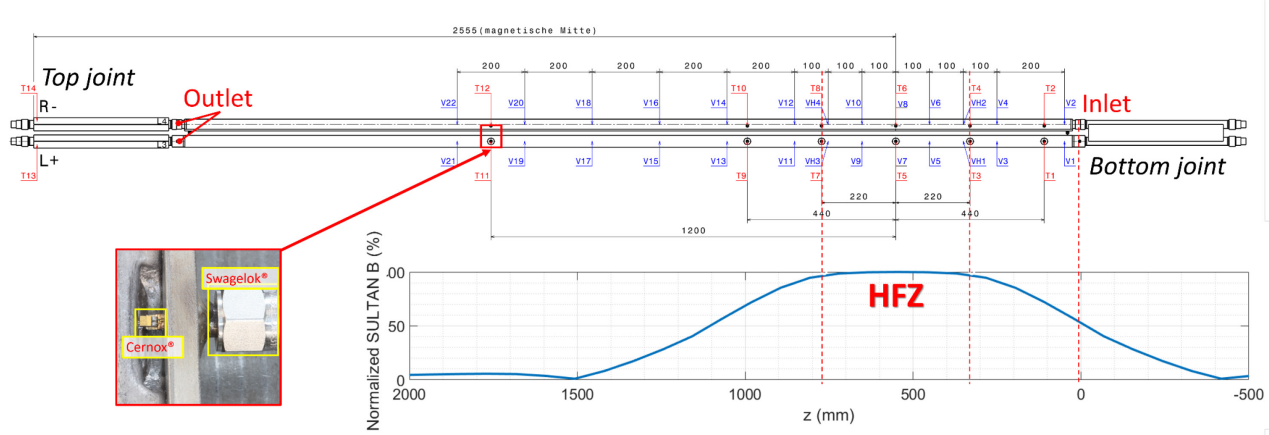


Figure 2:3 The sketch of the sample instrumentation and the Sultan magnetic field distribution along the sample length. The zero of the z coordinate is placed at the He inlet of the sample. The HFZ is highlighted. Voltage taps in blue, temperature sensors in red. The He temperature sensor is shown in the bottom left corner.

2.3. The test campaign

The experiment on a sample (two conductors) is divided in two parts: 1) DC performance of the conductors 2) quench evolution (Quench Experiment). During the DC measurements, I_c and T_{cs} were assessed at different magnetic fields and temperatures, to characterize the conductor and to obtain the data for the $I_c(B, T)$ scaling law. The Quench Experiment has been carried out on the two conductors in separate runs. The quench was triggered by heating up the He, and this could be done in two ways: rapidly (heat slug) or slowly. The current switch-off criterion in the first two campaigns was based on temperature. As soon as the maximum temperature among all the thermometers (He and Jacket) overcomes 150 K, the current is dumped. At the chosen threshold, the quench is fully developed and the safety of the conductor is not compromised. After the first two campaigns, the criterion has been changed. After having verified that the gradient between conductor, helium and jacket temperature was quite high, in order to have a better control on the strand temperature, the current dump criterion was based on the total voltage. In the section 2.5.1, the method to estimate the cable temperature from the voltage is explained. To discharge the current, a fast discharge rate (200 kA/s) was used. The Quench Experiment has been carried out also at different mass flow rates, magnetic fields and operating currents (see Table 2:2).

Parameter	Values
Quench trigger	Heat pulse or Slow heating
Sample current (kA)	9.5–15
Mass flow rate \dot{m} (g/s)	1.5 or 3

Table 2:2. The summary of all the values of the parameters used during the Quench Experiment.

2.4.The DC characterization

The DC assessment is needed for several reasons:

- To check if the conductor has the expected performance obtained from tapes I_c ;
- To characterize of the conductor. The scaling law obtained will be used in the computational model. In this respect, data at different magnetic field are needed. Since the model has the goal to simulate the performance during the quench, the useful points for the scaling law are in the “neighbourhood” of the selected magnetic field for the quench runs;
- To identify the initial conditions, namely in terms of magnetic field, at which to perform the quench experiments at full current, at the designed copper current density (~ 100 A/mm²);
- To identify the I_c distribution in the High Field Zone and the weak points in the conductors, where the quench can initiate;
- To quantify of the loss of performance after the combination of quenches and EM loads.

2.4.1. Check of the expected conductor performance

The SST tapes used for the QE conductors have the characteristic shown in (Table 2:3). In Table 2:4 the composition of the conductors strands is shown. Such composition was selected to obtain a similar average conductor critical current at 77 K among all the different designs (~ 5000 A), computed taking into account the average I_c of each spool.

Spool #	34	35	36	37	38	39
Width (mm)	3					
Hastelloy thickness (μ m)	50					
Average I_c (s.f.,77 K) (A)	122	132	96	143	126	137
Min I_c (s.f.,77 K) (A)	111	113	78	120	106	94
Max I_c (s.f.,77 K) (A)	138	150	128	161	147	168
$I_c \sigma$ (%)	3.5	4.1	7.7	2.9	4.4	8.8
Spool Length (m)	133	147	135	133	136	520

Table 2:3. Features of REBCO tapes purchased by SST.

Conductor	# tapes from 34	# tapes from 35	# tapes from spool 36	# tapes from spool 37	# tapes from spool 38	# tapes from spool 39
#1			18	30		27
#2	25	50				
#3			12	6	6	51
#4			6		30	39

Table 2:4 Conductor stack composition (number of tapes from each spool, the total number of tapes in one conductor is 75).

A model was used to compute the expected critical current at 77 K, s.f. in the cross section of the strand starting from the tape I_c and considering the strand self-field distribution. It was assumed that the critical current is constant along the length. The geometrical x-

y domain was divided using N_x and N_y nodes. The critical current for each node in the stack domain is used as input of the model to compute the magnetic vector potential A , in case of rectangular shape [56]. The initial guess $\overline{I_{c,stack,0}}$ is the same for all the nodes: it is the average of the critical current in the stack, according to the SST data (Table 2:3, Table 2:4, Appendix A-Figure A:0:1). The self-field distribution is found according to Equation 2:1. The critical current in the stack domain is recomputed taking into account to the magnetic field magnitude and orientation, according to the data reported in [57]. The updated critical current is used to compute again A . The loop continues until a certain error between the old and new self-field in a specific x-y point (where the gradient is the highest) is lower than a certain threshold. The conceptual scheme of the iterations is depicted in Figure 2:4. The final I_c and self-field distribution is illustrated in Figure 2:5. The I_c of the strand is computed as the sum of the I_c in the nodes in the stack domain. The final expected critical currents in the conductors (three time the I_c of one strand) are: 4924 A in the #1, 5000 A in the #2, 5026 in the #3, 5250 A in the #4. The difference in the values comes from the non uniform distribution of the I_c of the spool#39 (see Appendix A-Figure A:0:1).

$$B = \nabla \times A$$

Equation 2:1- The self-field in the stack B is computed as the curl of the magnetic vector potential A

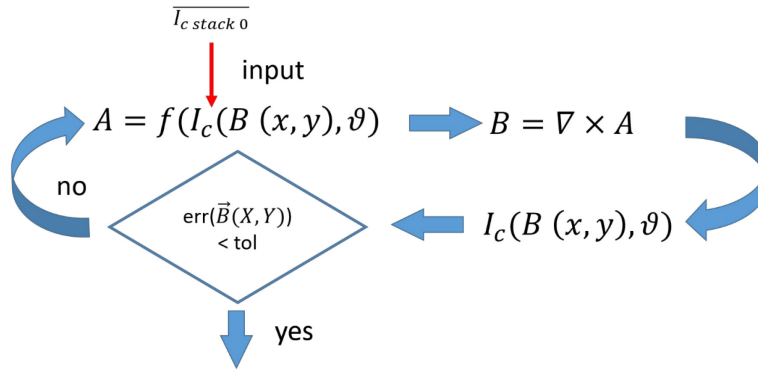


Figure 2:4 Conceptual scheme of the model to compute the critical current and self-field distribution at 77 K.

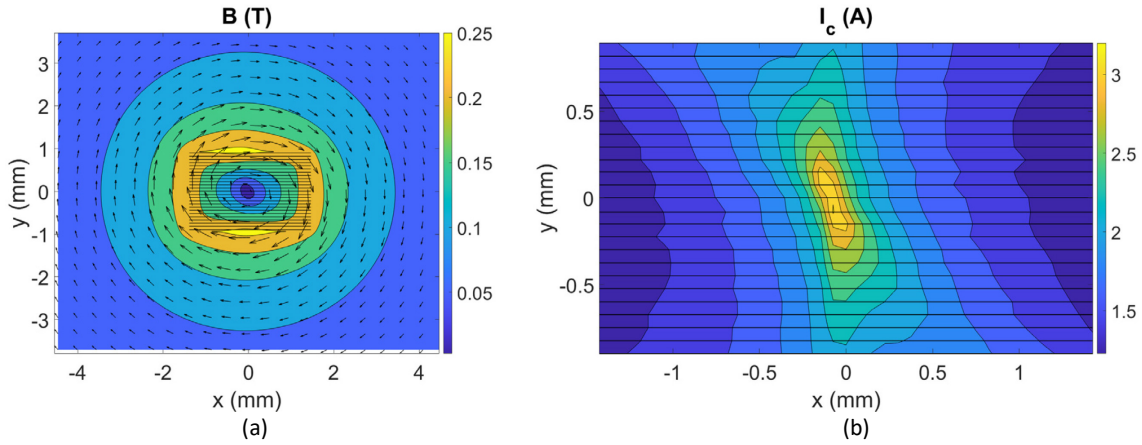


Figure 2:5 a) The self-field of one strand of the Conductor#1. b) The I_c distribution in the stack of the strands belonging to the Conductor#1. For the strands of the other conductors, the B and I_c distribution are very similar but the values are slightly different.

The strands were tested before the cabling at 77K in self-field by four probe methods. Several regions were investigated to check the uniformity of the critical current along the length (see the voltage taps sketch in Figure 2:6). The I_c distribution along the length at 77 K-s.f. is shown in the Figure 2:7. The I_c presented is the sum in a certain region of the three strands belonging to the same conductor. None of the strands exhibited an early voltage. The conductors show a quite uniform I_c along the length (maximum standard deviation is 1.5 % on the Conductor#1). The different average I_c among the different conductors come from the variability of the I_c along the tape (see Appendix A- Figure A:0:1).

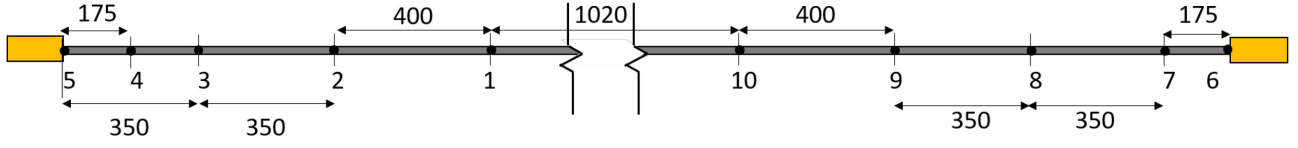


Figure 2:6: Sketch of the instrumentation with the voltage taps label and the distances (in mm) used to measure the strand of the conductors at 77 K, s.f.

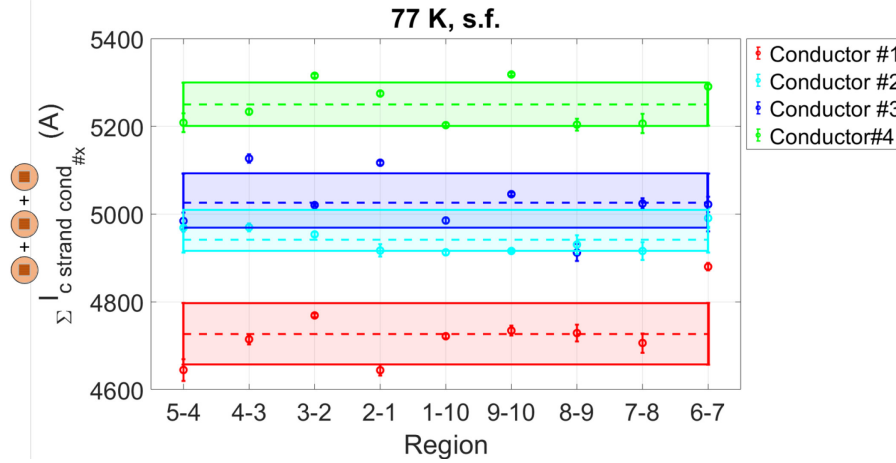


Figure 2:7 Measured I_c along the length in different regions (Figure 2:6) at 77 K, strand self-field for the different conductors. The symbols denote in a certain region the sum of the three strands belonging to the same conductor. The error bar on each symbol represents the repeatability of the measurement. The dashed lines represent the mean on the different regions for each conductor. The shaded area is the standard deviation on the different regions for each conductor.

Comparing the sum of the measured I_c of the strands belonging to the same conductor with respect to expected one obtained by the analytical model, it is possible to see that no major degradation is present for any of the conductors (Figure 2:8) after the strand manufacturing. The Conductor#1 and Conductor#4 have a slightly higher difference in $I_{c,measured}/I_{c,expected}$ ratio with respect to the 100 % that could be reasonably explained by the variability along the length of the I_c of the tape, especially for the tape belonging to the spool#39 (see Appendix A-Figure A:0:1).

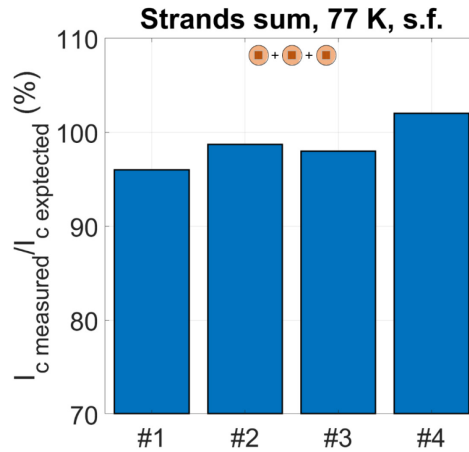


Figure 2:8 The relative ratio in percentage of the measured critical current with respect the one expected at 77K, self-field for the different conductors. The value considered for the ratio is the sum of the critical current on the strands belonging to the same conductor.

The tapes were measured at 4.2 K and at several fields in the perpendicular direction (Figure 2:9) to compute the expected critical current of the conductors in the SULTAN experiment. The scaling law (Equation 2:2) was estimated by fitting the measured I_c at different fields. The goal was to find the parameters θ , p , q (Table 2:5) that control the dependence with the magnetic field. They will be used in the fit of the conductors measurements. Having less free parameters, α and A could be estimated with less uncertainty. The α value reported in the (Table 2:5) is not the final one: α controls the temperature dependence and cannot be properly estimated from the tapes measurements, since they were done just at 4.2 K. The REBCO B_{irr0} and T_c are taken from [41].

$$I_c(B, T) = \frac{A}{B} \left(\frac{B_{irr}(T)}{B_{irr0}} \right)^\beta b^p (1 - b)^q$$

$$B_{irr}(T) = B_{irr0}(1 - t)^\alpha$$

$$b = B/B_{irr}(T)$$

$$t = T/T_c$$

Equation 2:2- The scaling law equation for the critical current as function of magnetic field and temperature.

Spool	B_{irr0} (T)	T_c (K)	α	β	p	q	A
36	120	92.83	1.75	1.5	0.4921	0.5359	5095
38	120	92.83	1.75	1.5	0.4921	0.5359	7677
39	120	92.83	1.75	1.5	0.4921	0.5359	7196

Table 2:5. The parameters of the scaling law for the tapes obtained by the measurement on the tapes at different field at 4.2 K, in perpendicular direction.

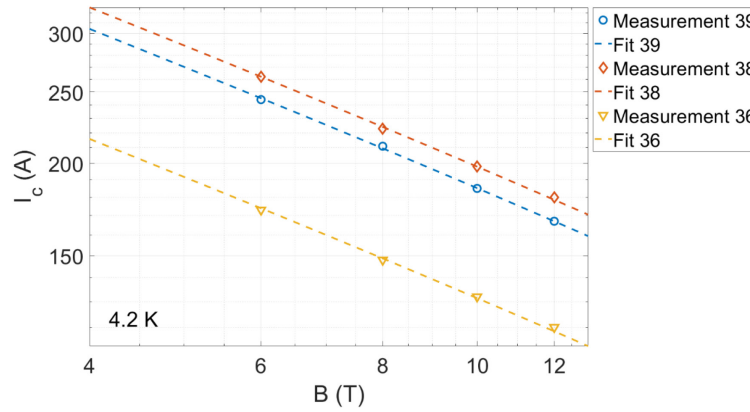


Figure 2:9 The I_c of REBCO tapes measured at different magnetic fields at 4.2 K a) with the fit obtained by the scaling law. The scale for both axis is logarithmic.

The expected critical current at a certain field at 4.2 K was computed from the critical current measured on the tapes that constitute the strand at that field at 4.2 K (Equation 2:3).

$$I_{c\ cable}(B, 4.2\ K) = \sum_{j=1}^{N_{strand}} \sum_{i=1}^{N_{tapes/strand_j}} I_{c\ tape_i}(B, 4.2\ K)$$

Equation 2:3- The computation of the I_c in the cable starting from the I_c in the tape

In the SULTAN test, the inlet He temperature in the conductor was not 4.2 K but around 7 K, due to the configuration of the cooling circuit. The critical current at 7 K is obtained by multiplying the I_c at 4.2 K by 0.92, this factor is obtained by the scaling law of the conductor (see 2.4.2).

The Figure 2:10 shows the ratio between the measured I_c and the one coming from Equation 2:3 at 7 K, 10.78 T. For the Conductor#1, the I_c measured around 22% lower than the I_c expected from the tapes measurements. Moreover the n value of the Conductor#1 was 6, much lower than the ones of the Conductor#3 and #4 (12 and 14 respectively). A reason could be that the crimping could have damaged the conductor: the Conductor#1 is twisted (and soldered), so the effective diameter of the cable becomes larger than the designed dimension. The Conductor#2 is also twisted, but the tapes are not soldered to the copper profiles, allowing them to slide under transfer compression and so feeling less strain. The soldered conductor with the best agreement between the measured and the expected I_c is the Conductor#4, the only one that was not crimped. These results suggest that the crimping could be a risky manufacturing procedure for the soldered and twisted cable design.

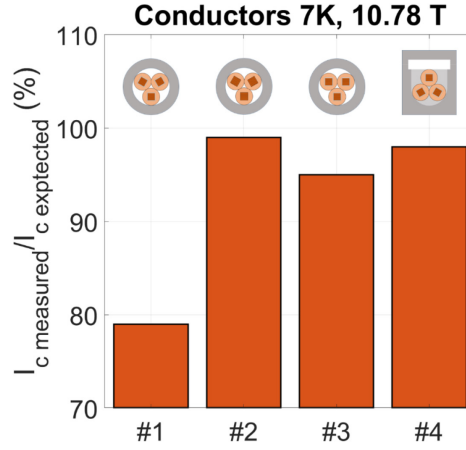


Figure 2:10. The relative ratio in percentage of the measured critical current with respect the expected one at 7 K, 10.78 T.

2.4.2. The Conductors scaling law

Having seen that some degradation was present in the conductors and due to the uncertainty of the α parameter (see 2.4.1), the scaling law was recomputed starting from the data collected during the DC characterization in the SULTAN experiment, in order to use these fits in the computational model to simulate the quench. The fit was just assessed for the Conductor #1, 3 and 4, because the Conductor #2 was damaged during the DC test campaign and it was not possible to perform any Quench Experiment on it. For this reason, it will not mentioned in the following sections. The scaling law was obtained from the fitting of the points in the phase space B, T, I assessed by I_c and T_{cs} measurements on the conductor. The temperature used for the scaling is the He for all the conductors except for the Conductor #4, since in this case, the jacket temperature is closer to the strand temperature than the He one. The β , p and q values come from the tape measurements (Table 2:6). The Figure 2:11 represents the measured I_c and the fit curves as function of temperature and at different magnetic fields. The estimated I_c of the conductor from the tape measurements at 4.2 K is also shown.

Conductor	B_{irra} (T)	T_c (K)	α	β	p	q	A
Conductor#1	120	92.83	2.48	1.5	0.4921	0.5359	3.8391e5
Conductor#3	120	92.83	2.425	1.5	0.4921	0.5359	4.9494e5
Conductor#4	120	92.83	2.481	1.5	0.4921	0.5359	5.2464e5

Table 2:6. The parameters of the scaling law for the conductors obtained by the DC measurement.

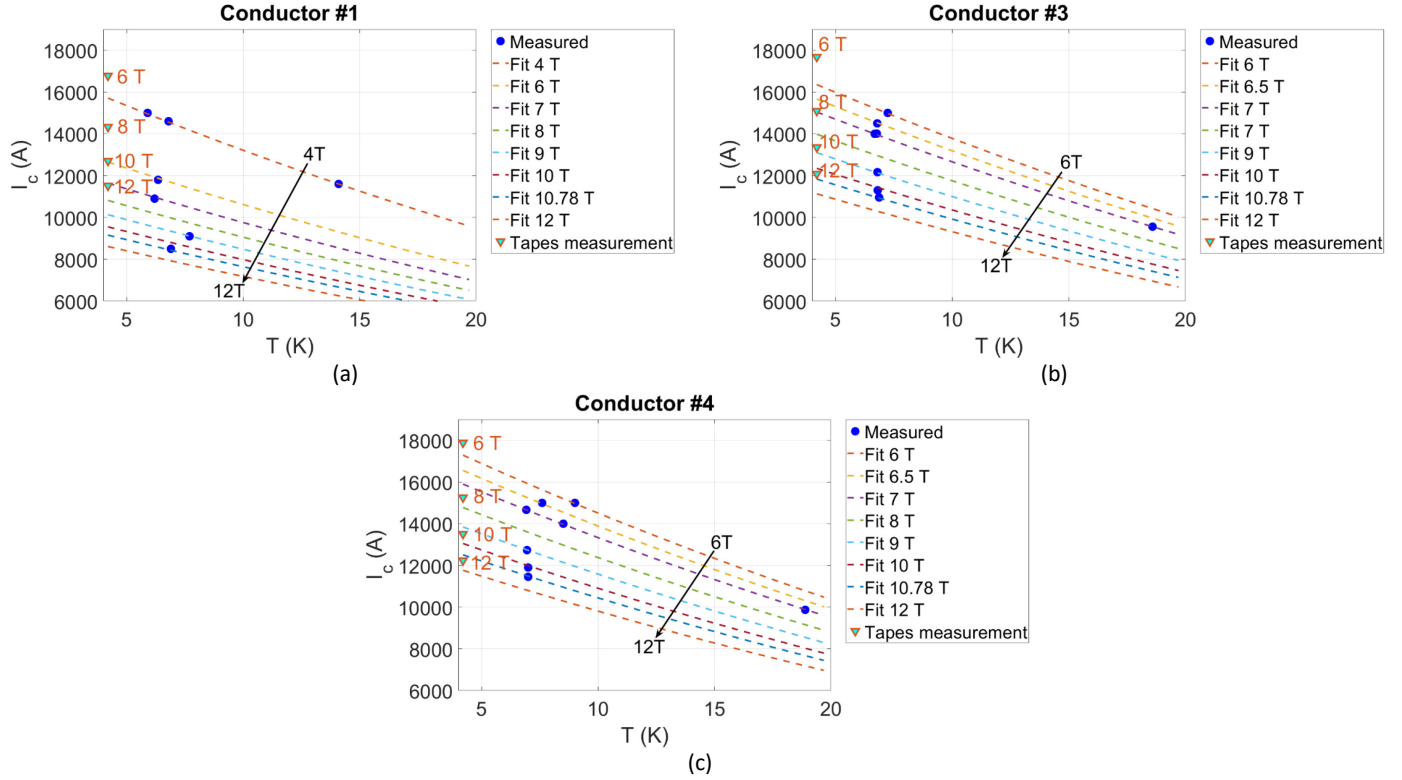


Figure 2:11 The I_c of the a) Conductor #1, b) Conductor #3, c) Conductor #4 vs temperature. The dashed lines is the value obtained by the scaling law at constant magnetic fields. The blue dots represent the DC SULTAN measurements, while the triangular points the expected I_c computed from the tapes measurements

2.4.3. The initial conditions for the Quench Experiment

At the SULTAN maximum field (10.78 T), the conductors have lower I_c than the design value (15 kA), hence the copper current density J_{cu} is lower than in full size fusion conductors (about 100 A/mm²). In order to operate at full current (15 kA) at ~ 7 K, the magnetic field needed to be lower than 10.78 T. The values of the magnetic fields for each conductor are reported in Table 2:7.

Conductor	B (T)
#1	3.5
#3	6
#4	6.5

Table 2:7 The selected fields for each conductor to perform the Quench Experiment at 15 kA, 7 K.

At such fields and temperature, the conductors were in the dissipative condition (electric field about 0.7-0.8 μ V/cm), rather than the zero resistive state at which the superconductor normally operates. This criterion was selected in order to reduce the energy and the time to carry out every single quench experiment with respect to the non-resistive case. Anyway, at such small electric field the helium cooling power was sufficient with respect the self-heating in the cable to have a stable value of electric field and temperature, even if the conductor is in current sharing.

In order to explore the effect of having a lower J_{cu} in the quench development, the experiment was performed also at higher magnetic fields (Table 2:8), keeping the criterion of 0.7-0.8 μ V/cm as initial condition for the experiment.

Conductor	I (kA)	J_{cu} (A/mm ²)	B (T)
#1	12/9.5	80/63	4/9
#3	11	73	10
#4	11	73	10.78

Table 2:8 The selected fields for each conductor to perform the Quench Experiment at lower current, starting from 7 K.

2.4.4. The I_c distribution in the High Field Zone

To identify the weak point (location of the minimum in I_c) in the HFZ of the conductor, the I_c measurements were taken.

The $I_{c,rel}$ is the I_c assessed using the finer positioning of the voltage taps (every 100 mm) in the HFZ with respect to the I_c assessed by the voltage taps placed across the whole HFZ (440 mm, VH voltage taps). The Figure 2:12 shows the I_c distribution for the three conductors. The Conductor#3 and #4 have a more homogenous distribution than the Conductor #1: the weak point has an $I_{c,rel}$ of ~ 96 %, while in the other two it is around 99%.

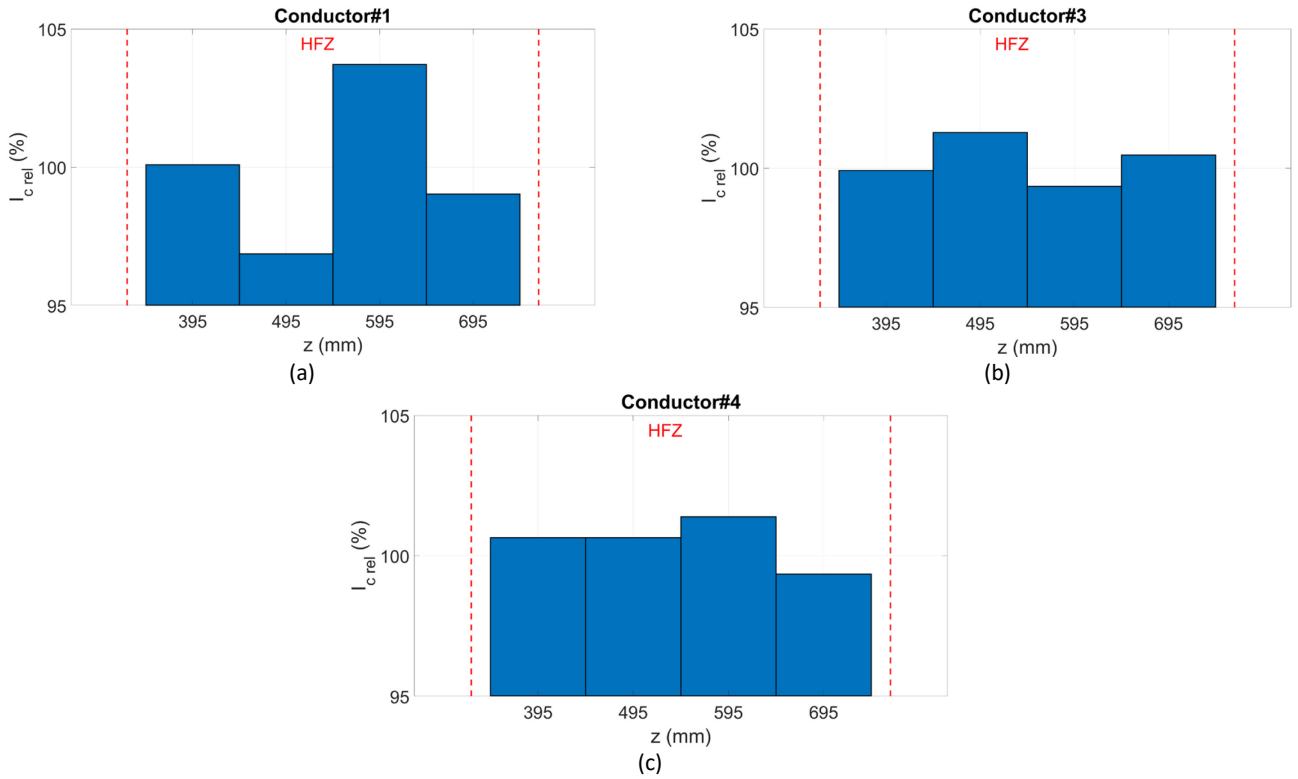


Figure 2:12 The I_c distribution along the conductor length in the a) Conductor#1, b) Conductor#3 and c) Conductor#4 in the HFZ, delimited in the picture.

2.4.5. The loss of performance

After having being exposed to a series of quenches and electromagnetic loading, all the conductors degraded. The performance reduction was quantified (Figure 2:13) as the percentage difference of amplification factor A of the scaling law at the beginning and at the end of the test campaign, since all the other parameters in Table 2:6 did not change. For the Conductor#1 the degradation was much smaller than the one that took place during the manufacturing, while, for the other conductors, it is the same order. The Conductor#4 degraded less thanks to the solder filling: it is the more mechanically robust, and the conductor reached lower temperature than the other ones. In the sections 2.5.2 and 2.6.2.2, it is shown that at a given temperature of the hottest region (He or jacket), the temperature of the conductor in the Conductor#4 is lower than the other ones, thanks to the bigger inertia and the lower cable-jacket thermal resistance.

There are two possible explanations for the loss of performance:

- The mechanical damage induced by the thermal gradient;

- The mechanical damage induced by the EM cycling.

It is not clear which one is the dominating, because to any quench experiment corresponds a cycle.

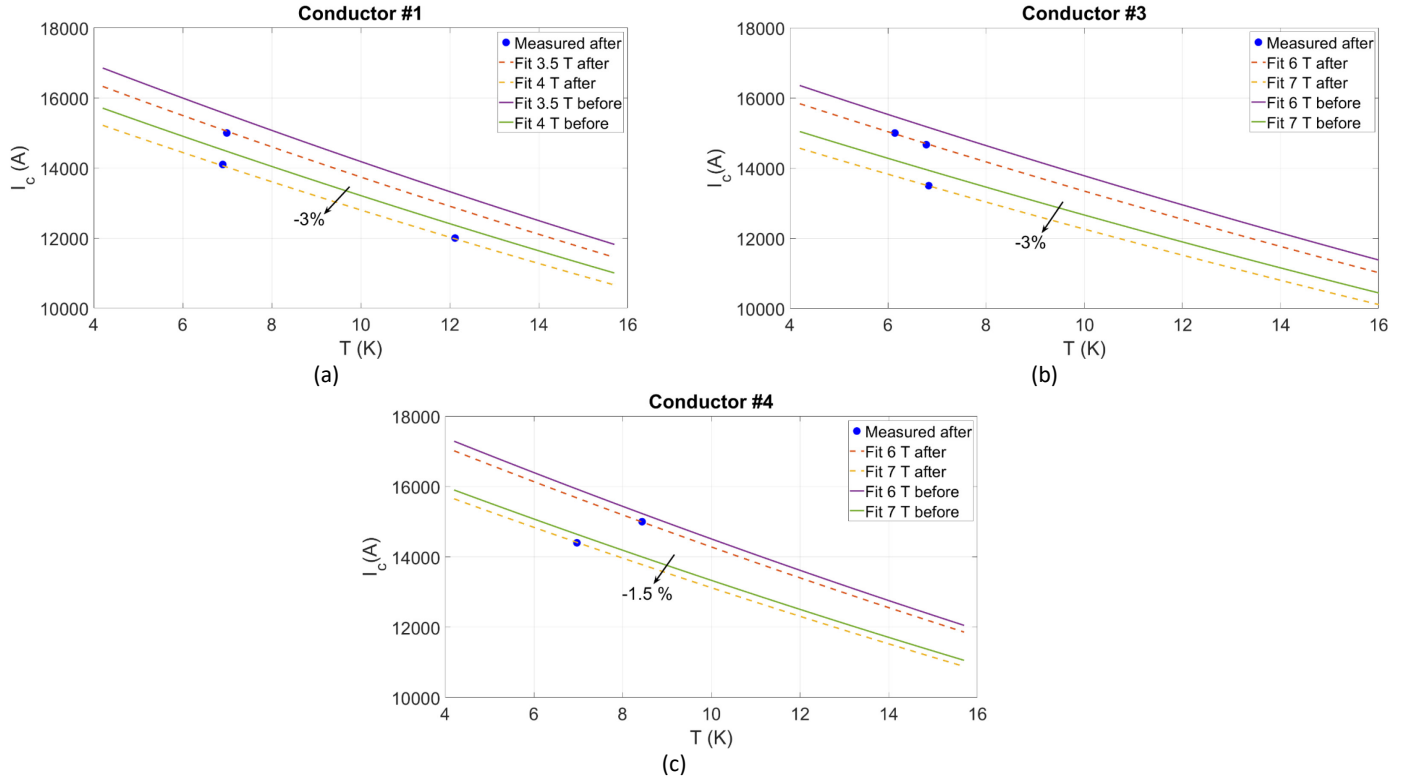


Figure 2:13 The critical current of the a) Conductor#1, b) Conductor#3 and c) Conductor#4 vs temperature. The dashed lines is the value obtained by the scaling law at constant magnetic fields after the quenches and EM loads, obtained by the blue dots, the DC SULTAN measurements. The continuous lines denote the scaling law at the beginning of the test campaign.

2.5. The Quench Analysis

2.5.1. The Cable temperature estimation

The cable temperature T_{cable} was not directly measured during the experiment. However, it could be estimated from the voltage signal with the assumptions that: 1. the superconductor does not carry the current; 2. the three strands have the same voltage (and so temperature); 3. the copper temperature is representative of the cable temperature, because the copper profiles represent 89% of the cable mass, the rest consisting of tapes and eventually solder in between the tapes and knowing the temperature dependence of the strands copper (Cu), the stainless steel jacket (Ja) resistance and the $\text{Bi}_{57}\text{Sn}_{42}\text{Ag}_1$ solder for the solder-filled conductor. One can say that the copper works as a thermometer, because the resistance (and the corresponding voltage at constant current) is proportional to the temperature.

From Figure 2:14, where the critical current of the different cables is plotted as function of temperature, it is possible to see that the current in the superconductor is close to zero around 70 K, validating the assumption 1 true, from around 70 K on. Consequently, the assumption number 1 limits the analysis to temperature above 70 K. This is acceptable because the interest is on the high dissipative range, when the current flows just into the copper and the rising speed of the temperature is faster.

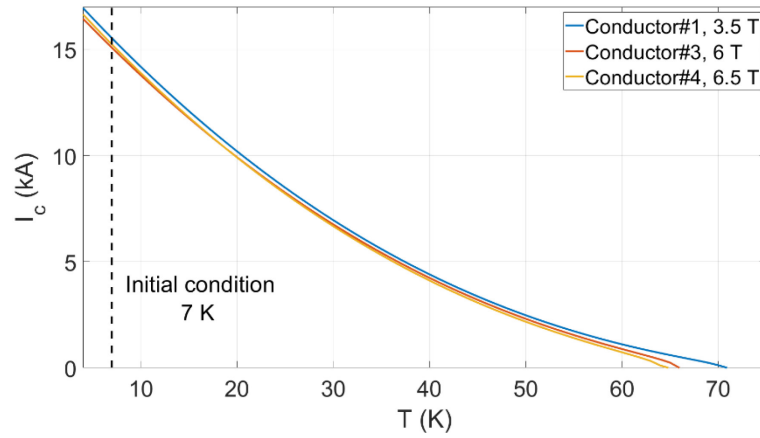


Figure 2:14. The critical current vs temperature at the magnetic field selected for each conductor for the Quench Experiment at full current-low field. a) Conductor #1. b) Conductor #3. c) Conductor #4.

The temperature dependence of the copper resistivity ρ was measured on three samples taken from the copper profile used to manufacture the strands; the resistance was measured at 4.2 K, 77 K and 298 K (see Figure 2:15). The RRR is computed as Equation 2:4 and reported in Figure 2:15. The value of $\rho(273 \text{ K})$ is computed using a linear interpolation between the resistivity at 77 K and at 298 K.

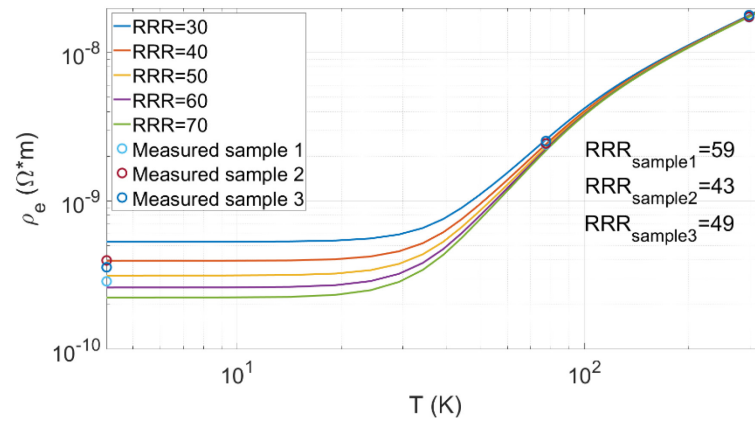


Figure 2:15. Electrical resistivity of copper as function of temperature for several RRR at zero magnetic field (lines, data from [58]). The values measured on the copper profile sample are indicated by open circles.

$$RRR = \frac{\rho(4.2 \text{ K})}{\rho(273 \text{ K})}$$

Equation 2:4- The RRR evaluation

The effect of the magneto resistance is disregarded (see Figure 2:16), as it is very small (<8%) at temperatures above 77 K for this copper with RRR=40. Such an effect leads to a negligible difference in the current flowing into the copper (~25 A), therefore on the temperature.

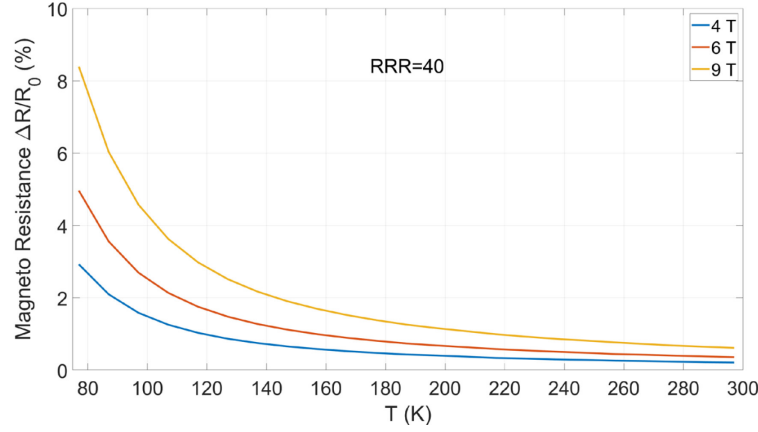


Figure 2:16. The magneto resistance as function of temperature for different magnetic fields (data from [58]). R_0 is the resistance at 0 T.

The solder used in the solder filled conductor is $\text{Bi}_{57}\text{Sn}_{42}\text{Ag}_1$; a resistivity value at 4.2 K and RT is found in literature for a solder with almost the same composition, $\text{Bi}_{58}\text{Sn}_{42}$ [53]. The temperature dependence of the electrical resistivity is modelled on the basis of that of $\text{In}_{66.3}\text{Bi}_{33.7}$ from [59], whose resistivity at 4.2 K and RT is close to the one of $\text{Bi}_{58}\text{Sn}_{42}$.

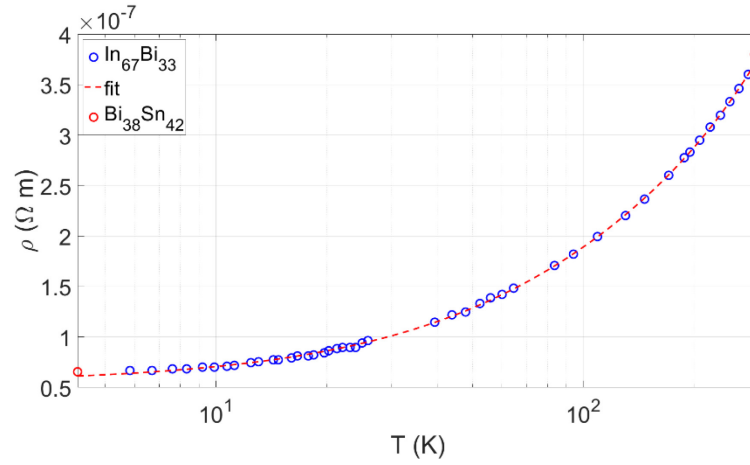


Figure 2:17 The resistivity used for the solder of the solder-filled conductor as function of temperature. The red dots represent the values found for the $\text{Bi}_{58}\text{Sn}_{42}$ in [53]. The blue dots are the data taken from [59].

The temperature of the cable is obtained solving a system of implicit equations (in temperature) for any section of the HFZ in which the voltage was measured, describing the current sharing between the copper, the stainless steel (SS) and other metals, if any, electrically in parallel. The equivalent parallel circuit of the different materials composing the conductor is illustrated in Figure 2:18, where R is the resistance per unit length and the temperature of the i^{th} material can be expressed as a function of the copper and jacket temperatures. The total current I_{tot} is kept constant, as in the experiment. The electric field is the same for any material, being the different paths in parallel. It is a function of the temperature of the materials, because of the equivalent resistance (Equation 2:5, Equation 2:6). At the beginning of the iterations, a value for T_{cable} is chosen. Since the cable temperature is derived from the voltage measured between the voltage taps, this value is an average over a certain length (usually 100 mm). For the sake of the calculation, the cable temperature is virtually located on a fictitious temperature sensor, placed in the middle of the voltage taps. The measured temperature on the external wall of the jacket is considered to represent that of the steel, assuming it uniform across the jacket radial direction. Since the positions of the jacket thermometers is not the same as of the fictitious cable temperature sensors, the temperature of the steel in the fictitious temperature sensor location is found from a linear interpolation. In the case of Conductor#4, there is also the solder as other branch of the parallel circuit. The hypothesis on its temperature is that it is the average between the steel and the cable in the fictitious temperature sensor location (Table 2:9).

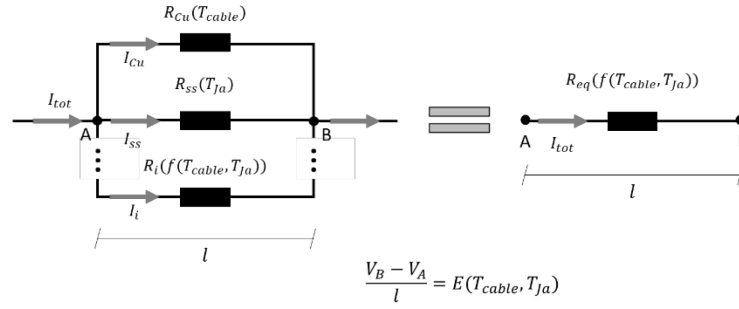


Figure 2:18. The sketch of the electrical circuit of the conductor. The nodes A and B are the voltage taps in the HFZ.

$$E(T_{cable}, T_{Ja}) = R_{eq}(T_{cable}, T_{Ja}) I_{tot}$$

Equation 2:5- The electric field of the equivalent electric system.

$$\frac{1}{R_{eq}(T_{cable}, T_{Ja})} = \sum_i^n \frac{1}{R_i(f(T_{cable}, T_{Ja}))}$$

Equation 2:6-The equivalent resistance per unit length of the circuit with i in parallel. For the specific problem all the T_i can be obtained as function of T_{cable}, T_{Ja} . The $f(T_{cable}, T_{Ja})$ are in Table 2:9.

Material	$f(T_{cable}, T_{Ja})$
Copper	$f(T_{cable}, T_{Ja}) = T_{cable}$
Steel	$f(T_{cable}, T_{Ja}) = T_{Ja}$
Bi ₅₇ Sn ₄₂ Ag ₁	$f(T_{cable}, T_{Ja}) = (T_{cable} + T_{Ja})/2$

Table 2:9 The $f(T_{cable}, T_{Ja})$ used in Equation 2:6 for different materials.

The system is solved iteratively until the relative error between the computed E and E_m (for the time instants of interest) is lower than a set tolerance. Here E_m is the measured electric field. At the end of the iterations, for that conductor length section, it is possible to obtain the current flowing in any i^{th} material, according to Equation 2:7.

$$I_i(T_{cable}, T_{Ja}) = \frac{E(T_{cable}, T_{Ja})}{R_i(f(T_{cable}, T_{Ja}))}$$

Equation 2:7- The current flowing in the i^{th} path.

The Figure 2:19 gives an example of the T_{cable}, T_{Ja} and T_{solder} estimation of the Conductor#4. It is possible to see that the copper carries most of the current, but the contribution of the steel and the solder is not negligible (around 10 % in the hot spot). In particular, where the temperature is higher, the copper carries less current, which goes into the other parallel paths according the resistance of each material (see Figure 2:20). The higher is the temperature in the cable, the closer becomes the resistance of the copper and the other materials, allowing them to carry more current.

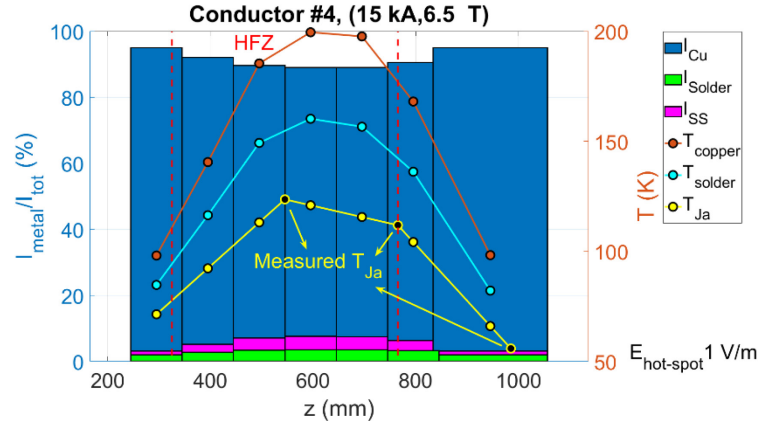


Figure 2:19. The cable temperature profile along the conductor length for the Conductor#4 at the instant at which the maximum electric field is ~ 1 V/m, with the slow heating triggering the quench at full current, at $B = 6.5$ T. The cable, jacket and solder temperatures are computed considering the current sharing between the copper, stainless steel and solder, whose redistribution is shown by histograms.

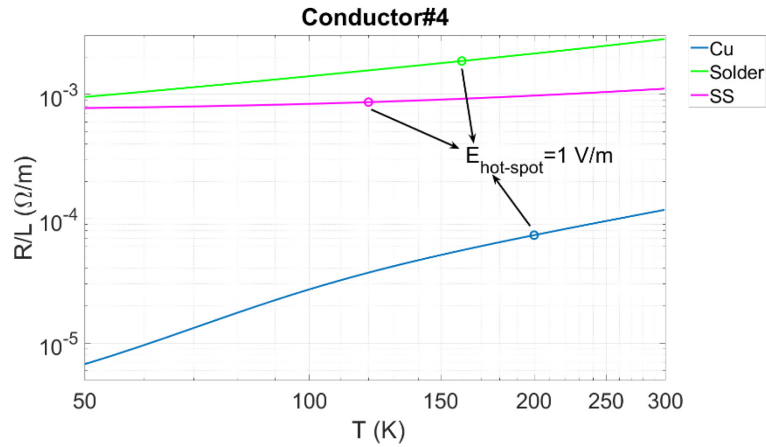


Figure 2:20. The resistance per unit length of the materials involved in the Conductor#4 cable temperature estimation.

2.5.2. Comparison between the different shots

By “shot”, it is meant one quench experiment performed on a certain conductor, characterized by certain parameters: the quench triggering mode, the mass flow rate, the current, the magnetic field.

As stated in the paragraph 2.3 , the quench was triggered by heating up the helium flowing in the conductor by heaters placed on the conductor inlet pipe. Two different heating rates were used: 1) a rapid one (heat pulse, hp), heater power of about 80 W for tens of seconds; 2) a slow one (slow heating, sh). Where the power was increased parabolically in hundreds of seconds till the conductor quenched. Figure 2:21 shows the two heating modes to quench the Conductor#4.

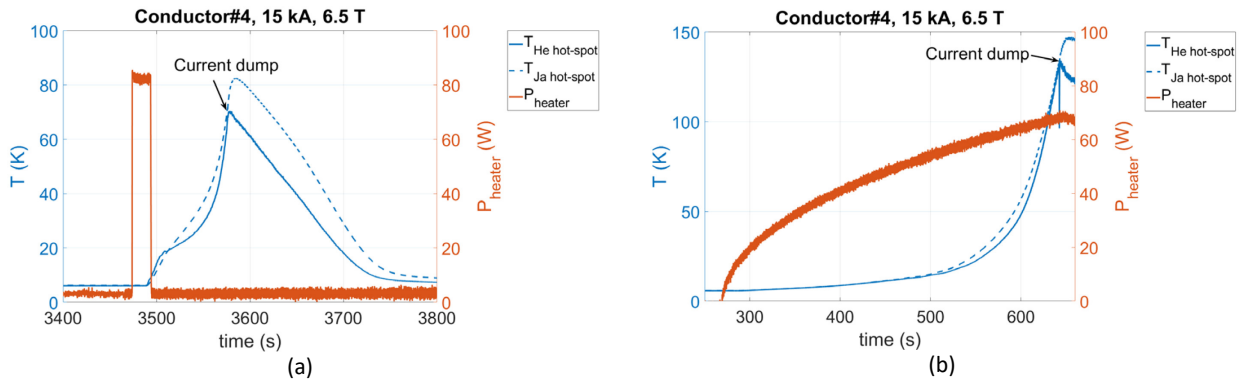


Figure 2:21 The quench triggered in two ways on the Conductor#4: a) the heat pulse ; b) the slow heating.

In the Table 2:10-Table 2:12, the list of the shots analysed for each conductor, with the different parameters (field, current, heating mode and H mass flow rate). The Conductor#1, required more energy to quench, because of the lower n value. All the conductors start from the same initial conditions, with an electric field of about $0.7 \mu\text{V/cm}$ (see section 2.4.3) and I_c 1-3% higher than the operating current I_{op} (see Figure 2:14).

Shot# Conductor#1	B (T)	I (kA)	Heating mode and corresponding quench energy	\dot{m} (g/s)
161101	3.5	15	Heat pulse, 80 Wx65s-> 5.2kJ	1.5
161103	3.5	15	Slow heating -> 31 kJ	1.5
161105	3.5	15	Slow heating -> 78 kJ	3
181101	9	9.5	Slow heating -> 36 kJ	1.5

Table 2:10 The list of the shots analysed for the Conductor#1 with their specifications.

Shot# Conductor#3	B (T)	I (kA)	Heating mode and corresponding quench energy	\dot{m} (g/s)
170808	6	15	Heat pulse, 80 Wx15s->1.2 kJ	1.5
190808	6	15	Slow heating -> 6 kJ	1.5
180801	6	15	Heat pulse	3
200802	10	11	Slow heating -> 13.5 kJ	1.5

Table 2:11 The list of the shots analysed for the Conductor#3 with their specifications.

Shot# Conductor#4	B (T)	I (kA)	Heating mode and corresponding quench energy	\dot{m} (g/s)
140809	6.5	15	Heat pulse, 80 Wx20s->1.6 kJ	1.5
190807	6.5	15	Slow heating -> 10 kJ	1.5
170801	6.5	15	Heat pulse	3
200801	10.8	11	Slow heating -> 14 kJ	1.5

Table 2:12 The list of the shots analysed for the Conductor#4 with their specifications.

Looking at the hot spot evolution in Figure 2:22, it is possible to see that evolution of the E and the T_{cable} is very similar for all the 15 kA shots, since it is possible to consider the hot spot as adiabatic [16]. Consequently, it is not influenced by the neighbour points around it.

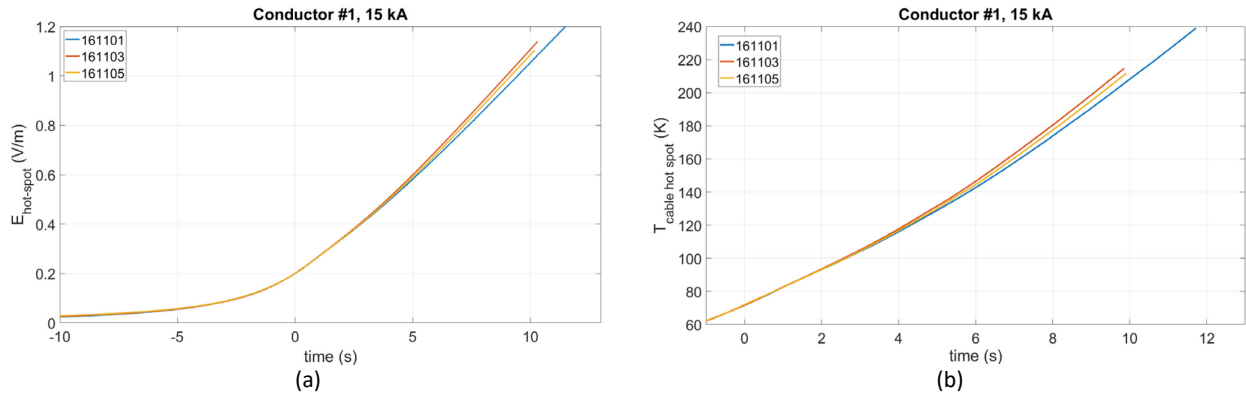


Figure 2:22 a) The $E_{hot-spot}$ evolution for the shots at 15 kA in the Conductor#1. b) The $T_{cable hot-spot}$ evolution for the shots at 15 kA in the Conductor#1.

The situation is different when plotting the total voltage versus time and versus the T_{cable} in the hot spot on the Conductor#1, see Figure 2:23. The synchronization in time is done at 0.2 V/m . The temperature evolution is influenced more by the heating mode than by the mass flow rate. In fact, the shots 161103 and 161105 (both slow heating) almost overlap, despite the difference in mass flow rate (1.5 and 3 g/s). The curve for the heat pulse (in blue, 16101) is moderately different from the one for slow heating (red and orange). The different behaviour between slow heating and heat pulse is due to the different He temperature profile along the conductor at the time of quench initiation (see Figure 2:24). In case of heat pulse, the quench is initiated in the weakest point of the conductor (identified in 2.4.4). In the slow heating case, the downstream border of the HFZ is heated more than the rest of the conductor, and there the quench starts. The slow heating is much slower process than the heat pulse. So, the helium has the time to bring the heat generated in the HFZ during the current sharing and bring it by advection downstream. The corresponding electric field profiles are shown in Figure 2:25, where it is possible to see that the shape of the electric field remains unchanged in time.

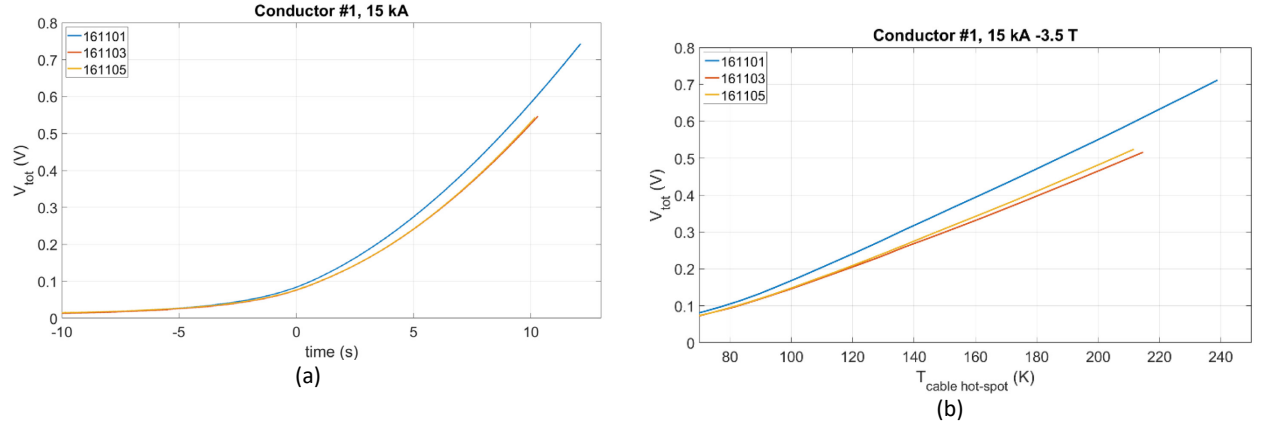


Figure 2:23 a) The total voltage evolution for the shots at 15 kA in the Conductor#1. b) The total voltage vs the $T_{cable\ hot\ spot}$ for the shots at 15 kA in the Conductor#1.

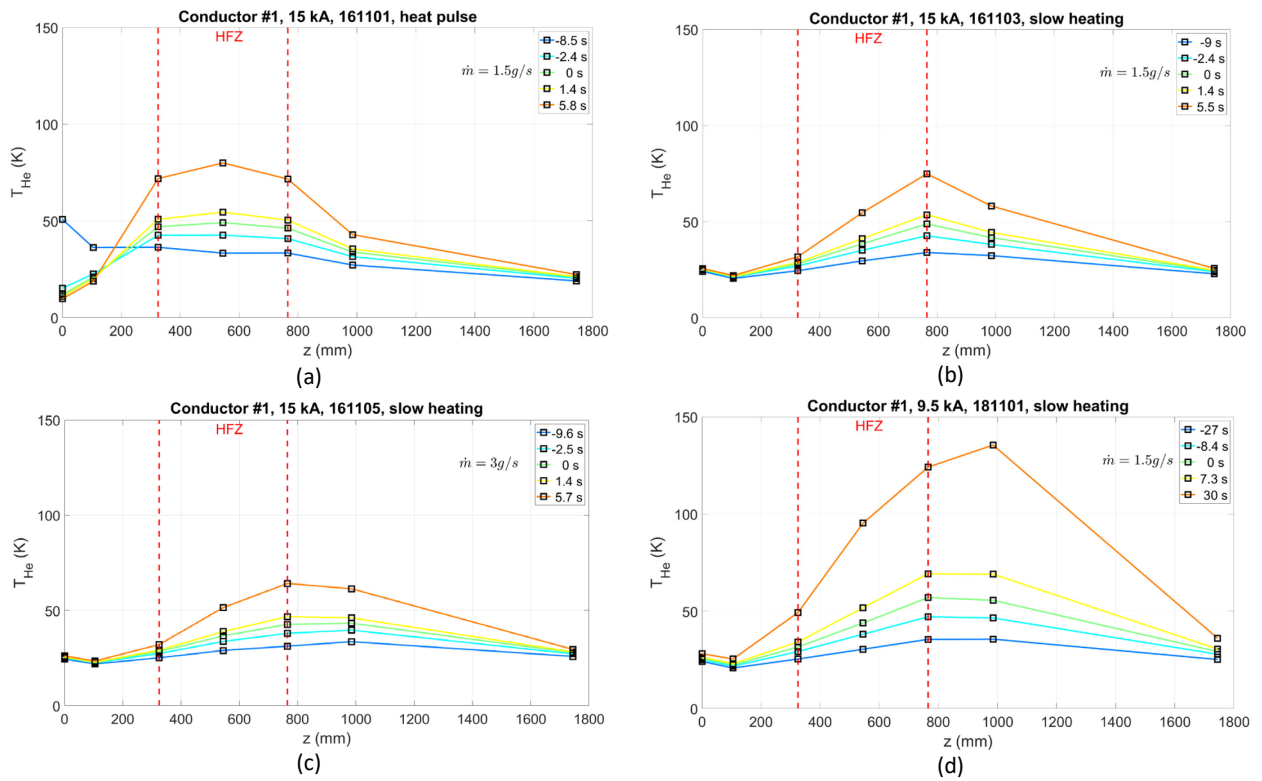


Figure 2:24 The He temperature profiles of the Conductor#1 in the shot analysed for several times (at which the $E_{hot\ spot}$ is: 0.03, 0.1, 0.2, 0.3 and 0.65 V/m). (a) shot #161101; (b) shot #161103; (c) shot #161105; (d) shot #181101. The lines are interpolation between the temperature sensors location. The 0 is at the inlet of the helium in the conductor.

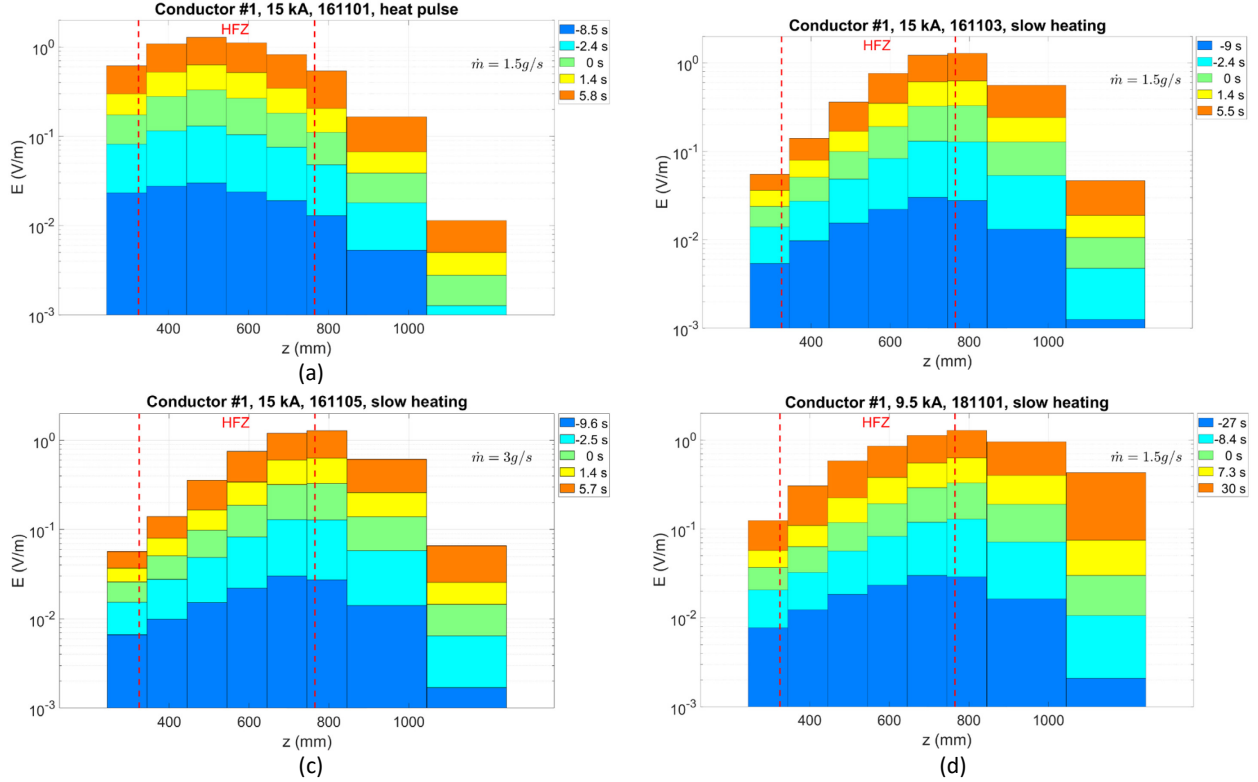


Figure 2:25 The E profiles of the Conductor#1 at different shots analyzed for several times (at which the $E_{hot\ spot}$ is: 0.03, 0.1, 0.2, 0.3 and 0.65 V/m). (a) shot #161101; (b) shot #161103; (c) shot #161105; (d) shot #181101. The width of the bar represents the length between the voltage taps. The 0 is at the inlet of the helium in the conductor.

From Figure 2:25, one can notice that the quench propagates beyond the so-called High Field Zone (HFZ). This is because the temperature profile can compensate the intrinsic I_c profile of conductor and the SULTAN magnetic field profile. The HFZ in SULTAN is defined as the region where the magnetic field is homogeneous, that is the variation is less 4% with respect to the maximum value of the field (see Figure 2:26). Considering a uniform temperature along the length, it is possible to see in Figure 2:26 b) that the 4% homogeneity zone on the critical current for the QE REBCO conductor at 7 K-3.5 T is about 540 mm long (from 275 mm to 815 mm), about 100 mm longer than the HFZ. The length of this zone, at uniform temperature, is influenced more by the value of temperature than the value of the maximum magnetic field, but much less than in the case of Nb_3Sn (Figure 2:26 c), scaling law taken from [18], neglecting the strain dependence), where at 10 T the 4% homogeneity zone on the critical current is much shorter than for REBCO: from 200 mm to 300 mm, depending on the temperature. If a more stringent definition of homogenous I_c is used (for example 2%) the difference between REBCO and Nb_3Sn is even more pronounced. This explain the particular electric field profile in the case of slow heating.

However, in a fusion magnet, the conductor is exposed to a constant high field over several meters. An important question is if the quench propagation in the QE experiment (<1 m of uniform I_c region) is relevant for the case of a magnet (>20 m of uniform I_c region). This question is addressed in 2.7 with the help of the multi-physics model, where it is possible to see that the SULTAN magnetic field profile is able to restrict the normal zone with respect to the case of uniform magnetic field along the length, slowing down the voltage rise.

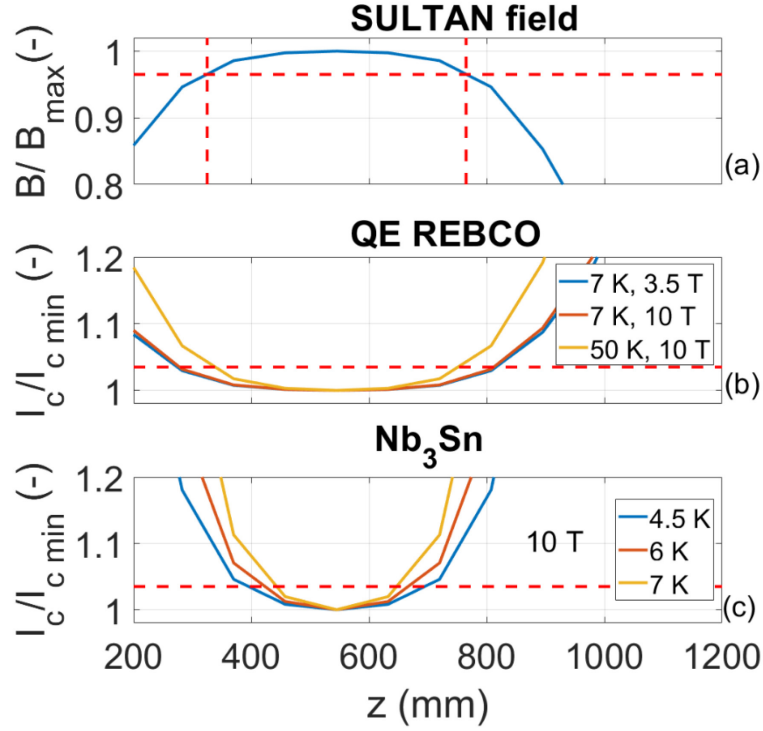


Figure 2:26 a) The normalized Sultan field profile. The vertical red dashed lines are at the intersection of the 4% homogeneity of the field; b) the normalized I_c of the Conductors of the QE 7 K-3.5 T and 50 K-6.5 T along the length of the conductor, computed taking into account the SULTAN magnetic field profile; c) the normalized I_c for the Nb_3Sn at 10T maximum field for several temperatures computed taking into account the SULTAN magnetic field profile. The 0 is at the inlet of the helium in the QE conductor. The horizontal dashed lines are at 4% difference with respect to the max of the magnetic field, (minimum of the I_c).

In Figure 2:27 the temperature of the different materials when the $E_{hot\ spot}$ is 0.65 V/m is shown for different shots in Conductor #1. It is possible to see that there is a large difference between the cable and helium temperature (about 70 K) and cable and jacket (about 100 K), as qualitatively predicted already by R. Kang [41]. Moreover, it is possible to see that the hot spot position is located where the I_c distribution has a minimum, computed taking into account the magnetic field and cable temperature at $t=0$ s. In the shot at low current (181101, 9.5 kA), the temperature is higher than in the other shots at 15 kA, because to have the same electric field at lower current, the resistivity, hence the temperature, have to be higher. The lower current scenario is also slower, see Figure 2:28. This smooths the temperature in the cross section (Figure 2:27 d)), because, for a given change in the voltage value, there is more time for the heat to be transferred from the cable to the helium and to the jacket than with the higher current.

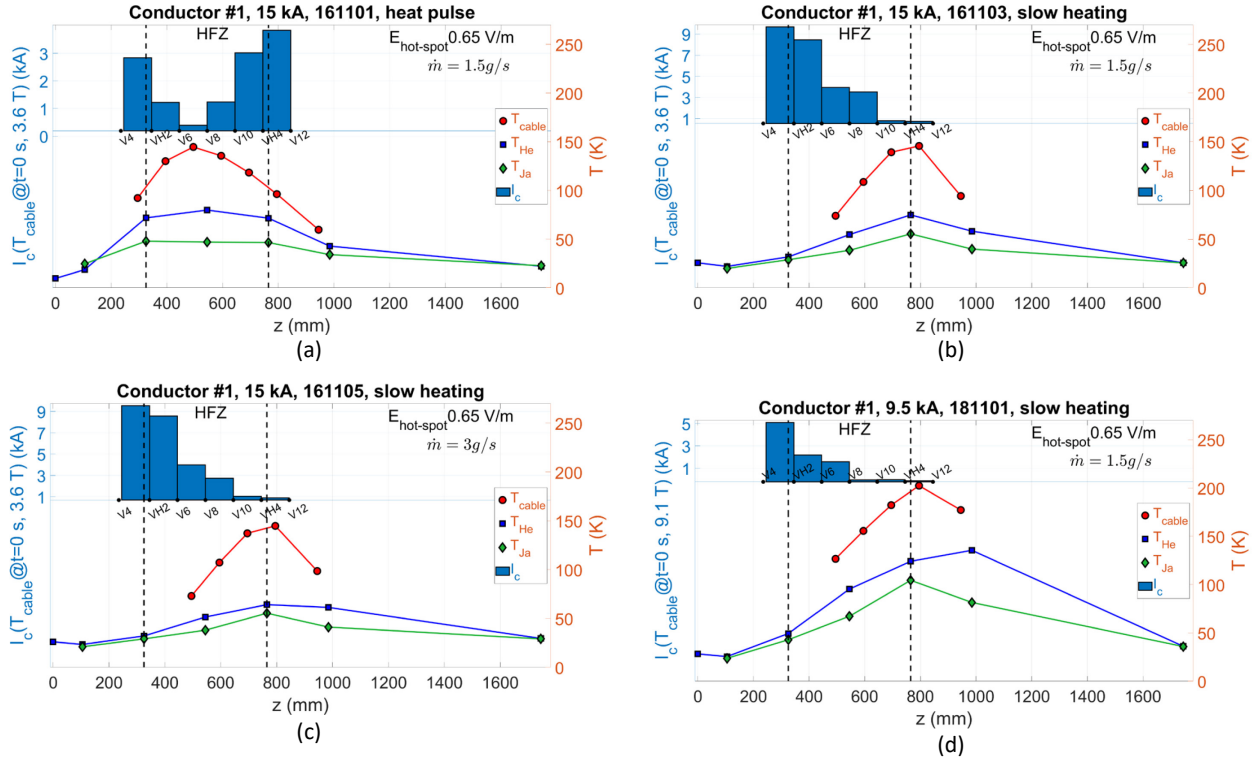


Figure 2:27 The temperature and I_c profiles in the Conductor #1 for different shots. The temperature of copper, He and jacket are depicted at the instant when the $E_{hot-spot}$ is 0.65 V/m. The I_c (blue bars) is shown at the when the $E_{hot-spot}$ is 0.2 V/m ($t=0$ s).

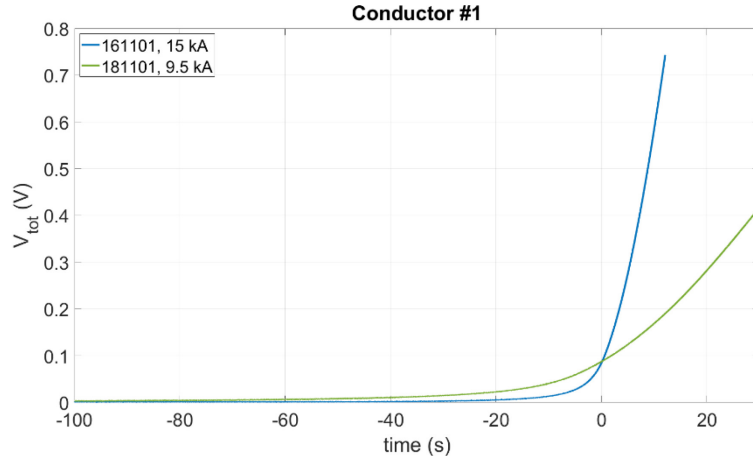


Figure 2:28 The total voltage evolution in the Conductor#1 for two shots at 15 and 9.5 kA.

Similar considerations can be done for the other two conductors.

Figure 2:29 shows the evolution of voltage and electric field in the hot spot for the three conductors, in the case of heat pulse scenario at 15 kA and mass flow rate 1.5 g/s. The behaviour of the Conductor#1 and #3 are similar (the Conductor#3 has a slightly faster evolution than the Conductor#1), while the Conductor#4 is the slowest. This effect is due to the better contact between cable and jacket enhanced by the solder filling, which makes available the jacket thermal capacity as heat sink for the heat generated by the quench. In fact, the jacket temperature is the highest among all the conductors (see Figure 2:30). Thanks to the better thermal contact between all the conductors component, their temperatures are closer. In addition, the total thermal capacity in the Conductor#4 is higher than the other two, due to the presence of the solder. This contributes to the slow down the quench evolution as well. More comments on the difference among the three conductors will be discussed in 2.6.2.2, on the basis of the physical interpretation obtained by the computational model.

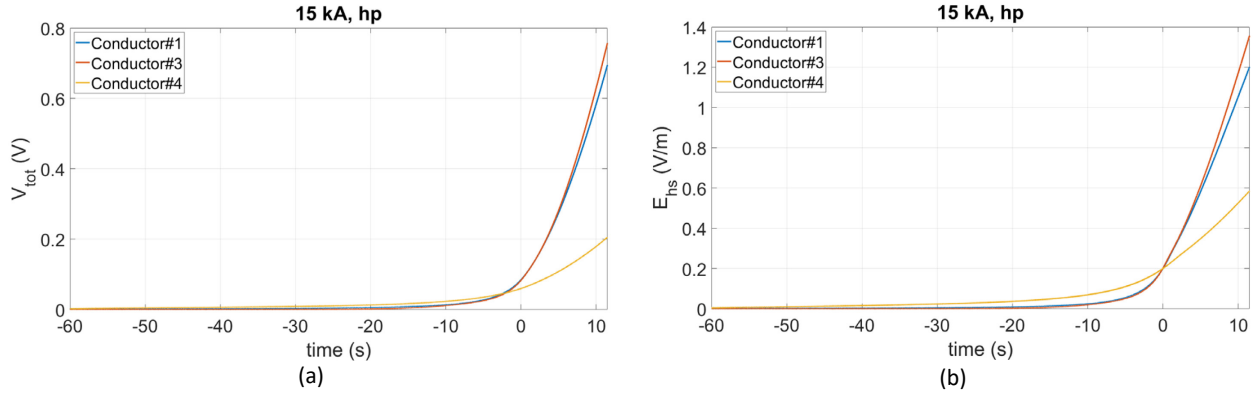


Figure 2:29 The total voltage (a) and the $E_{hot\ spot}$ (b) evolution for the three conductors at 15 kA operating current, with heat pulse heating mode and mass flow rate of 1.5 g/s. Namely the 161101 shot for the Conductor#1, 170808 for the Conductor#3, 140809 for the Conductor#4.

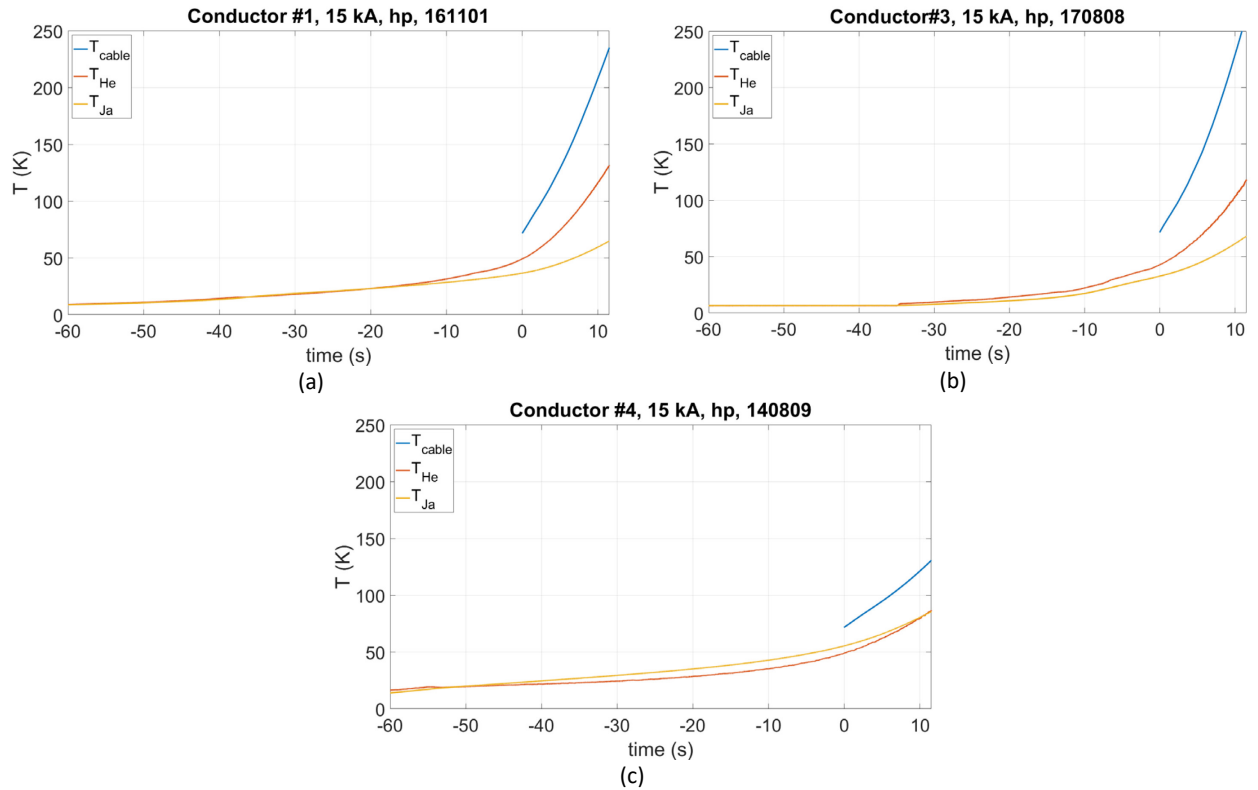


Figure 2:30 The temperature evolution in the hot spot for the Conductor#1 (a), Conductor#3 (b), Conductor#4 (c), at the 15 kA operating current, with heat pulse heating mode and mass flow rate of 1.5 g/s. The hot spot location is where the maximum E (and so T_{cable}) is measured. The T_{He} and T_{Ja} are the measured temperature by the closest thermometer.

2.5.3. Estimation of the Normal Zone Propagation Velocity

The quench is generally initiated locally and then expands longitudinally and transversally across adjacent turns in the case of a winding. The velocity at which the quench propagates is called Normal Zone Propagation Velocity (NZPV). Many experiments were done on the bare tapes to estimate the NZPV in the coated conductors (for example [60], [47]). NZPV for REBCO tapes in adiabatic conditions was found to be in the range 10–300 mm/s, depending on the current density, field and temperature, i.e. much slower than for Nb₃Sn (few m/s) and NbTi strands (over 10 m/s). In fusion cables, the large amount of copper, steel and helium, affects the NZPV, because of the different thermal capacity and dissipation than in strands.

Here, the value of the NZPV in the cable configuration for the three conductors is assessed, considering the NZPV as the speed at which the electric field profile moves along the conductor. The NZPV is evaluated as the length between the middle points in the two adjacent regions divided by the difference in time at which the electric field in those adjacent region reaches a certain threshold. The

definition of normal zone propagation velocity is ambiguous in HTS because of the extended current sharing regime. In fact, HTS and REBCO in particular can carry supercurrent up to very high temperature (70 K) and thus at high electric field. Therefore, there is not a sharp temperature transition as in the case of LTS. The temperature transition is the temperature at which the superconductor becomes normal. Its value affects the normal zone propagation velocity estimation, in particular its difference with respect to the operating temperature. The higher is this difference, the lower is the value of the NZPV ([16], page 487). Being the REBCO superconductor in “transition” in a broad range of temperature (and so in electric field), three thresholds on the electric field have been selected (0.03, 0.1 and 0.3 V/m) to evaluate the NZPV. At 0.03 and 0.1 V/m (when the T_{cable} is lower than 70 K) the superconductor is still carrying some current, while at 0.3 V/m its contribution is negligible. Figure 2:31 illustrates the evaluation of the NZPV in the case of the Conductor#4 in the shot 140809, in which the hot spot is located across the regions VH4-V10.

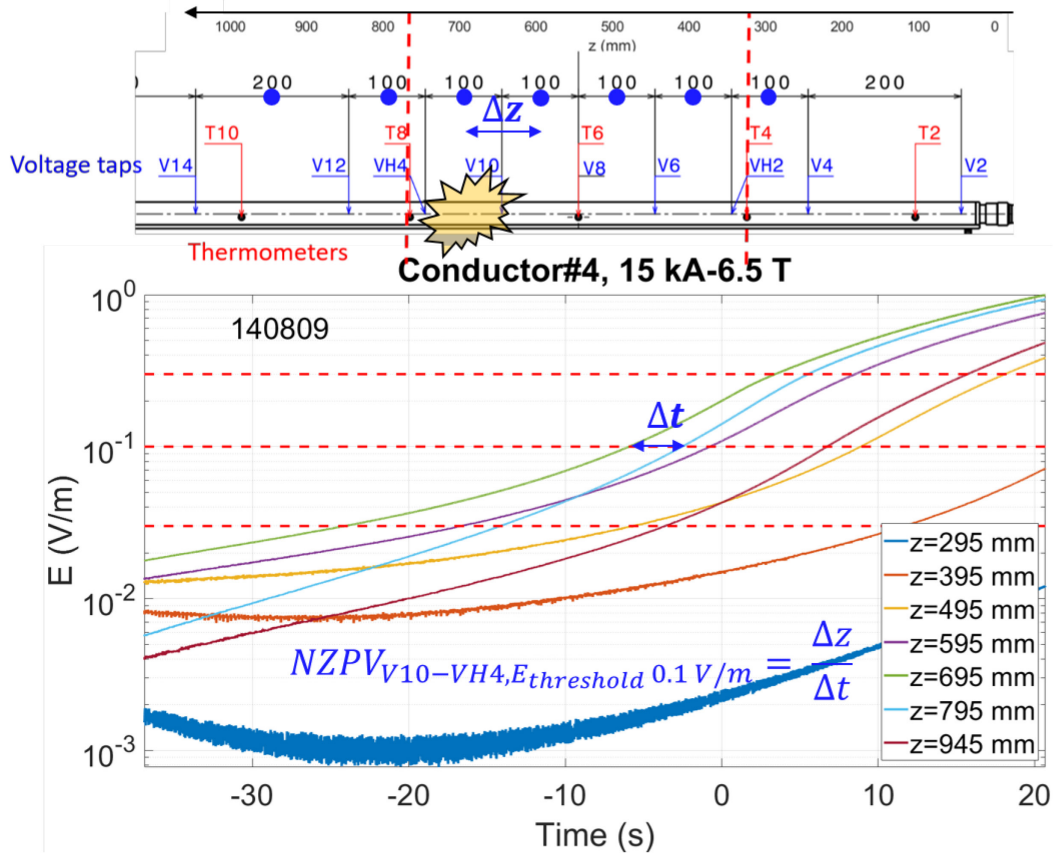


Figure 2:31 The evaluation of the normal zone propagation velocity in the case of the Conductor#4 for the shot 140809. In the legend in the bottom plot, the position of the middle point of the regions across which the voltage was measured. As an example, the evaluation of the NZPV in the region, VH4-V10, whose middle point is at 795 mm.

Figure 2:32 shows the NZPV along the length of the three conductors at 15 kA operating current. The estimated values are between 10 and 180 mm/s. The highest values are found close to the hot spot, above 100 mm/s. It is important to consider that the NZPV is obtained on 100 mm, the distance between the voltage taps. It means that the normal zone transition needs 0.6-10 s to travel along this length. In this time, the velocity can change significantly. Therefore, just the order of magnitude of the velocity has to be considered. As already stated in 2.5.2, in the heat pulse scenario, the hot spot is located at the minimum of the I_c profile assessed during the DC characterization. Among the three conductors, the Conductor#4 is the slowest one. In the slow heating scenario, all NZPV are fairly symmetrical with respect to the hot spot location (on the downstream border of the high field zone), meaning that there is not a preferred direction (downstream or upstream the helium flow) for the quench to propagate. This is the combined effect of the temperature and magnetic field profile. As illustrated in the section 2.7, without the restriction of the homogeneity zone of the magnetic field, the increase of the temperature downstream, due to the Helium advection, increases the NZPV, giving an asymmetric shape to the strand temperature with respect to the hot spot location.

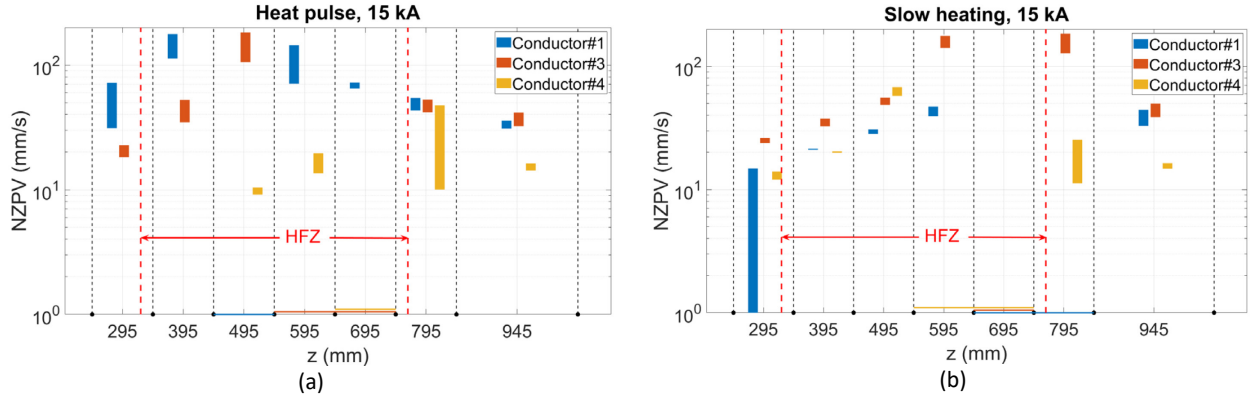


Figure 2:32 The NZPV for the three conductors along the length. In the bottom part of the plot, the coloured lines indicate the hot spot location for the conductor with the same colour. The two bases of the plotted rectangles indicate the maximum and minimum value of the NZPV evaluated for the considered region among the three electric field thresholds. The HFZ is highlighted. The NZPV was estimated in the case of 15 kA in the a) heat pulse scenario (161101 for the Conductor#1, 170808 for the Conductor#3, 140809 for the Conductor#4); b) the slow heating (161103 for the Conductor#1, 190807 for the Conductor#3, 190808 for the Conductor#4).

2.6. The comparison with the THEA code

One of the main goals of the Quench Experiment was to provide the data to validate computational codes. The interest in codes in the frame of the quench has several reasons. They are useful tools for the design of the cable, in order to verify the protection of a magnet after the quench detection. Using the codes, it is possible to explore the effect of several design parameters on the safety of the magnet. In this context, the most important physical quantity is the temperature of the hot spot. According to [16], the minimum safety criterion is to maintain the magnet hot spot temperature lower than 200 K, to keep the thermal strain low, keeping in mind that while the quench is developing in a small portion of the magnet, the rest of it remains at the operational temperature. For the hybrid EUROfusion magnet design, this is 4.75 K [61].

This section is devoted to the validation of the THEA code to model the quench in HTS conductor using the data of the Quench Experiment. THEA is a code developed for the Thermal, Hydraulic and Electric Analysis of superconducting cables [62] [63]. In THEA, the heat conduction equation describes the temperature in time and along the axis of the conductor for the thermal components. The thermal components can be made of several materials, used to homogenized the thermo-electric properties according to the cross section of the different materials. The transverse heat transfer between two components in thermal contact is modelled by a distributed transfer thermal resistance. The hydraulic components are described by the mass, momentum and energy conservation equations. The electrical model takes into account a cable formed of parallel electrically conductive components characterized by a non-linear longitudinal resistance, mutual and self-inductance. It is assumed that each component has a constant current density in its cross-section, and that current transfer happens along the length of the cable through distributed electrical conductances. The system of PDE describing the thermal, electric and hydraulic domains are coupled and numerically solved in space by Finite Element Method and in time by Finite Difference [63].

For the thermal and hydraulic analysis of superconductors, the main hypothesis is that the conductor length is much larger than its transverse dimension, so that all phenomena can be dealt with in a 1-D approximation of the cable along its length: this means that the physical quantities, such as the temperature, are assumed constant on the cross section (i.e. radial heat propagation is instantaneous). In LTS wire, the quench length grows to meters (1000 times more than the wire diameter) very quickly, making the 1D approximation reasonable. On the other hand, in a coated conductor tape, the normal zone propagates about one to two orders of magnitude slower. This may lead to a non-negligible radial gradient in the cross section of the soldered stack, as stressed by A. Zappatore in [42]. This hypothesis has been discussed by R. Kang in [64], stating that the detailed description of the temperature and current redistribution in a soldered stack could be unnecessary if the time scale of the experiment is much larger than the thermal and electrical time constants in the stack. The experiment time scale is a function of the inter-strand and strand-jacket thermal resistance, and depends upon the way in which the quench is started. In the case of the Quench Experiment, the time scale is very long: the temperature needs hundreds of seconds to rise from 7 K to 50 K. Moreover, the quench is triggered in the three strands simultaneously via the hot helium, making the inter-strand coupling negligible. The strand then could be treated as unique body.

The physical model, including the thermal and electrical characteristics is presented in 2.6.1. In 2.6.2, the validity of the 1D assumption for the jacket is discussed to account for the radial heat transfer in the jacket. Then, the temperature evolution of the three conductors (strand and jacket) is simulated to fit the experimental data, using the transverse thermal resistance between jacket and cable

as fitting parameter. The role of the thermal resistance between jacket and cable is discussed in terms of strand temperature rate of increase.

2.6.1. The model

The model has been first developed by R. Kang [41], and was modified to simulate the Quench Experiment. The initial model has four thermal domains: three strands (called s1, s2, s3) and the steel jacket. The strand is composed of: the superconducting ceramic, the copper (both coming from the copper shells and from the tapes), the Hastelloy (used in the tape as substrate), the silver (surrounding the ceramic coated substrate), the solder used to manufacture the strands. The cross sections of the strands are listed in Table 2:13.

Cross section in the thermal component	SC	Silver	Hastelloy	Copper	Sn ₆₀ Pb ₄₀	AISI 304 Stainless Steel	Bi ₅₇ Sn ₄₂ Ag ₁
Strand [m ²]	7.5e-8	2.25e-7	3.75e-6	50e-6	2.52e-6		
Jacket Conductor#1 						715e-6	
Jacket Conductor#4						652e-6	
Solder to fill Conductor#4							135e-6

Table 2:13. Cross section of the thermal domains composing the conductors.

The superconductor critical current is described by the scaling law $I_c(B, T)$, obtained from the DC characterization (see Chapter 3.5) and the n-value and by the threshold for the power law equation, E_0 , here $1e-4$ V/m, that describes the electric field upon the current in the superconductor. During the DC characterization, the n-value of the cable has been obtained. However, for the model, the n-value of the strand is needed. In practice, the n-value obtained during the measurements of the strand at 77 K, s.f. has been used, after having it scaled to low temperature and high magnetic field. The factor used for this it is the same as observed on the tapes.

	n of strands at 4.2 K, rescaled from 77 K measurements	n measured on the cable during the DC characterization @ 7 K
Conductor#1	26	6
Conductor#3	33	15
Conductor#4	39	13

Table 2:14 The n of strands at 4.2 K for the several conductors and for the cable at 7 K.

Thanks to the Ginzburg–Landau law [41], the different orientation of the tape along the conductor length with respect to the magnetic field, coming from the twist pitch of the strand and cable, is taken into account (see Figure 2:33). The stack in the three strands is oriented in three different directions with respect to the magnetic field in SULTAN. In the strand s1 the angle between the ab plane of the tape and the field is 90°. The stack in the strand s2 is rotated of 120° with respect to the strands s1, while the strand s3 of 240°. This has been set for the reference and solder-filled conductor. For the not-twisted conductor the value of the twist pitch has been set to 0 m, and for the angle to 0°.

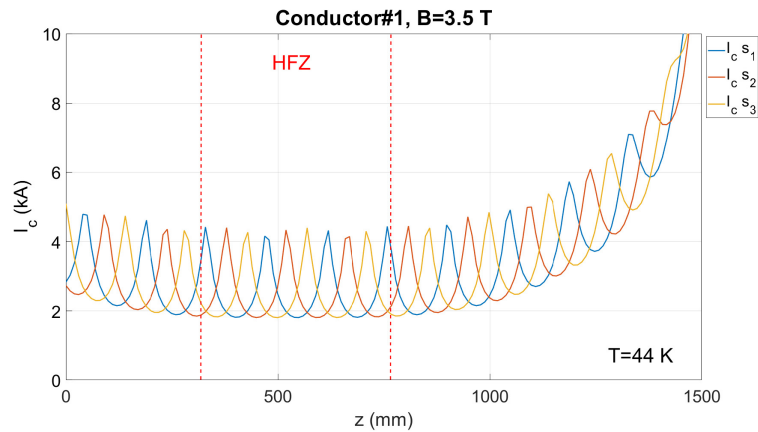


Figure 2:33. The I_c distribution along the length for the three strands of the Conductor#1 at 3.5 T at an average temperature of 44 K.

The material of the solder-filled conductor ($\text{Bi}_{57}\text{Sn}_{42}\text{Ag}_1$) is not present in the THEA library [58]. The thermo-physical properties have been added (Figure 2:34). The electrical resistivity is the one depicted in 2.5.1, Figure 2:17. For the thermal conductivity, the same reasoning of the resistivity has been adopted, while for the specific heat, the Neumann-Kapps rule has been applied, which weights the c_p on the mass fraction of different elements in the metal alloy.

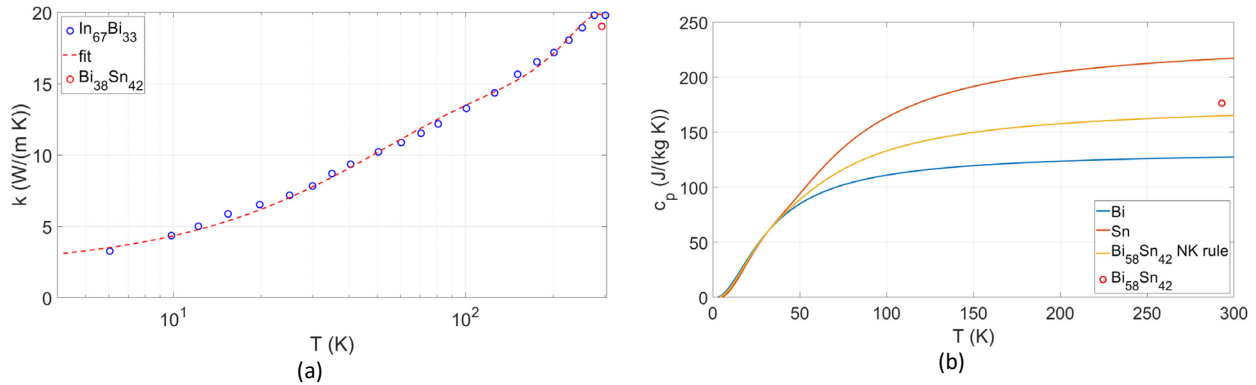


Figure 2:34. Thermo-physical properties used for the solder of the solder-filled conductor as function of temperature. The red dots represent the values found for the $\text{Bi}_{58}\text{Sn}_{42}$ in [59]. a) The thermal conductivity; b) the specific heat.

The transverse thermal resistance between the different strands has been set initially at $0.9 \text{ K}\cdot\text{m}/\text{W}$, as in [41]. It has been found a posteriori, that the thermal (as well as electrical) resistance is not an important parameter because the three strands behave in the same way, both in temperature and voltage (see 2.6.2). Instead, the thermal resistance between strand and jacket has been adjusted for any conductor in order to fit the experimental data, taking into account the rate of increase of the strand temperature in the hot spot. The conductor #1, and 3 have similar the thermal resistance between strand and jacket (respectively 0.12 and $0.21 \text{ Km}/\text{W}$), while the one for the conductor #4 is one order of magnitude smaller: $0.03 \text{ Km}/\text{W}$.

The initial temperature of the test was around 7 K ; at this temperature, the electric field across the high field zone is measurable but very small (less than mV/cm), leading to negligible self-heating. The simulation of the temperature evolution starts from a relatively high initial temperature ($\sim 30 \text{ K}$ on the helium/jacket, around 45 K on the cable, depending on the transverse thermal resistance). It is above 45 K on the cable that total voltage assumes relevant and interesting values for the quench detection, above 10 mV (see Figure 2:35). As a consequence it is possible to have a detailed description of the quench evolution at the detection threshold (100 mV for ITER) and above by starting the simulation from 45 K on the cable. Moreover, it is in that range of temperature that the rising speed of the temperature in the hot spot is high enough to be problematic from the safety point of view.

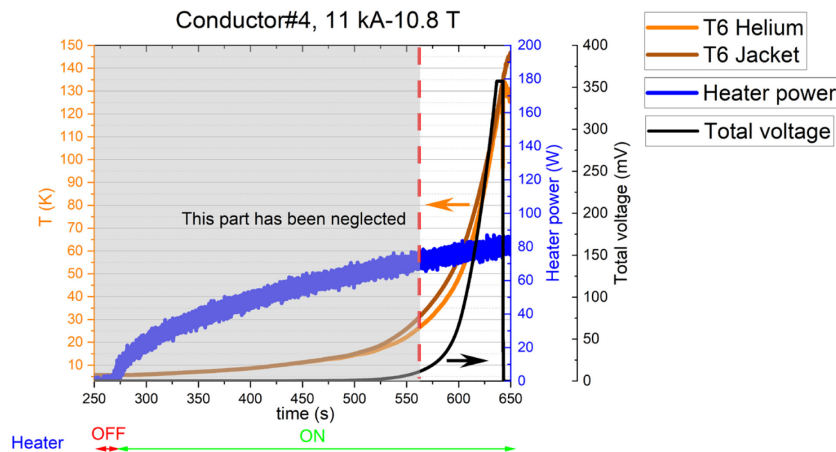


Figure 2:35. The temperature evolution (on the left axis) recorded by the sensors in the HFZ in the Conductor #4, in a slow heating shot, a high B and low I . On the right axis, the evolution of the heater used to trigger the quench (in blue) and the total voltage (in black).

Adiabatic boundary conditions have been set for all the thermal components: the heat flux is set to zero at the edges of the spatial domain. The length of the conductor is 2.67 m , which is the length of the real conductor without the terminations. The current is kept constant for the whole simulation. The simulation stops at the moment of discharge. The magnetic field profile is the Sultan one (see Figure 3:3).

About the numerical settings, the mesh is uniform (element size $1e-2$ m), and the time discretization is adaptive. From the electrical point of view, the transverse electrical conductivity between all possible couples (strand1-strand2, strand1-jacket, etc...) is $5e5$ S/m [31] and the mutual and self-inductance have been taken from [41].

In this paragraph, the effect of Helium is considered. The same mass flow rate of the experiment in the Conductor#1, in the heat pulse scenario, has been imposed by setting a fixed Δp between the ends of the conductor (around 40 Pa). The temperature at the boundaries has been fixed equal to the initial temperature. The heat transfer coefficient has been modelled by the Dittus-Boelter correlation [65] and the friction factor by the Blasius one [66]. In Figure 2:36 the temperature of the strand and jacket are shown in the case with and without Helium (dry). The synchronization between the two simulations is done on strand temperature at 70 K, as for the following plots. From Figure 2:36 it is possible to see that the influence of the coolant is negligible in the range of temperature considered (higher than 30 K), while it is important for the initial phase of the quench because it helps in developing the normal zone, influencing the voltage drift (see section 2.7). Moreover, the presence of He does not influence the dependence of the total voltage on the temperature in the hot spot. Above 30 K, the He has no significant cooling power due the much lower c_p than the other materials (Figure 2:37). Thus, for the following discussion, the helium does not need to be considered, since the focus is on the high dissipative range of the quench evolution and so, at high temperatures.

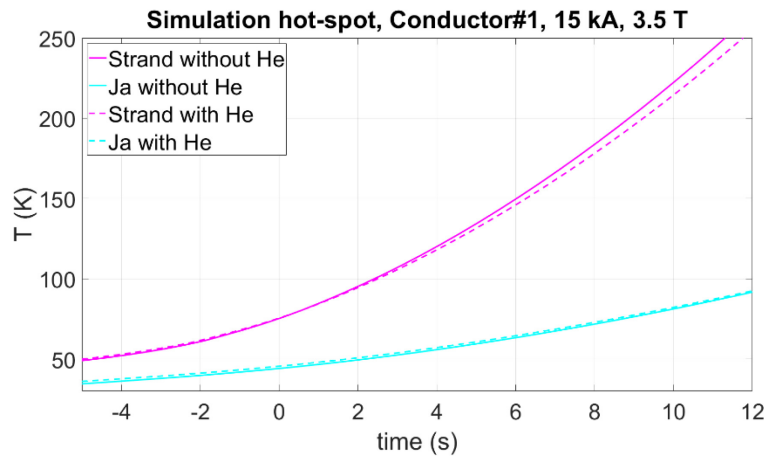


Figure 2:36 The simulated temperature evolution of the strand and the jacket in the hot spot of the Conductor #1, with and without the He.

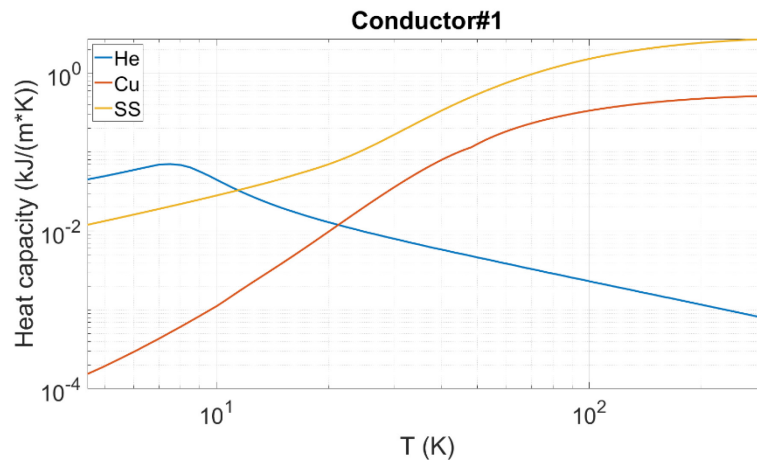


Figure 2:37. The heat capacity of the different materials of which the Conductor#1 is made of as function of temperature.

Regarding the effect of RRR on the hot spot, a parametric study has been carried, since, in paragraph 2.5.1, it has been seen that the value of RRR of the copper used for the strands varies from 40 to 60. Figure 2:38 a) and b) show that the effect of the change of RRR in the considered range is minor, both looking at the $T_{hot\ spot}$ evolution and on the $V_{tot} - T_{hot\ spot}$ characteristic. From now on, the RRR is set at 40.

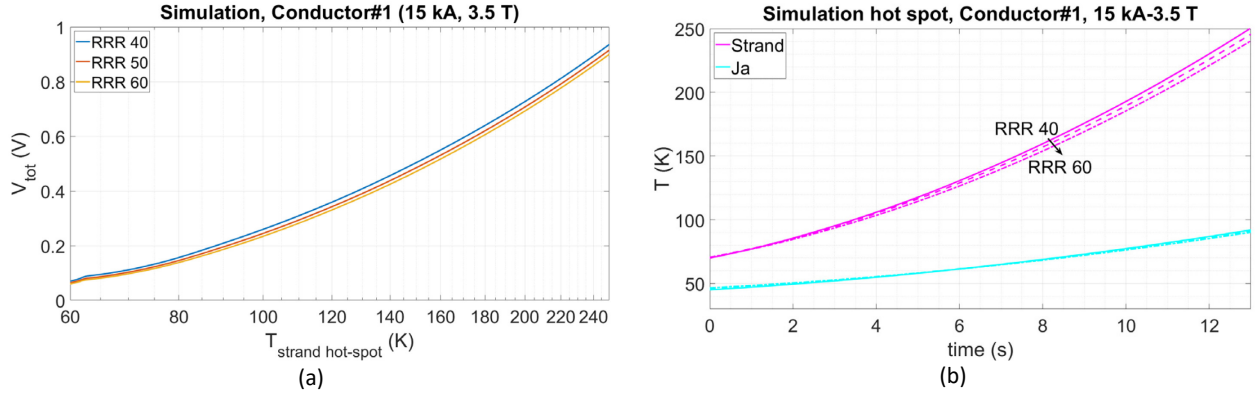


Figure 2:38. The parametric study on the copper RRR of the simulated results of the quench development of the Conductor #1. a) The total voltage on the conductor vs the hot spot temperature. b) The temperature evolution of the strand and the jacket in the hot spot.

2.6.2. The results

First of all, in the 70-200 K temperature range, the hot spots in the three strands have the same temperature evolution because:

- The current in the superconductor is negligible, and consequently the initial difference in temperature among the three strands (see Figure 2:33) that was caused by the different angular dependence of the critical current, does vanishes;
- In the experiment the quench was triggered by sending hot helium in the conductor, leading to a uniform heating in the cable.

For this reasons, the following considerations are valid for all three strands.

The total voltage on the conductor is a function of the electric field profile (see Figure 2:39 a)): the narrower is the electric field profile, the lower the total voltage. One possible cause of the disagreement between experimental and simulated electric field profiles is that the conductor shows an I_c distribution (possibly coming from the tape I_c not perfect homogeneity along the length), which was not introduced in the model. Moreover, the temperature gradient along the length at the initial conditions, around $T_{strand \text{ hot spot}}$ around 40 K, was not included. Because of the different broadening of the electric field, the total voltage in the experiment is lower than the simulated one (see Figure 2:39 b)). The simulated $V_{tot}(T)$ is almost independent from the transverse thermal resistance between strand and jacket. An important consideration needs to be done: if the model is not able to simulate the experimental total voltage, cannot be used as predictive tool for magnet protection. However, the SULTAN experiment itself cannot be used in this sense, due to the confined zone of the magnetic field along the length, not present in a large magnet, like a CS (see section 2.7, where it is shown that the normal zone expands much more in the uniform field scenario).

To compare the simulation with the experimental results, only the hot spot evolution is taken into account. In this way, it is also possible to compare the experiment and the simulation based on just one shot, not considering the location of the hotspot location. As discussed in the 2.5.2, at a given J_{cu} , for the same conductor, the hot spot evolution is independently on how the quench is triggered and on hot spot location, when the current in the superconductor becomes negligible. Moreover, the hot spot is the most critical point from the safety point of view.

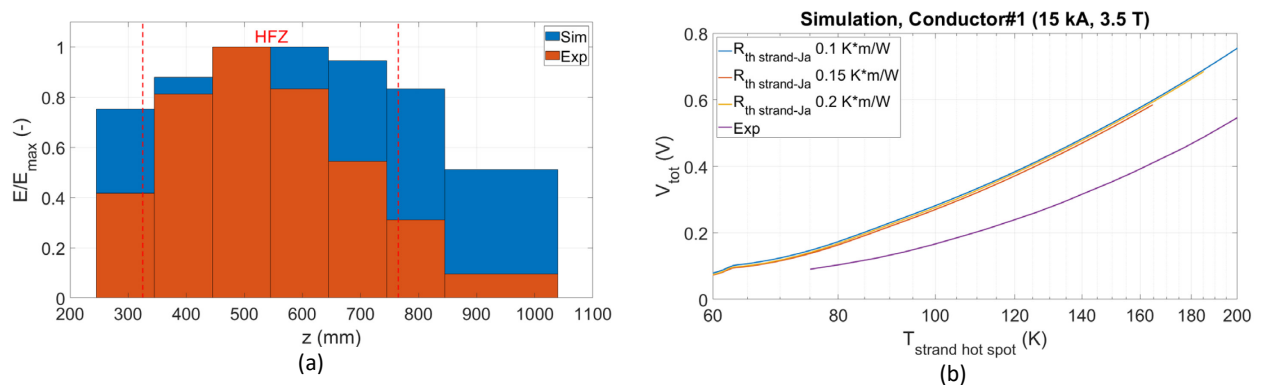


Figure 2:39. a) The normalized electric field profile in the HFZ, simulated vs experimental. b) The total voltage of three simulated cases with three different R_{th} between strand and jacket and the experimental one.

The copper temperature obtained from the voltage measurement in the HFZ (see paragraph 2.5.1) is compared the simulations. The voltage was measured across a region of 100 mm. Consequently, the copper temperature can be considered as the average temperature along 100 mm, and not exactly as the maximum one. However, this approximation is justified by the fact that the simulated temperature profile is very flat in the HFZ.

2.6.2.1. The radial heat diffusion: two shells model for the jacket

For the experiment, in order to maintain the steel/Cu cross section ratio designed in [35], the thickness of the jacket was 8.5 mm. This affects the thermal diffusion time τ_d in the jacket wall, i.e. the time that it is necessary to smooth the temperature gradient in the body ($\tau_d = \delta^2/\alpha$). δ is the characteristic length (in this case, the thickness of the jacket) and α is the diffusivity. If the thermal diffusion time is smaller than the time scale of the experiment, the assumption of uniform temperature in the cross section is valid. Figure 2:40 a) shows the dependence of τ_d of the stainless steel jacket with the dimensions of the Conductor#1 (and #3) with respect to the temperature, highlighting the range of temperatures that was considered in the simulation at 15 kA and 9.5 kA. In the case of 15 kA in the Conductor #1, the temperature in the jacket increases from 30 to 70 K in ~ 12 s (see Figure 2:40 b)), while τ_d in the same temperature interval, is between 5 and 13 s. Consequently, it is possible to state that the uniform temperature approximation is not valid in this condition. In fact, the simulated jacket temperature using just one body (one shell) is much higher than the experimental one (see Figure 2:40 b)), measured on the external wall of the steel tube. On the other hand, the simulated strand temperature is in very good agreement with the experimental values. This means that the temperature of the jacket cannot be lowered by increasing the thermal resistance between strand and jacket, without impacting on the temperature of the strands (see Figure 2:40 c)). The synchronization between simulation and experiment is done on the strand temperature. This holds for all the comparison. In the 9.5 kA scenario, the temperature of the strand and the jacket are in a good agreement with the experimental values. The experimental time scale is much longer than in the 15 kA scenario: it takes 35 s for the jacket temperature to rise from 50 to 100 K. This leaves more time for the heat coming from the cable to diffuse through the jacket: the diffusion time in the same range of temperature is between 10 and 17 s. Hence, the uniform temperature approximation is valid.

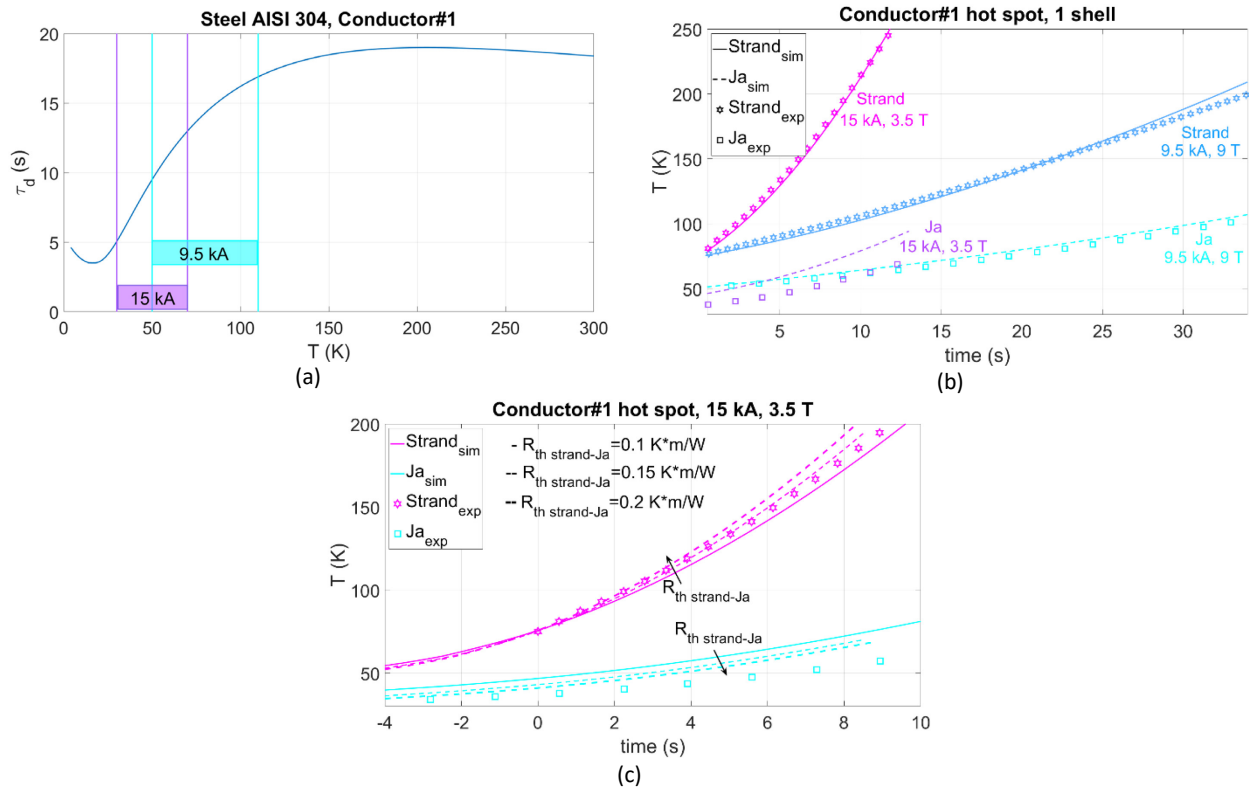


Figure 2:40 a) The diffusion time in the jacket of the Conductor#1 as function of temperature. The temperature ranges in the jacket used in the simulations with the 15 kA and 9.5 kA operating current are highlighted; b) The evolution of the strand and jacket temperature (simulated and experimental) for the Conductor#1 in 15 kA and 95 kA operating current shots; c) The simulated strand and jacket temperature evolution for different strand-jacket thermal resistances are compared to the experimental one.

In order to take into account the radial gradient, the jacket is divided into two shells (see Figure 2:41), in contact by the transverse thermal resistance $R_{th\ shell}$, sum of the radial transverse resistance inside each shell, computed in cylindrical coordinate (Equation

2:8), where k is the thermal conductivity, $D_{out I}$ is the outer diameter of the shell I, $D_{in I}$ is the inner diameter of the shell I. The same notation is used for the shell II. This procedure has been already adopted by K. Sedlak in [67].

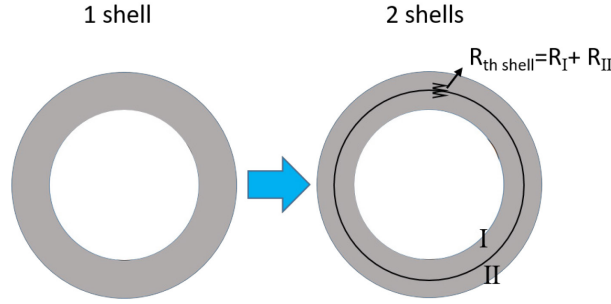


Figure 2:41 The division of the jacket into two shells, in order to model the radial thermal gradient in the thickness.

$$R_{th shell} = \frac{\ln\left(\frac{D_{out I}}{D_{in I}}\right)}{2\pi k} + \frac{\ln\left(\frac{D_{out II}}{D_{in II}}\right)}{2\pi k}$$

Equation 2:8- The transverse thermal resistance across the shells

In principle, $R_{th shell}$ is function of temperature, because of k . To simplify the model, the conductivity used in $R_{th shell}$ is the integral mean in the range of temperature observed in the experiment, denoted as \bar{k} . The initial temperature of the internal jacket shell is set at the helium one, taken from the experiment.

Figure 2:42 shows that the temperature in the external shell of the jacket is lower than the one modelled by a single shell, and closer to the experimental data. The comparison is done at the same total thermal $R_{th strand-Ja_{ext}}$. The difference between the internal and external shell temperatures at the current dump moment ($t=12$ s in the plot) is about 28 K. The simulated external jacket temperature is still higher than the experimental one, suggesting that a finer discretization of the jacket is needed in order to account for the real radial gradient. Moreover, the temperature of the strand is not significantly affected by the shell modelling of the jacket, meaning that what matters for the strand temperature is the total $R_{th strand-Ja_{ext}}$. Therefore, the model with two shells is adopted for all conductors.

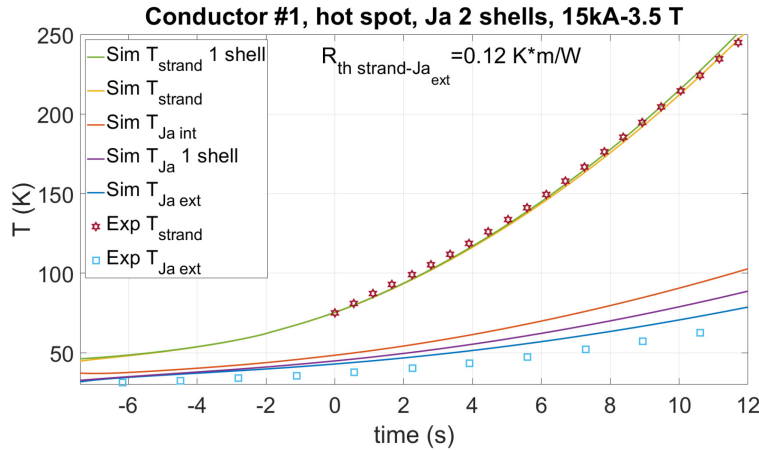


Figure 2:42 The temperature evolution of strand and jacket, simulated both with one or two shells. The two models have the same $R_{th strand-Ja_{ext}}=0.12 \text{ K}\cdot\text{m}/\text{W}$. The simulated results are compared with the experimental ones.

2.6.2.2. The Temperature evolution in all conductors

In order to find the thermal resistance between the strand and the internal shell of the jacket $R_{th strand-Ja_{int}}$ that fits the experimental strand temperature of the Conductor#1, a parametric study on two runs (15 and 9.5 kA) is carried out. The evolution of the strand temperature is much more influenced by the change of the thermal resistance than that of the jacket (Figure 2:43 a)) due to the difference in the heat capacity (see Figure 2:43 b)) between the cable (copper) and the stainless steel. Specifically, the strand temperature rises faster when the thermal resistance is higher, since the strand can exploit less the big heat capacity of the jacket as thermal sink. Therefore, there is also less current passing into the copper: the strand temperature is higher, the electrical resistance

of the copper increases, letting more current passing into the steel. However, this effect is marginal: from Figure 2:43 c), it is possible to see that the relative difference in current at the last instant before the current dump is about 0.5%. To summarize, the higher is $R_{th\ strand-Ja_{int}}$, the faster is the increase in the strand temperature, even if the joule heating in the copper is lower, proving the importance of heat capacity of the jacket.

The discrepancy between the simulation and the experiment in the strand temperature is quantified as the relative norm of the difference between the $T_{strand\ exp}$ and $T_{strand\ sim}$ with respect to the norm $T_{strand\ exp}$ (see Figure 2:43 d)). The selected value of $R_{th\ strand-Ja_{int}}$ is 0.1 K*m/K, which leads to a reasonably low error (between 2 and 3 %) on both the 9.5 kA and 15 kA runs.

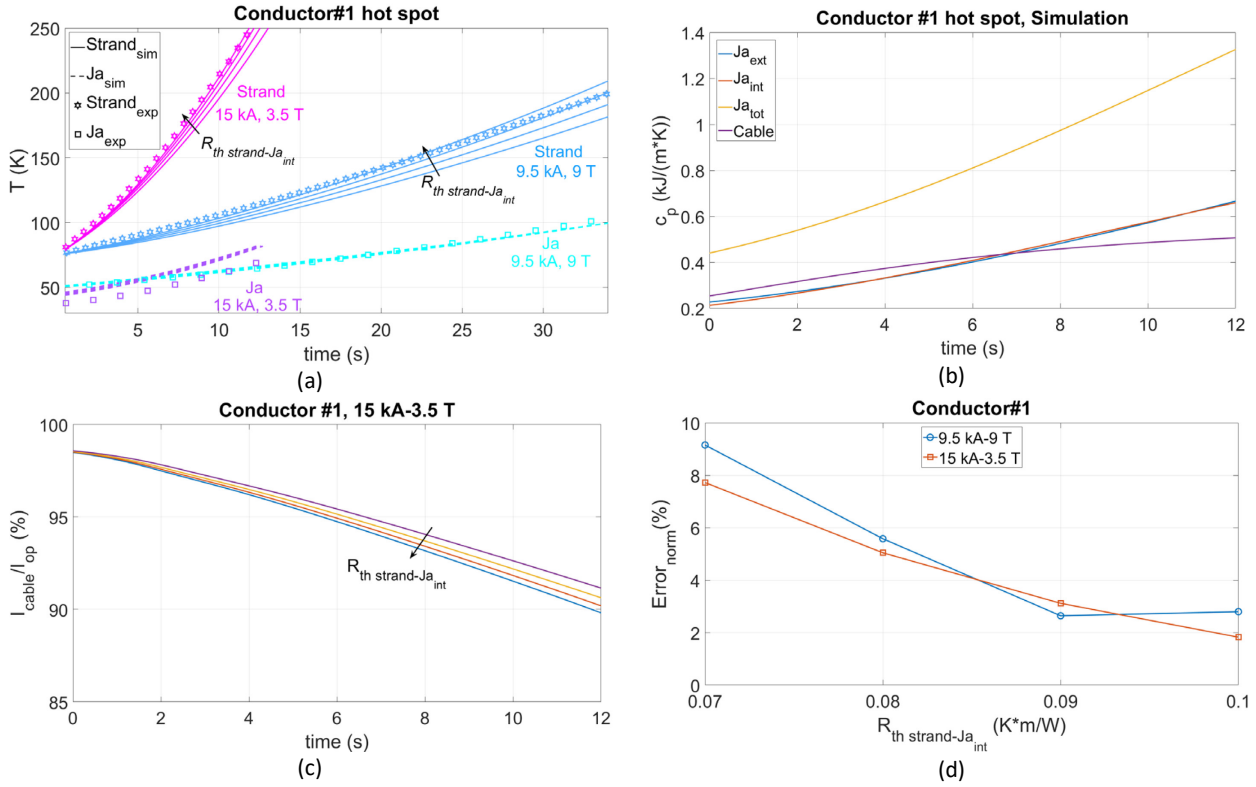


Figure 2:43 a) The evolution of the strand and jacket temperature in the hot spot of the Conductor#1 for both 15 and 9.5 kA. The simulated results (obtained for several $R_{th\ strand-Ja_{int}}$, whose values are reported in the frame d)) are compared with the experimental ones. b) The heat capacity per unit length for the different components of the Conductor#1 as function of time. c) The simulated relative current evolution in the Conductor#1 at 15 kA-3.5 T by varying the $R_{th\ strand-Ja_{int}}$. d) The error (computed as relative norm) between the simulated and experimental strand temperature as function of $R_{th\ strand-Ja_{int}}$, for both 15 kA and 9.5 kA shots.

From Figure 2:44 it is possible to see that the simulated electric field in the hot spot as upon the strand temperature is in very good agreement with the experimental one, both for the 15 kA and the 9.5 kA scenarios. At a given temperature, the electric field at 9.5 kA is lower, due to the lower operational current.

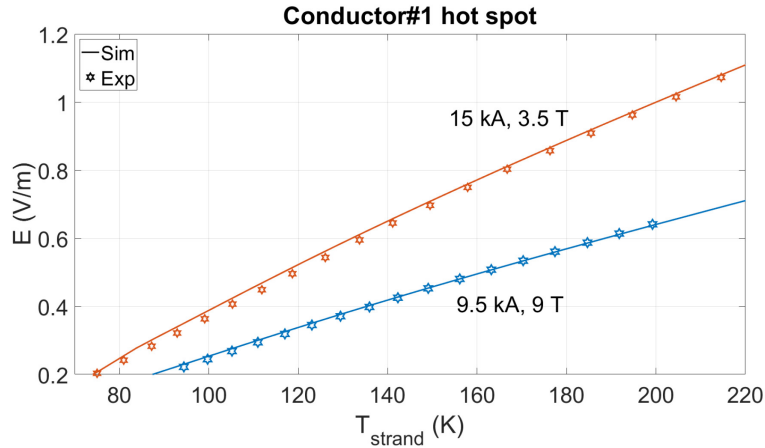


Figure 2:44 The electric field as function temperature (simulated and experimental) in the hot spot of the Conductor#1 for both 15 and 9.5 kA.

The same procedure for the research of the optimal $R_{th\ strand-Ja_{int}}$ is applied to the Conductor#3, obtaining a final value of 0.21 K*m/W, which gives an error of 2-3% on the strand temperature. From the Figure 2:45 it is possible to see that there is a very good agreement between the simulation and the experimental results, both on the temperature in the hot spot (strand and jacket) and on the electric field, for the 15 kA and 11 kA.

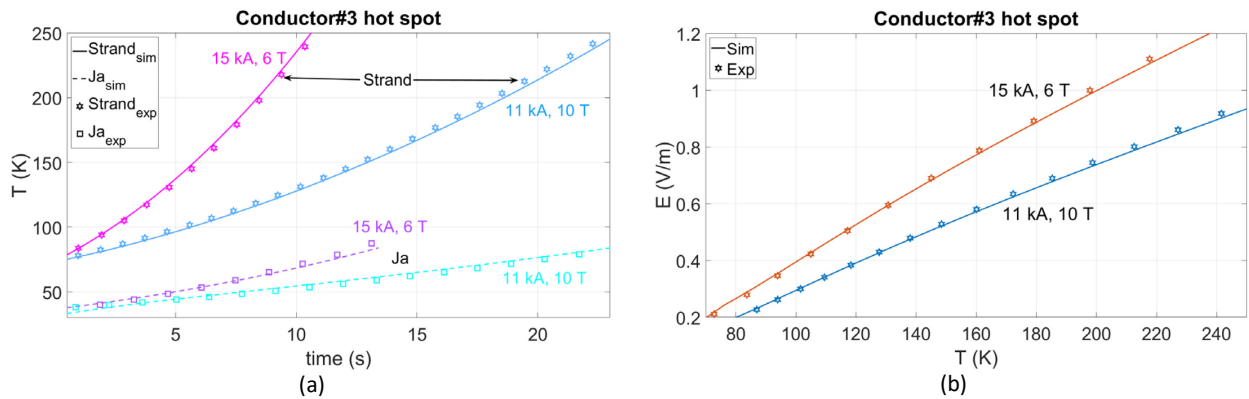


Figure 2:45 a) The temperature evolution in the hot spot of the conductor#3 at 15kA-6 T and 11kA-10T. b) The electric field vs strand temperature in the hot spot the conductor#3 at 15kA-6 T and 11kA-10T.

In the Conductor#4, also the solder has been modelled. Regarding the initial temperature set in the simulation, the temperature of the internal shell of the jacket is the average between the external shell of the jacket and the strand, while the temperature of the solder is the average between the strand temperature and the internal jacket shell. Looking at Figure 2:46, it is possible to see that the simulation and the experiment agree for $R_{th\ strand-Ja_{int}}$ 0.018 K*m/W (one order of magnitude less than in the Conductor#1 and #3), with an error of 1-2% on the strand temperature. The experimental jacket temperature was measured on the cable side and not on the helium channel one. This leads to a fair comparison between simulation and experiment. The same value of thermal resistance is set for the solder-strand and solder- Ja_{int} coupling. The presence of the solder induces a slower evolution of the quench, because it improves the thermal contact cable-jacket and it increases the total heat capacity of the conductor itself. This

leads also to a more homogeneous distribution of temperature in the cross section of the Conductor#4 (see Figure 2:47) with respect the other two conductors. However, it is interesting to notice that even if the solder has an important role, the current carried by the solder is only few percent of the operating current.

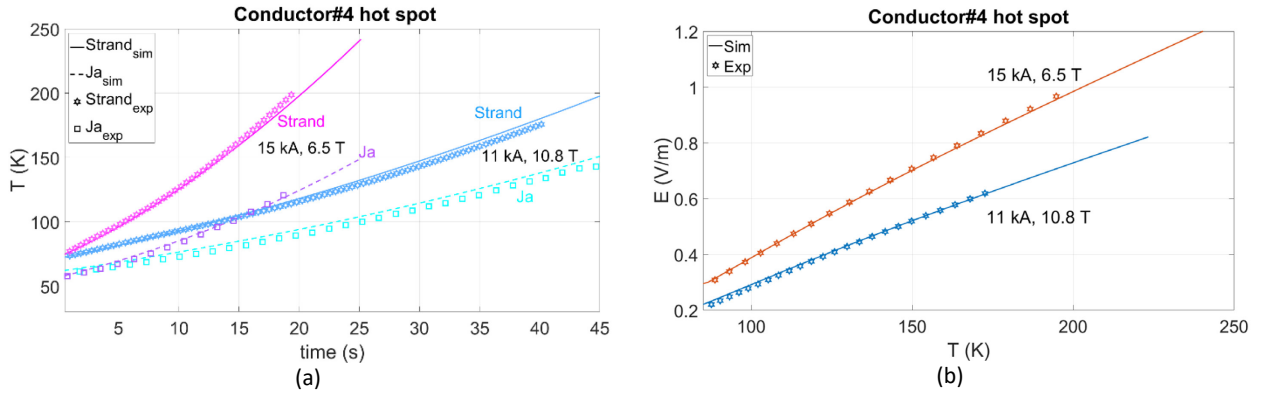


Figure 2:46 a) The temperature evolution in the hot spot of the conductor#4 at 15kA-6.5 T and 11kA-10.8T. b) The electric field vs strand temperature in the hot spot the conductor#4 at 15kA-6.5 T and 11kA-10.8T

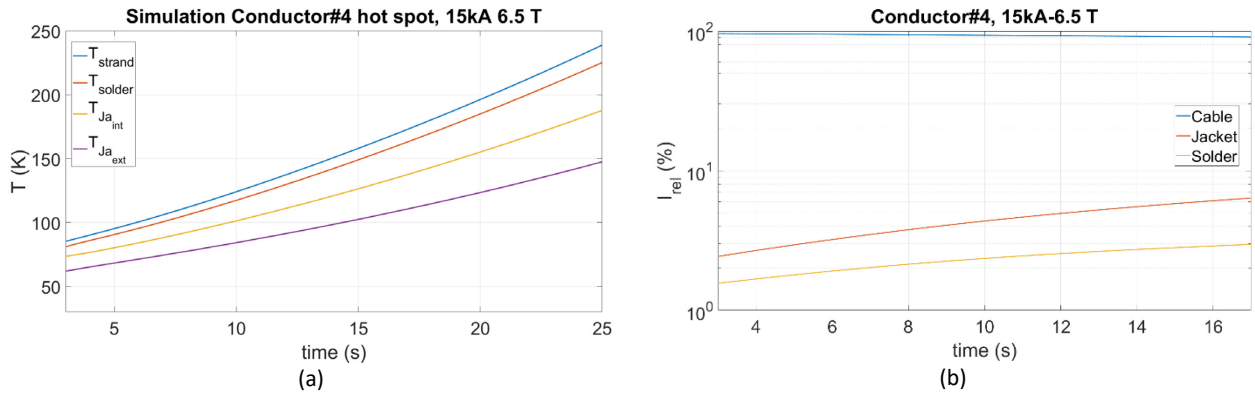


Figure 2:47 a) The simulated temperature evolution in the hot spot of the Conductor#4 at 15 kA-6.5 T for the several thermal components of the conductor. b) The simulated evolution of the relative current with respect to the operating one in the different electric components of the Conductor#4 at 15 kA-6.5 T.

2.6.2.3. The role of the thermal transverse resistance

As Figure 2:48 shows, the numerical models of Conductor#1 (twisted stack) and #3 (non-twisted stack) have the same temperature evolution if the $R_{th\ strand-Ja_{ext}}$ is set at the same value. This is because, at this temperature, the superconductor does not play any role: having the strands twisted or not does not make a difference. An educated guess about the difference in the thermal resistance between Conductor#1 and #3 is that by crimping the jacket to the same diameter, the gap between the cable and the internal wall of the jacket is smaller for the Conductor#1, with the twisted cable. The strands do not follow exactly the analytical trajectory of the helical cabling because of the anisotropic bending properties of the coated conductor, that is more difficult to bend in plane (hard bending) rather than along the longitudinal direction (see Figure 2:49). As a consequence, the final cable diameter is higher in hard bending parts rather than in the easy bending. The Conductor#3 is not twisted, so have a uniform cable diameter. Moreover, during the compaction the strands in the Conductor#3 have more freedom to move than in Conductor#1. For all these reasons, it is reasonable to think that the compaction left less gap in the Conductor#1 than in the Conductor#3. This could be also a possible explanation for the damage observed in the Conductor#1 (see paragraph 2.4.1).

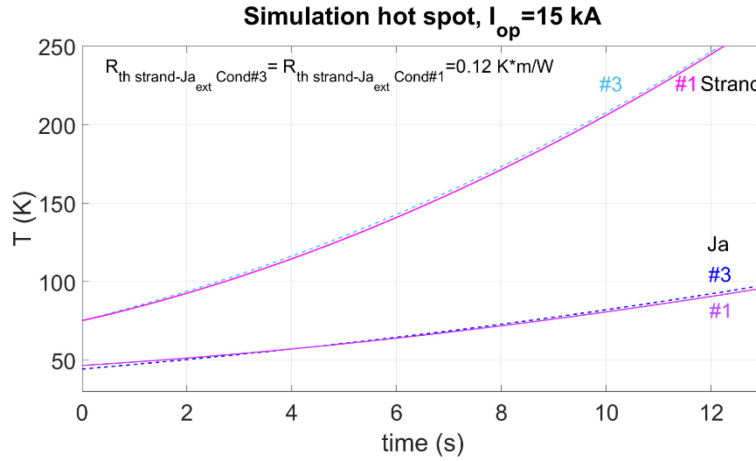


Figure 2:48 The simulated temperature evolution in the hot spot of the Conductor#1 and #3 at 15 kA in the strand and jacket. The same $R_{th \text{ strand-Ja}_{ext}}$ is set for both the conductors.

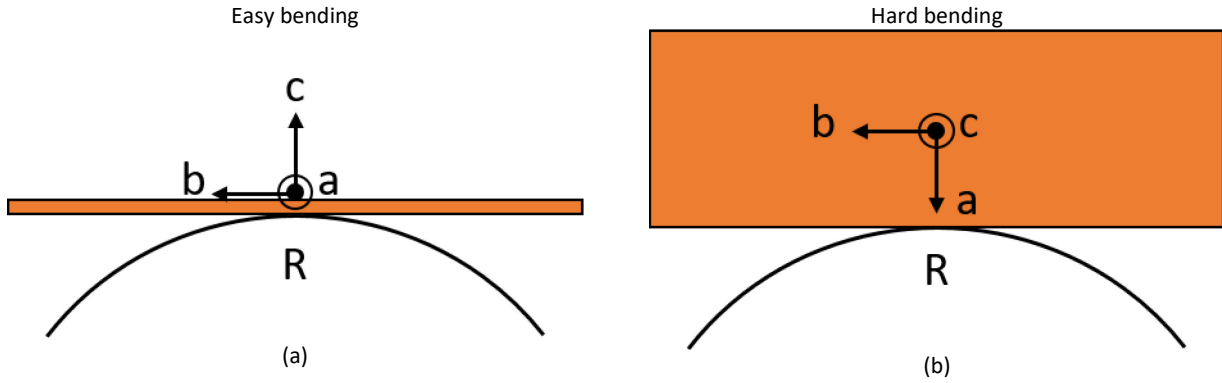


Figure 2:49. The tape bent in the easy bending a) and hard bending direction b).

Having proved that the Conductor#1 and #3 are different just for the thermal resistance between strands and jacket, it is possible to compare all conductors having the same materials with the same cross section just looking at the effect of the thermal resistance. In Figure 2:50a) the comparison among the three conductors is shown in terms of strand temperature evolution. Looking all the three conductors together is interesting to see how important is the thermal resistance for the temperature evolution: in the range of the thermal resistance of the Conductor #1 and #3, the temperature rate of increase is decreased by just few K/s by halving the $R_{th \text{ strand-Ja}_{ext}}$ (see Figure 2:50 b)), while it drops by tens of K/s by reducing $R_{th \text{ strand-Ja}_{ext}}$ by one order of magnitude drops of tens on K/s. This is important from the cable design point of view, to verify how safe is the maximum hot spot temperature reached during the current discharge (not treated in this dissertation). It is interesting to notice the effect that heat capacity of the solder has on the Conductor#4: without it the temperature increases faster: at 17 s the difference in the strand temperature is around 30 K, and not because the copper carries more current. Looking Figure 2:50 c) and comparing it with Figure 2:47 b), it is possible to see that the current that was flowing in the solder it is taken by the jacket, leaving the copper with the same fraction of current as in the case with solder.

By looking at the cable (copper) current as function of temperature (Figure 2:51), it is possible to see that till 150 K all the conductors behave the same, while when the temperature is above 150 K, the Conductor #4 has slightly more current . In this conductor, the jacket has higher temperature than in the others. Therefore, the electrical resistivity in the jacket of the Conductor#4 is higher, leading to have less current flowing in the jacket and more in the copper. Anyway, this difference is very small (about 1% of the operating current).

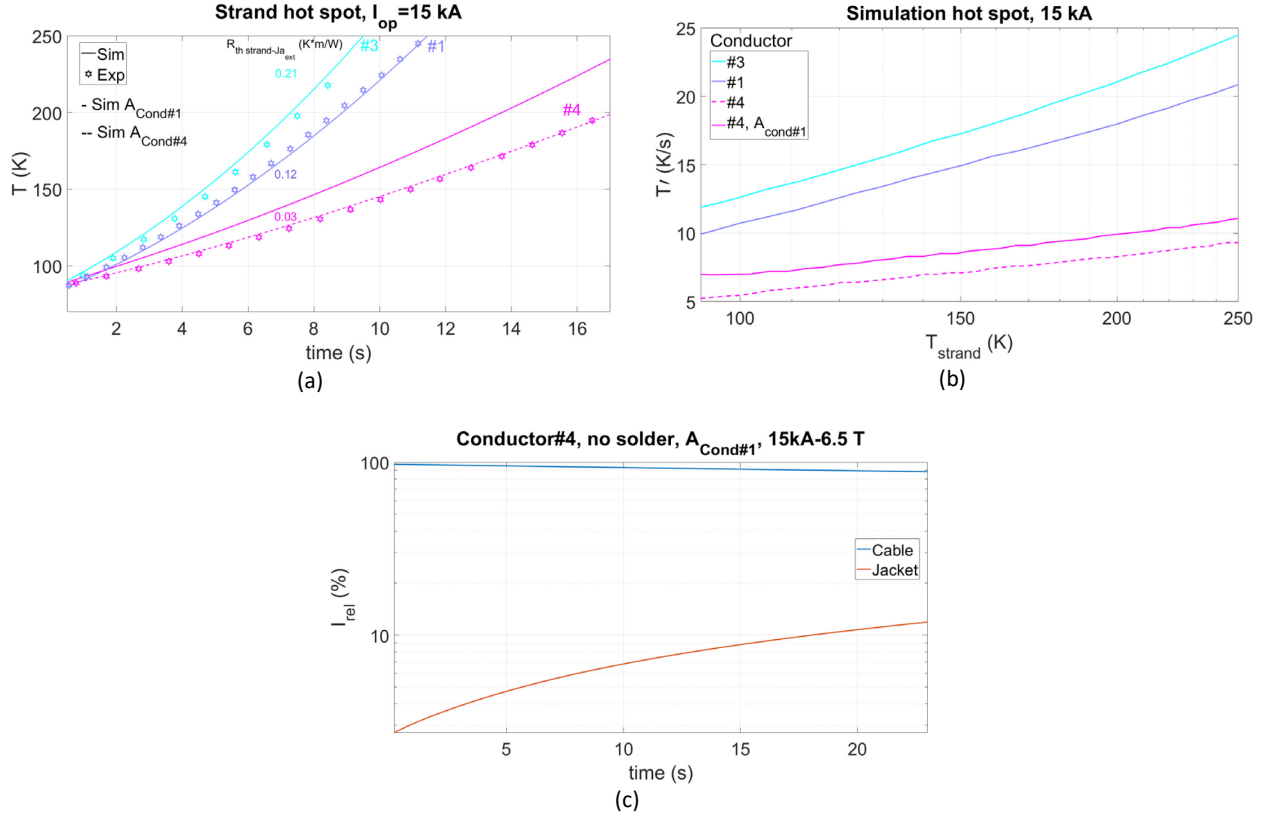


Figure 2:50 a) The simulated and experimental temperature evolution in the hot spot of the Conductor#1, #3 and #4 at 15 kA in the strand. The solid line is the strand temperature of the Conductor#4 without the solder and having set the same jacket cross section as in the Conductor#1 and #3. b) The simulated hot spot strand temperature derivative in time with respect to the strand temperature in the Conductor#1, #3 and #4 at 15 kA. The solid line is the strand temperature of the Conductor#4 without the solder and having set the same jacket cross section as in the Conductor#1 and #3. c) The relative current repartition in time among the cable and the jacket in the Conductor#4 without solder and with the jacket having the same cross section of the Conductor#1.

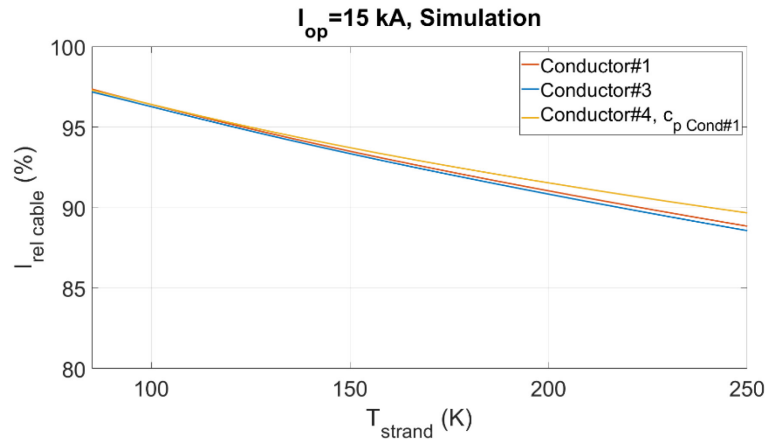


Figure 2:51 The simulated current carried by the copper in the hot spot in the Conductor #1, #3 and #4 with respect to the strand temperature. The conductors have the materials with the same cross section.

In conclusion, the validity of the model has been proved, in the analysed range of temperature and electric field, proving the importance of the thermal transverse resistance. The thermal transverse resistance, together with the cross section, can fully describe the quench development at high temperature. However, in all the experiments here analysed the quench was always initiated in all three strands at the same time. It is unclear if the conclusion is also valid when the quench is triggered in only one strand.

Another important point to stress is that the THEA code is 1D, with the heat propagating only in the longitudinal direction inside a given thermal element. In the radial direction, the temperature is constant in each element (steel, copper, He). A rudimentary 2D

heat propagation was included in the model by subdividing the jacket in two concentric shells. This may suggest that THEA code is not fully appropriate to model a thick jacket, but it is flexible enough to allow the user to modify the domain configuration and to get a better approximation of the physics.

2.7. The effect of the magnetic field profile

In the SULTAN quench experiments, the magnetic field along the length of the conductor is not constant, decreasing outside a relatively homogenous region of about 600 mm. Instead, in a large magnet, the conductor would be exposed to a homogenous field over several meters. What is the effect of the magnetic field profile on the total voltage developed during the quench? Is the voltage and temperature evolutions measured in the SULTAN quench experiments representative of what happens in a large magnet? To answer these questions, two additional simulations were carried out, one with the actual SULTAN magnetic field profile, and another one with a constant magnetic field along the length of the conductor.

The operating conditions are 3.5 T, 7 K and a current of 15 kA. The scaling law and the cross section of the conductor#1 are used. The helium mass flow rate was initially set at 1.7 g/s by adjusting the pressure drop along the conductor. The quench is triggered by heating up the helium at the beginning of the conductor on 1 cm length for 5 s with the power density of 5000 W/m. The helium travels along the conductor, and the quench develops at about 770 mm. The temperature and electric field profiles during the quench evolution are shown in Figure 2:52 a) and Figure 2:52 b). In the uniform field situation, the temperature downstream the hot spot ($z > 770$ mm) is higher than in the upstream branch ($z < 770$ mm). This happens because the heat generated by the cable is carried downstream by the helium, leading to a higher temperature of the cable in the downstream side than upstream. Instead, the temperature profile is symmetric with respect to the hot spot location in the SULTAN magnetic field profile case. The reason is that the critical current increases more and more for $z > 770$ mm, and the heat carried by the helium cannot quench the conductor.

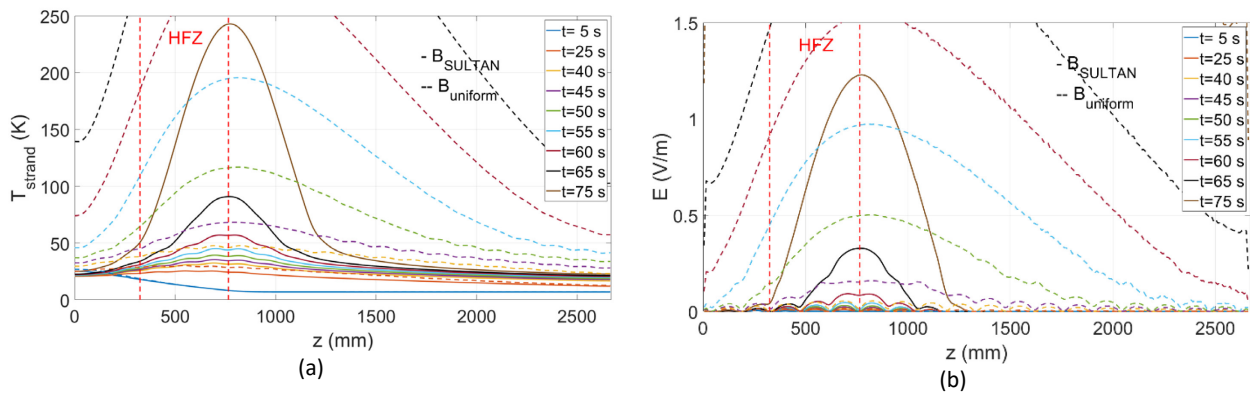


Figure 2:52 The quench development comparing the strand temperature (a) and the electric field (b) along the conductor length, at different times.

Before investigating the quench propagation, first a transition temperature has to be defined. For the definition of transition temperature T_t , the article of Bonura and Senatore [68] is taken as reference, in which T_t is the temperature at which the joule dissipation power $g_j(T)$ assumes its average value in the current sharing temperature range, between T_{cs} and T_c

$$g_j(T_t) = \frac{\int_{T_{cs}}^{T_c} g_j(T) dT}{(T_c - T_{cs})}$$

Equation 2:9- The average joule dissipation power in the current sharing regime evaluated as integral average between T_c and T_{cs} .

T_t is about 48.5 K. The position of the 48.5 K temperature as a function of time is plotted in Figure 2:53 for the two cases. It is possible to see how the normal zone is confined in the B_{SULTAN} case with respect to the uniform one, where also the NZPV is one order of magnitude faster (Figure 2:53 b)). The values found for the B_{SULTAN} case are qualitatively in agreement with what found in the section 2.5.3.

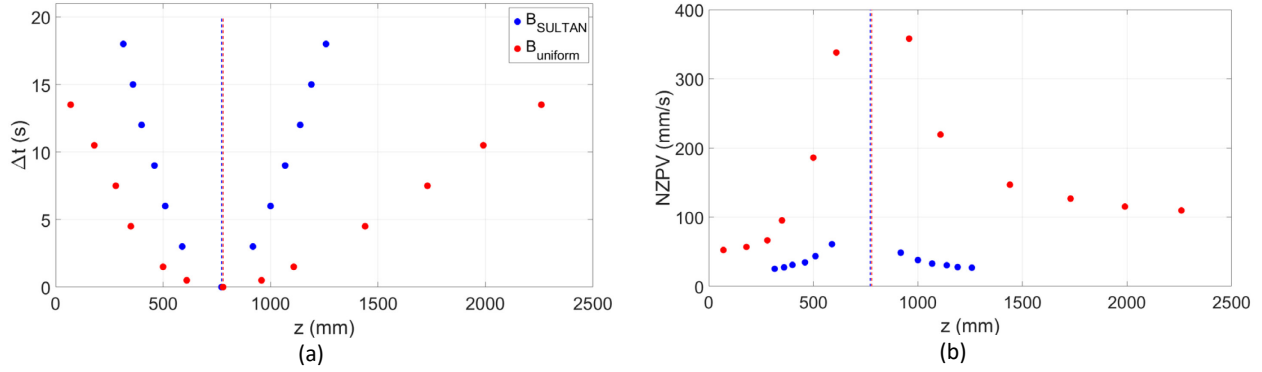


Figure 2:53 a) The normal length propagation in the B_{SULTAN} case and uniform one. The dashed lines point the hot spot; b) the NZPV in the B_{SULTAN} case and uniform one along the conductor length.

As a consequence of the different normal zone propagation between SULTAN and uniform cases, the total voltage grows faster in the uniform case than in SULTAN (Figure 2:54 a)). Moreover, being the normal zone larger in the uniform magnetic field, for a given voltage, the temperature in the hot spot is lower. For example, at 0.1 V, the T_{strand} in the hot spot is 59 K in the uniform field case and 83 K in the SULTAN case ((Figure 2:54 b)). If this value is used as voltage detection, as in ITER, there is more time to reach the safety limit of 200 K on the strand temperature: 12 s in the uniform case, instead of 9 s with the SULTAN magnetic field profile(Figure 2:54 c)).

This leads to the conclusion that the SULTAN quench experiment may not be appropriate to draw conclusions about the total voltage and hot spot temperature evolutions. However, it is interesting to notice that, in both magnetic field cases, the total voltage evolution has two regimes: one slow between roughly $1e-3$ and $5e-2$ V, and one fast, above $5e-2$ V (see Figure 2:54 a)). In the fast one, most of the current flows in the copper and the propagation speed is determined only by the copper current density and the thermal resistance between the cable and the jacket. In the slow regime, the superconductor still carries a large current, thus the joule heating is relatively low. This slow voltage rising is called drift. Therefore, if a quench detection threshold is used in this range, a long validation time can be used to recognise the quench as a slow but constantly increasing voltage signal, allowing to start the current dump before reaching the high time constant regime. Alternately, the quench can be detected by measuring the corresponding slow temperature drift (Figure 2:54 a)), for example using optical fibers. In this case, the signal is based on the local temperature, avoiding the problem of induced electromagnetic noise on the voltage. One example of voltage detection by optical fibers on relevant HTS fusion cable VIPER has been studied by Salazar et al. in [19].

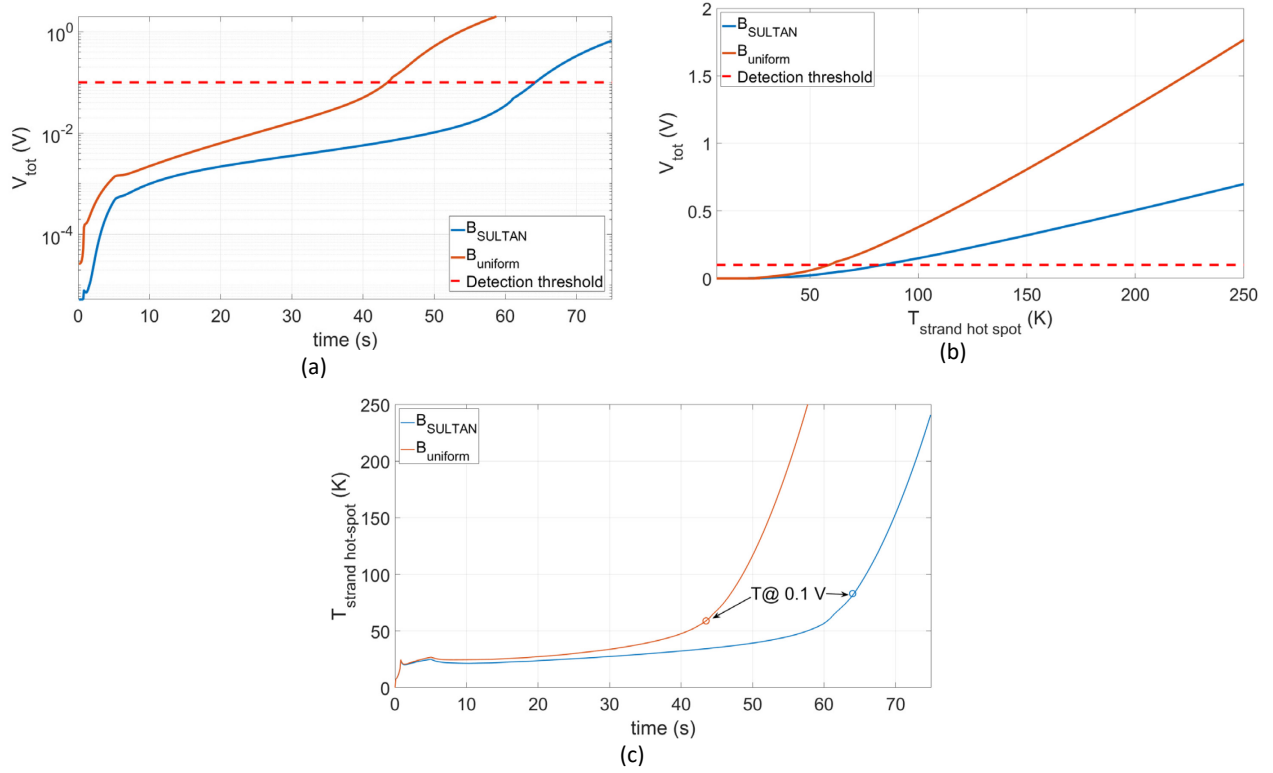


Figure 2:54 a) The total voltage evolution in the B_{SULTAN} case and uniform one. The red dashed line indicates the detection threshold voltage (0.1 V); b) the total voltage vs the strand hot spot temperature in the B_{SULTAN} case and uniform one. The red dashed line indicates the detection threshold voltage (0.1 V); c) The strand temperature evolution in the hot spot.

Chapter 3 Strands transverse pressure tests

In this chapter, various modifications of the round twisted stack strand (starting from the cable designs described in 3.1) are considered, aiming to improve the transverse pressure performance, i.e. in other words, the ultimate pressure at which the critical current degrades irreversibly. The transverse stress tolerance of various strand types is measured and reported in 3.2. In addition, a mechanical model is used to interpret of the results and provide suggestions for enhancing the performance of the strand under transverse load (section 3.3).

3.1. Cable designs

Two designs for the EU DEMO CS hybrid module operated at 53 kA, 18 T were considered in the 2017 paper [69]: a round cable composed of six large strands cabled around a copper bar, and a flat cable, similar to the 2015 prototype. The strands are manufactured according the SPC TSTC design, in which the stack of tapes is enclosed between two half cylindrical copper profiles. The strand is then twisted and soldered (see section 1.3.2). The split line is the soldered junction between the two copper profiles. Both designs have two advantages. The first is the reduction of the cabling strain, which is a consequence of the reduction in the number of strands. In this thesis, a further peak tensile cabling strain reduction is considered, increasing the twist pitch from 1 to 2 m. The second advantage concerns the transverse pressure. The split line is in a plane perpendicular to the wide face of the tapes, while, in the 2015 prototype, was in the same plane as the tapes. This modification is useful to better withstand the transverse pressure originated by the Lorentz force. In [34] it was shown that rotating the split line by 90° (having it perpendicular to the wide tape face) reduces the I_c degradation at the same pressure. In this case, the opening of the split line, caused when the force acts along the same direction, does not lead to a separation of the stack, avoiding the delamination (pressure limit 10-70 MPa) and cleavage of the tapes (1 MPa). To further improve the mechanical resistance of the strands, in the round conductor, the copper shells were not annealed: as the copper is harder, the deformation is lower [34].

In all conductors fabricated with round strands, the strands can deform because there are empty spaces around each strand. The coolant passes through them in forced flow to directly cool the cable. The disadvantage of this configuration is that the strands are not supported laterally and can deform under the effect of the Lorentz force. However, the strand deformation can be contained by filling up the voids and moving the helium to a dedicated cooling channel. Example of full impregnated (solid) cables are: Rutherford cable for accelerator, fully impregnated with epoxy resin; the SULTAN conductor [70] where the He flows in a separated channel, and the space between round strands is occupied by solder. Recently, the HTS VIPER conductor, manufactured by Commonwealth Fusion Systems, has shown negligible reduction of performance under transverse electromagnetic cycling (2-4%). This excellent result was attributed to the absence of deformation in the stack, being the conductor a bulk of copper in which the stacks were soldered, with a good quality soldering process (void sizes under $\sim 3 \text{ mm}^3$ and void fractions under $\sim 5\%$). Thanks to the robust mechanical support, the critical current does not degrade under static and cyclic loads [50].

Following these examples, another design is explored for the first time in the framework of this thesis: the Twisted Soldered Tapes Stack on flat core, where the tapes are individually cabled around the central flat copper core (see Table 3:1). The ceramic side of the tape is facing the copper core. In this way, the ceramic is longitudinally compressed after cabling, while the previous concepts resulted in longitudinal tensile strain. The cable twist pitch is set around 600 mm. After cabling, the cable is solder filled and then the jacket is welded around the cable. In this way, a mechanically robust structure is obtained, since the deformation under transverse load is almost negligible, because there is no empty space left for deformation. The cable is “fully bonded”, meaning that the different elements are not free to move with respect to each other. It follows that the cable must be relatively thin. The coolant flows in a separate channel. In this design, the cooling efficiency is somehow reduced, because the effective perimeter wetted by helium is much smaller than in the other two designs. The effect on heat removal (for example AC loss energy deposited in the cable) has not yet been investigated

The technical design specification of the cable described above are listed in Table 3:1, to be operated at 53 kA and 18 T, 4.75 K. All these conductors are twisted. Hence, even though the direction of the force is perpendicular to the cable direction, the tapes experience the force in all directions. In some locations, the stack is subject also to shear stress (pressure limit 19 MPa) and tensile transverse stress (pressure limit 10-70 MPa), against which the tapes are very weak. This is the reason why testing the strands under transverse stress is of particular importance.

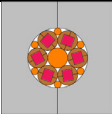

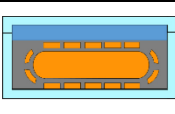
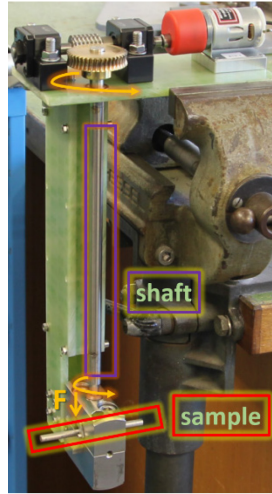
			
Design Type	6 around 1	Copper-core Rutherford	Twisted Soldered Tapes Stack on flat core
Copper shells	Not-annealed	Annealed	/
Cable twist pitch (m)	2	2	0.6
Stack twist pitch (m)	0.4	0.4	0.6
Core thickness (mm)	10	5	6
Longitudinal tensile strain (cabling+winding on R=1.9 m)	0.22% (zero friction) – 0.75% (fully bonded)	0.21% (zero friction) – 0.52% (fully bonded)	0.15 % (fully bonded)
Nominal transverse Pressure (MPs)	48	23	19
Number of strands/stacks	6	12	30
Number of tapes/ stack	40	28	11
Tape width (mm)	4.8	3.3	3.3
Strand outer diameter (mm)	10	7	/
Slot shape	Square	Square	/
Split line	// c axis	// c axis	/

Table 3:1 The design featured of the different designs considered for a the CS in DEMO. The TSTS on flat core sketch is an artistic representation. The drawing for the 6 around 1 and Copper-core Rutherford cables are taken from [69].

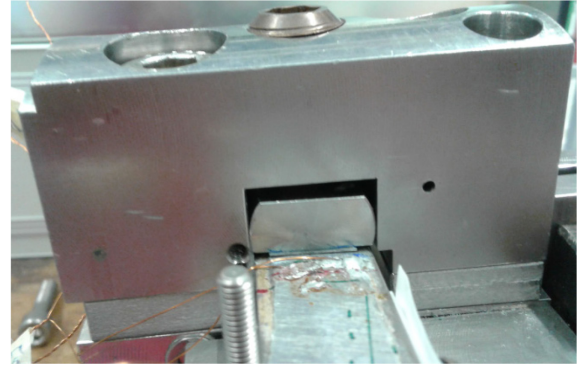
3.2. Transverse pressure tests

The strands are subjected to a significant transverse stress when the magnet is in operation. The stress is a combination of direct $B \times I$, and stress accumulation from the other strands. In particular, in the case of the flat design, the bottom layer bears also the force coming from the top one, while, in the round cable, the bottom strand sees its own Lorentz force plus that of the two strands on top. In order to simulate the operating transverse stress in a simple experiment, a mechanical press is used. It is important to notice that, in the experiment, all the tapes in the stack see the same pressure. Instead, the Lorentz force during magnet operation is a body force, and is linearly increasing till the last tape of the stack, where the force is maximum. Despite this significant difference, the test is still valuable, because it can show which design is particularly weak and moreover, it is conservative, since all the tapes face the same force and not just the bottom one. The objective is to measure the maximum transverse stress that each design is able to withstand, and verify that this value is larger than the expected transverse stress in the conductor during operation.

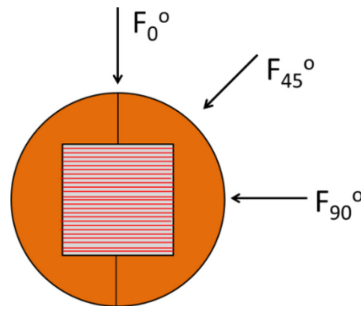
The force was applied by a motor, connected with gears and a shaft to a bolt, which converts the torque to load on an anvil located on top of the strand (Figure 3:1 a) and b)). A piezoelectric sensor, located under the strand, measures the applied force. The midplane pressure is obtained as the measured force divided by the diameter of the strand and the length of the anvil. The pressure is increased in steps till the critical current decreases irreversibly. This limit pressure is compared to the maximum stress foreseen in the cable under operating condition, which is on the bottom layer, to evaluate if the strand can be suitable for the cable design considered. The critical current is measured by the four point method, in the liquid nitrogen, at self-field. The threshold on the electric field E_0 to fit the E-I measurements is $1 \mu\text{V}/\text{cm}$. Being the stack twisted, all the force orientations are possible. In this kind of test, an important parameter is the orientation of the force with respect to the normal of the wide tape surface and the split line. The orientations considered are 0° , 45° and 90° (Figure 3:1 c)), the angle is between the normal to the wide tape surface (c axis) and the force direction. In the 0° direction, the force is aligned this the split line. In the 45° direction, shear stress in the stack is induced, while at 90° the transverse deformation (with respect the force direction) causes the tape delamination. Different zones with different orientations of the force were analysed (Figure 3:2). The length of the anvil is of the order of the diameter (20-30 mm with respect to 7-10 mm, respectively). This comes from the limitation of the force and pressure that this set up can apply.



(a)



(b)



(c)

Figure 3:1 a) The experimental set-up for the transverse pressure test, picture from [31]; b) the anvil, positioned on the TSTC on flat core sample; c) the sketch of the different orientation of the transverse force applied during the test the experimental results

3.2.1. Strand for the 6 around 1 conductor: thick hard copper

The copper used for 6 around 1 design is cold worked. More specifically, according to the Vicker test, its hardness is 110. This specific strand design can withstand the cable pressure load in static DC operation (reported in Table 3:1), even if the margin is relatively small (around 12 MPa, Figure 3:3). With respect to the results presented in [34], the critical pressure values are increased from 40 MPa to about 60 MPa, thanks to the hard copper. Moreover, not-annealing the profiles improves the performance at 90° direction (almost no degradation is found up to 90 MPa) with respect to the annealing case (see [34]), even if the strand dimensions are different. The decision of not annealing the copper profiles may lead to low value of RRR. Having high RRR copper placed in parallel to the superconductor is beneficial for the stability of the conductor. However, the HTS conductor is very stable if compared to LTS, meaning that the MQE is much higher (three orders of magnitude at 4.2 K [16]). As a consequence, the reduction of RRR due to the lack of the annealing process is considered by the author not a relevant problem for the stability of the HTS conductor. However, a high RRR copper may also be useful to slow down the voltage drift observed in the section 2.7, increasing the maximum allowed validation time. Nevertheless, the effect of RRR on the electrical resistivity decreases increasing the temperature. The current sharing regime in HTS is very broad in temperature (from about 7.5 K to 70 K), as seen in the analysis of the Quench Experiment. In this range of temperatures, the ratio in electrical resistivity at 0 T between a copper of RRR 40 and 300 decreases from 7.5 at 7.5 K to 1.3 at 70 K (see Figure 3:4). Moreover, the magneto resistance of the copper decreases the difference between the electrical resistivity at different RRR even at low temperature. From this consideration, it is possible assume that the gain in validation time that is possible to obtain by increasing the RRR might not be significant. Anyway, a computational parametrical study needs to be done in a wide range of RRR, in order to quantify the effect also in the NZPV, and so, on the total voltage evolution. From the results of the transverse pressure test, the degradation along the 45° orientation is probably caused by the shear stress in the stack, and by the solder deformation. Instead, the degradation in the 0° direction is linked to the opening of the split line: a possible explanation is that the two shells separation leads shearing stress on the top tape, with the ceramic facing the top of the stack.

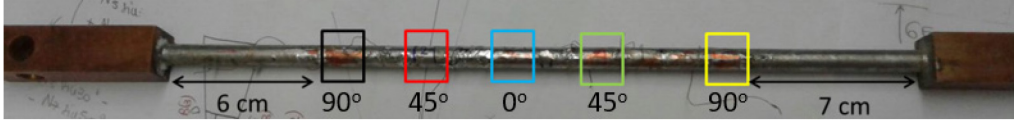


Figure 3:2 The strand for the 6 around 1 cable assembled for the transverse pressure. The regions tested to have the results at different orientations are highlighted.

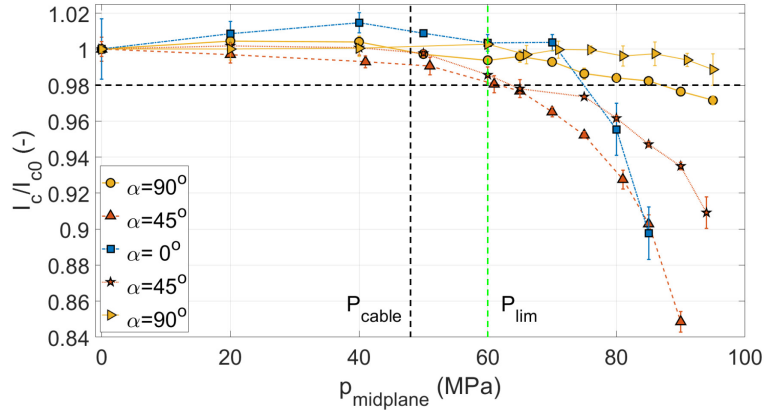


Figure 3:3 The critical current relative to pristine one of the not-annealed strand as function of the pressure at the midplane ($p_{midplane}$). The force was applied along three different directions. The set degradation threshold (0.98) is highlighted, as the cable nominal pressure. The error bar indicates the reproducibility of the measurements, being the standard deviation obtained by several of them.

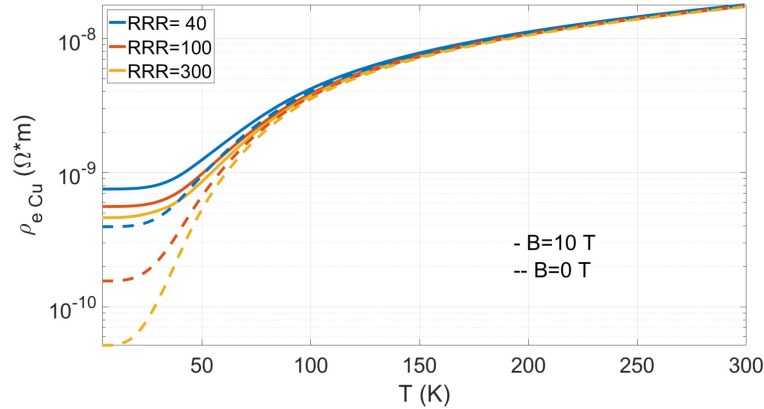


Figure 3:4. The electrical resistivity of copper as function of the temperature for different RRR at 0 and 10 T.

3.2.2. Strand for the flat cable: thin annealed copper

The flat cable strands are bent to a smaller radius than in the round cable. In order to simplify the cabling process, the copper shells for the strand of the Rutherford like cable are annealed at 500° C for two hours, (hardness of 46, according to the Vicker test). The other difference is that the flat cable strands have a smaller diameter than the round cable strands. As shown in (Figure 3:5 a)), the measured critical pressure is lower than nominal cable value (reported in Table 3:1). Moreover, the I_c degradation is similar in all directions. This means that the deformation of the soldered strand needs to be limited in all the directions.

This experiment was designed to understand if the I_c degradation could be just the result of a reversible strain induced by the plastic deformation of the shells or, instead, is due to an irreversible reduction of I_c . For this reason, the critical current of each tape of the stack in the different regions was measured before the strand assembly. The test is stopped after having reached the strand irreversibility limit (Figure 3:5 b)). After the transverse pressure test, the tapes were dis-soldered, extracted from the strand and measured again in all locations where the force was applied. No tapes were damaged during the strand assembly: the strand critical current obtained by the analytical model (see section 2.4.1), whose input is the tape I_c measured before the strand assembly, is close to the one measured at zero pressure (Figure 3:6). However, the strand critical current computed from the I_c measured on the extracted

tapes is lower than the measured strand I_c . This leads to the conclusion that the extraction process has further degraded the critical current. This experiment is therefore inconclusive.

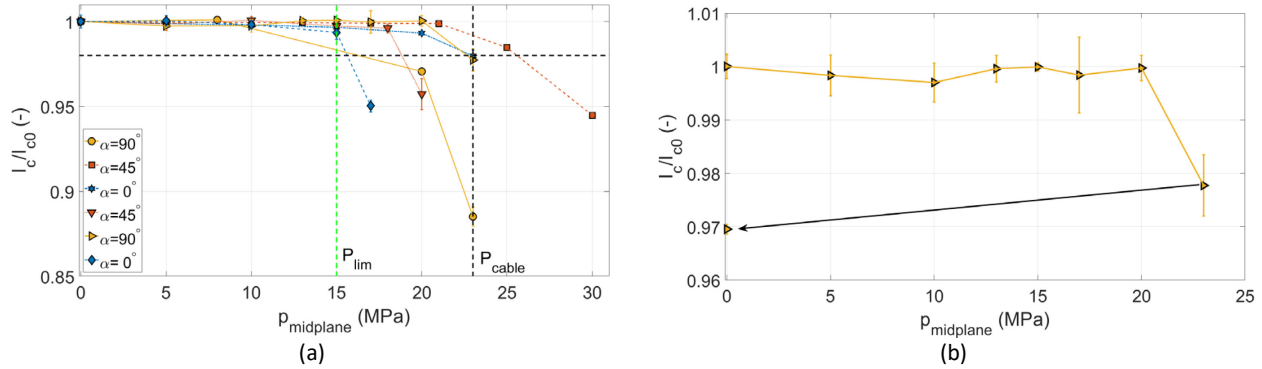


Figure 3:5 a) The critical current relative to the pristine one of the annealed strand as function of the pressure at the midplane ($p_{midplane}$). The force was applied along three different directions. The degradation threshold (horizontal dashed line) and the nominal value of the pressure at the mid-plane in the cable (vertical dashed line) are highlighted. The error bar indicates the reproducibility of the measurements, being the standard deviation obtained by several of them. b) The relative critical current degradation at 90° to show the irreversibility of the results obtained going back to 0 MPa.

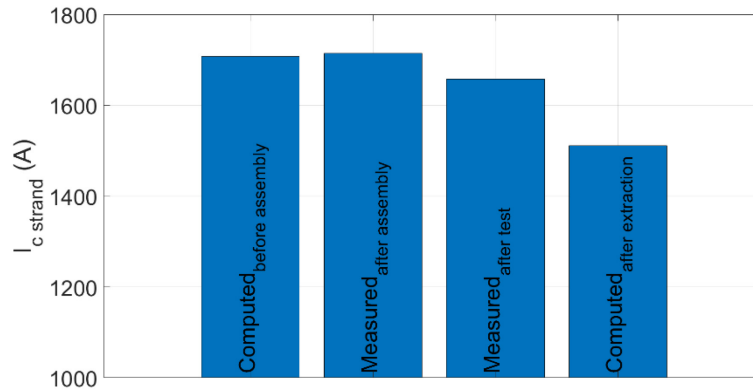


Figure 3:6 The history of strand critical current from the strand assembly to the tapes extraction. The strand critical current before assembly and after extraction tapes are computed from the measured tape I_c , while the others are measured.

3.2.3. Strand for the flat cable: reinforced and not-soldered stack

The results of the previous tests suggest that the copper profile deformation is responsible of the poor performance under transverse stress. A possible solution would be to increase the stiffness of the copper profiles, but at the same time keeping the flexibility of the annealed copper profiles. A first tentative was to wrap the strand with a steel tape in tension, which should reduce the deformation of the copper. The wrapping of the strand by stainless steel tape was attempted, but the bending trials on a dummy copper strand were not satisfactory, since the tape cannot fully follow the curvature of the strand during bending. In particular, the gap between the different turns under tension becomes bigger, while the gap completely closes in the part in tension (see Figure 3:7). It is then considered to wrap the strand using a wire instead of a tape.

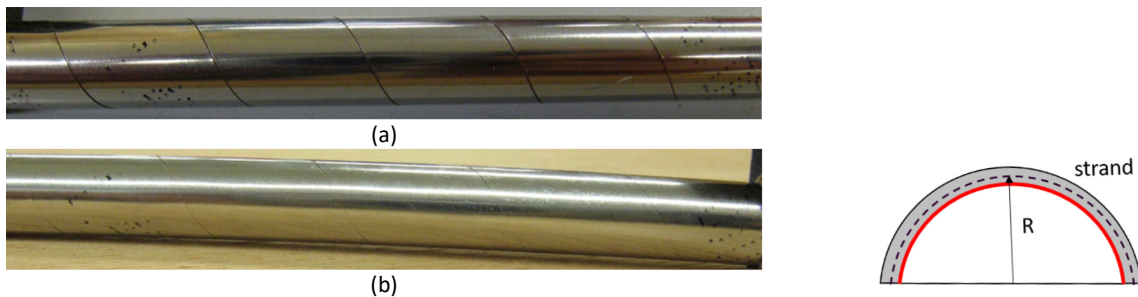




Figure 3:7 The dummy strand wrapped by the steel tape when straight a), bent on a radius of 320 mm in the compression side $R=320$ mm b), bent on a radius of 320 mm in the tension side c).

The deformation of the copper profiles induces transverse tensile strain and/or shearing strain on the tapes, which can result in delamination. One way to eliminate tape delamination is simply avoiding soldering the tapes together: the tapes are free to move when the transverse pressure deforms the copper shells, avoiding the delamination. Thus, the next strand design tested for the Rutherford like cable with annealed copper shells is based on non-soldered strand, wrapped by stainless steel wire (AISI 304, 0.5 mm). The function of the wire wrapping is to hold the components (copper shells and stack) together, and guarantee some contact among tapes and copper, so that they can exchange current. Since the groove was too big for the stack (28 tapes) without the solder filling, in order to increase compactness of the stack in the groove (and so reducing the inter-tape resistance), two extra copper tapes were added in the stack. An extra indium tape was inserted perpendicular to stack, to decrease the electrical transverse resistance between the stack and the copper (Figure 3:8 a)). The strand is twisted and then wrapped by the stainless steel wire with a constant tension of 30 N (Figure 3:8 b)).



Figure 3:8 a) The sketch of the new strand design for the Rutherford like cable, made of not-soldered stack and wrapped by the steel wire ; b) the strand prepared for the transverse pressure test.

The results of the test are reported in terms of force, since the transverse deformation of not-soldered strands is not negligible. The length of the anvil is 30 mm. The transverse force at which the irreversibility is reached is lower than that one foreseen in the cable (Figure 3:9). As in the soldered strand in the previous strand configuration, no difference between the different directions has been noticed. The most important problem that raised during the measurement is the large scatter of the value of I_c , because of the large inter-tape resistance. The plastic deformation of the copper shells diameter is high: $\sim \pm 10\%$ ($\sim \pm 1$ mm), see Figure 3:10. For all these reasons such a conductor design is deemed not reliable and will not be used for the CS cable prototype. Actually, the experimental conditions were not reproducing the real cable environment, in which the cable is inserted in a jacket and where the space left to the strands to deform (space around the strands and the insertion tolerance) is much less than in this experiment, where the strand deformation was not confined laterally.

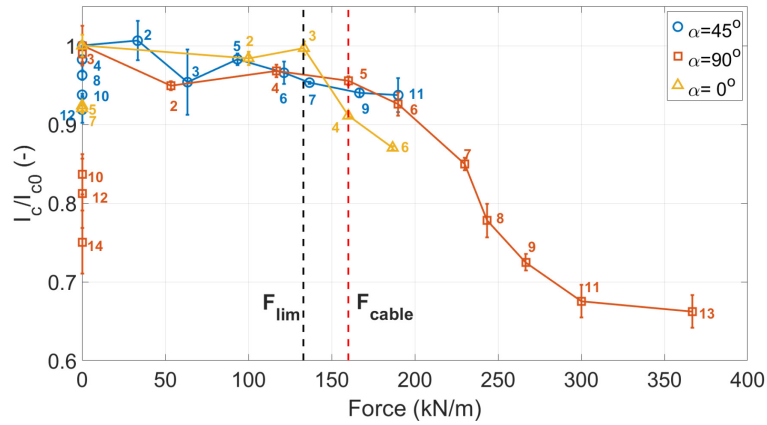


Figure 3:9 The critical current relative to the pristine one of the not-soldered reinforced annealed strand as function of applied force per unit length for different direction of the force. The cable nominal force is highlighted. The error bar indicates the reproducibility of the measurements, being the standard deviation obtained by several of them. The numbers indicate the measurement sequence.

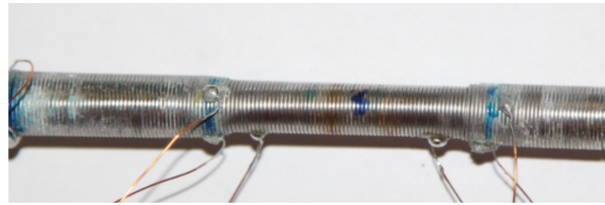


Figure 3:10 The deformation of the strand after the application of the transverse load.

3.2.4. Sub-size for the Twisted Soldered Tapes Stack on flat core conductor

A sub-size sample of the Twisted Soldered Tapes Stack on flat core was manufactured with the characteristics in Table 3:2. This sample contains only one stack of tapes. The solder used as filler is $\text{Sn}_{60}\text{Pb}_{40}$. This solder would shrink during solidification. The conductor is tested in two directions: the edge Figure 3:11 a) and c) and the bottom d). The length of the anvil is 30 mm and it was pressing on the whole conductor width directly on the solder (Figure 3:11 b)). The pressure is computed as the force recorded by the piezoelectric sensor divided by the width of the conductor and by the length of the anvil. The results of the test show that the edge direction is the worst (Figure 3:11 e)). A possible explanation is that the solder locally deforms under the anvil print, inducing deformation on the stack. Nevertheless, the pressure identified as limit pressure is higher than the nominal one expected in the cable (reported in Table 3:1), even if the margin is small.

Features of the sample	
Tape	SST tape, 3.3 mm width
Tapes/stack	10
Cabling angle	10°
Core thickness	6 mm

Table 3:2 The feature of the TSTC on flat core sample for the transverse pressure test.

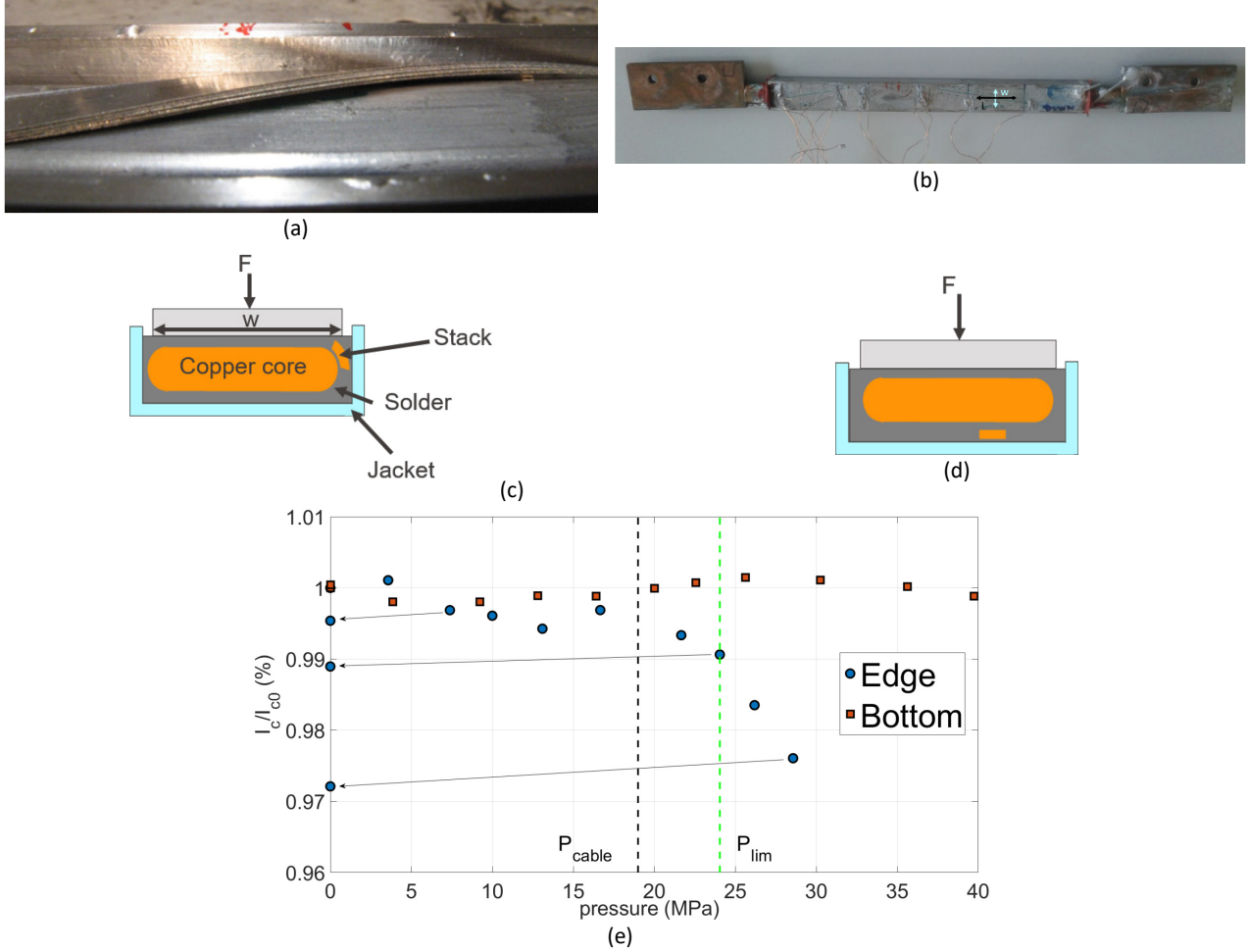


Figure 3:11 a) The stack on the edge of the copper core before the solder filling; b) The sample after the solder filling; the sketch of the edge c) and bottom d); e) The critical current relative to the pristine one of the new annealed strand as function of applied pressure. The cable pressure and the one at which the irreversibility limit is reached, are highlighted.

3.3. The mechanical model

In order to qualitatively understand the behaviour of the soldered round strands under transverse pressure, a numerical FE model was prepared in ANSYS 19 [71]. In particular, the reinforcement of the soldered strand by wrapping it by a wire under tension was investigated. With this strategy, it is possible to radially precompress the strand, decreasing the final deformation under transverse pressure. The role of different wire materials, the hardness of the copper shells and the geometrical dimensions are explored. The model considers a simplified 2D generalized plain strain (free endings). The symmetry of the problem is exploited, describing just one quarter of the strand and setting the displacement equal to zero across the symmetric line boundaries (see Figure 3:12). The Lorentz force is not simulated as a body force, but as external force, to avoid a too complex geometrical description of every single tape in the stack. Thanks to this, the mesh (multizone quad/tri, average size 7e-2mm, refined to 5e-2mm anvil-wire point of contact) is much simpler and the model is conservative: the maximum force is applied to the full stack evenly, as it is in the real transverse pressure test. The force is 115 kN/m (32 MPa at the midplane), while it is 80 kN/m in the Rutherford cable design (23 MPa at the midplane), to maintain some margin with respect to the operation. Being the model 2D, the wire is modelled as a wrapping layer around the strand. This means that, actually, there is no difference between a wire and a pipe. For simplicity, here a wire is considered. The wire tension before cool down is 30 N. The cool-down from room temperature to 77 K is considered, taking into account also the temperature dependence of the thermal expansion coefficient [72] and of the yield strength (see Table 3:3 and Figure 3:13). A plastic bilinear model describes the plastic behaviour of the materials (Figure 3:14). The contacts between the stack and between the solder and the solder and copper are bounded, while the one between the wire and the strand and the strand (or wire) with the anvil are frictional, with a friction factor 0.1. The strand deformation is studied in two configurations: when the force is parallel to the tapes (the worst case for the delamination, 90°) and at the angle between force and tapes of 45°, in which the shear stress (against which the tapes has poor electro-mechanical performance) has an important role.

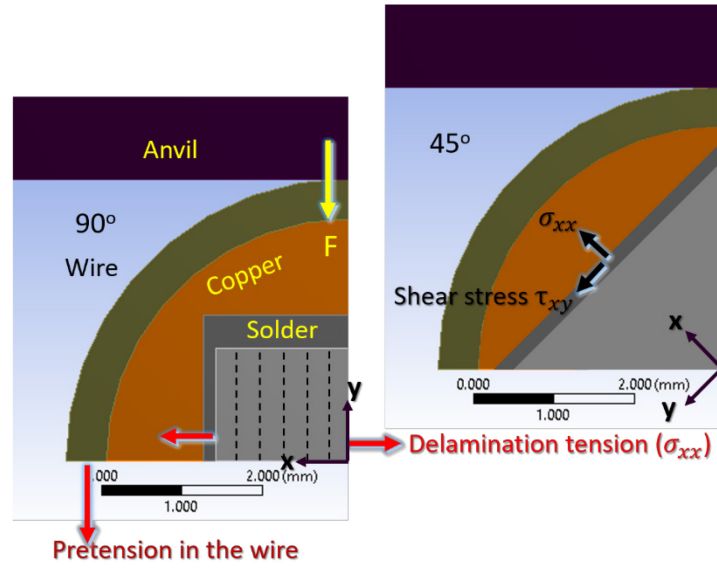


Figure 3:12 The sketch of the domain in the 90° and 45° orientation.

Material	Yield stress @ 77 K (MPa)	Yield stress @ RT (MPa)
Tape [73]	810	620
Cu (cold worked) [73]	387	333
Steel AISI 301 [71]	287	250
Alu alloy [71]	324	280
Sn ₆₀ Pb ₄₀ [73]	110	57
Cu (annealed) [74]	65	33

Table 3:3 The yield stress at 77 K and RT for the materials considered in the model.

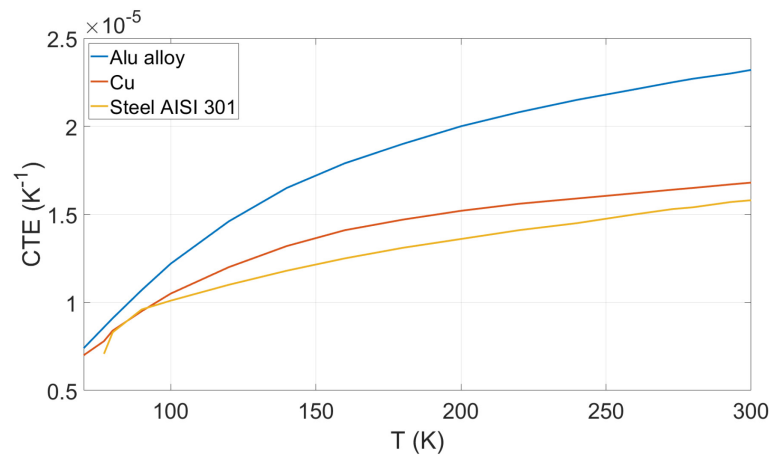


Figure 3:13 The thermal expansion coefficient of the Alu alloy, copper and steel as function of temperature.

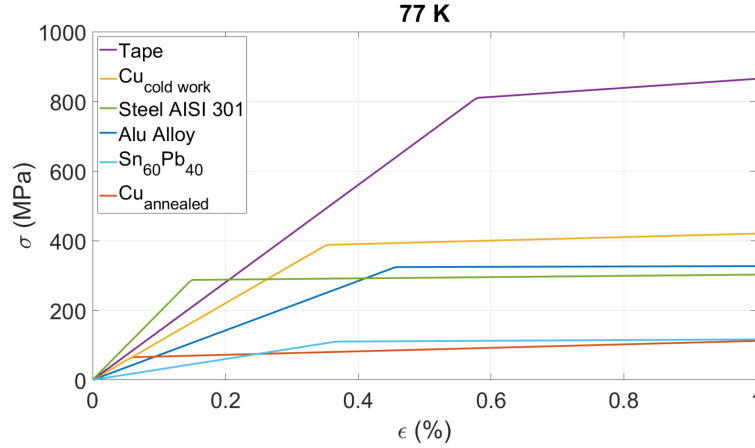


Figure 3:14 Tensile stress-strain curve for the materials considered in the model.

The results for the strands of the Rutherford-like cable are shown as the cumulative fraction of the cross section in the stack with respect to the tension σ_{xx} , that is the one inducing the delamination in the stack, for both 90° and 45° direction. The results are retrieved from the values of σ_{xx} in each element in the stack cross section after the cool down and the force application. In the graph, it is reported the fraction of the cross section in which the value of σ_{xx} is lower than the one reported in the x axis. For example, looking at Figure 3:15, 70 % of the cross section in the stack cross section (sum of the blue, light blue and yellow areas with respect to the total stack cross section) has a σ_{xx} below 10 MPa. The effect of different wire material, wire thickness, copper cross section material and dimensions, are reported for the 90° direction and the 45° direction, in terms of the cumulative fraction of the cross section with respect to the delamination tension (Figure 3:16 and Figure 3:17) and the shear stress (only for the 45° orientation, Figure 3:18). The limiting pressure in terms of the delamination and shear stress are highlighted (taken from [25]) by red dashed lines, to show how much of the stack cross section overcomes the limit. To obtain a good reinforcement by wrapping the strand by a wire in tension, the wire material has to have a coefficient of thermal expansion higher than copper. In this way, the wire shrinks more than the copper, keeping always the contact between the copper and the wire. If a gap opens then the pre-compression obtained by wrapping the strand by a strand in tension vanishes, as it happens with a steel wire. If the wire is not hard enough (yield strength at 77 K > 250 MPa), the wire plastic deformation under transverse load makes a gap opens at the contact between the wire and the strand, losing the radial precompression obtained during the pretension and the cool down (see Figure 3:19). In order to increase this effect, a thicker wire can be used, such that it would shrink even more during the cool down. To maintain the total design diameter, the copper shell diameter can be decreased. A material with these characteristics is the Alu alloy 7075 T7. Unfortunately, the solutions proposed are not helpful to decrease the shear stress at 45° .

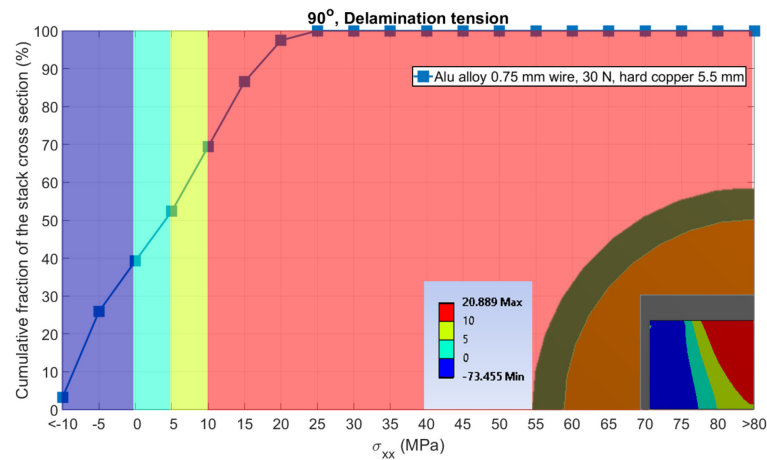


Figure 3:15 The cumulative of the fraction of the stack cross section vs the tensile strain along the x axis in the 90° orientation. The copper outer diameter is 5.5 mm, the wire wrapped around the copper is in Alu alloy of 0.75 mm diameter and the pretension force on the wire is 30 N. The cross section of the strand is illustrated in the bottom right corner, with the values of the tension along the x axis shown in the stack. The coloured bar in the plot have the same colours illustrated in the stack cross section

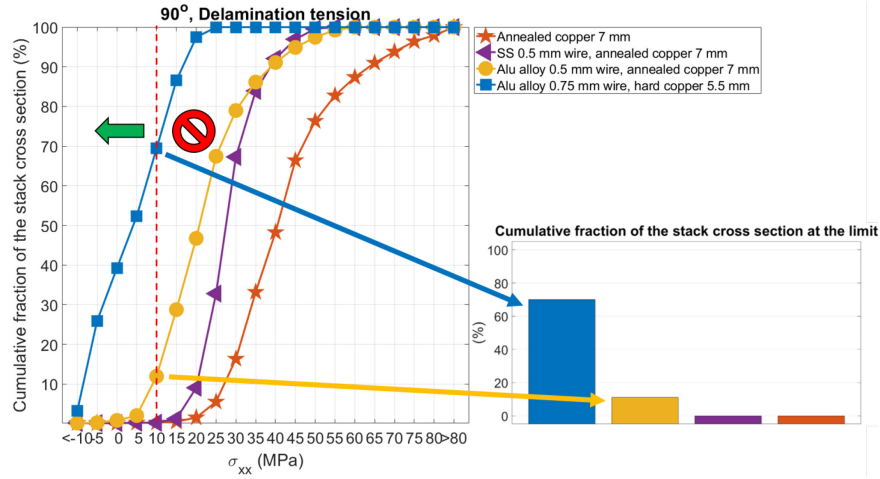


Figure 3:16 The cumulative of the fraction of the stack cross section vs the tensile strain along the x axis in the 90° orientation, for different wire materials, wire and copper shell outer diameter. SS stands for stainless steel. The dashed red line represents the limiting value of delamination tension for the tapes and it is taken from [25]. In all the scenarios with a wire, the tension applied on the wire during the wrapping (before the cool down) is 30 N. In the bottom right corner, the cumulative fraction of the stack cross section at the limiting value of delamination tension is shown for the various cases considered. The colour code is the same of the plot on the left side.

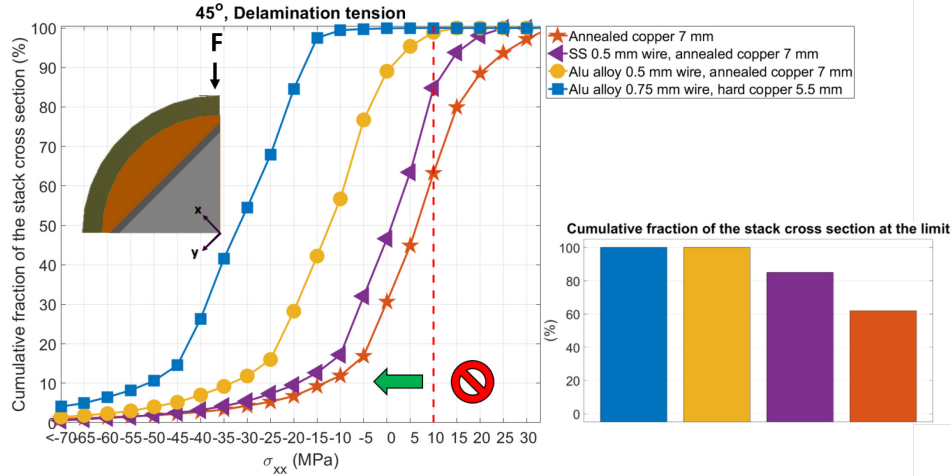


Figure 3:17 The cumulative of the fraction of the stack cross section vs the tensile strain along the x axis in the 45° orientation when the maximum force is applied, for different wire materials, wire and copper shell outer diameter. SS stands for stainless steel. The dashed red line represents the limiting value of delamination tension for the tapes and it is taken from [25]. In all the scenario with a wire, the tension applied on the wire during the wrapping (before the cool down) is 30 N. In the bottom right corner, the cumulative fraction of the stack cross section at the limiting value of delamination tension is shown for the various cases considered. The colour code is the same of the plot on the left side.

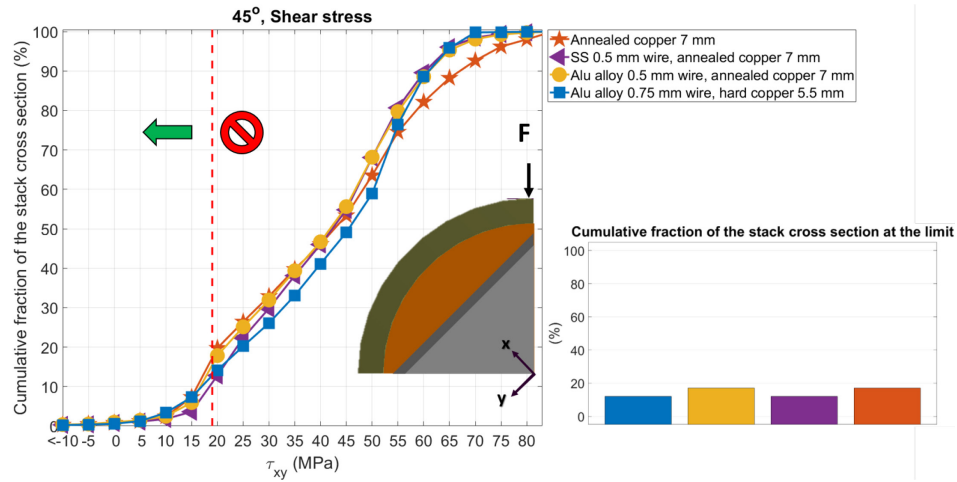


Figure 3:18 The cumulative of the fraction of the stack cross section vs the shear stress in the 45° orientation when the maximum force is applied, for different wire materials, wire and copper shell outer diameter. SS stands for stainless steel. The dashed red line represents the limiting value of shear stress for the tapes and it is taken from [25]. In all the scenario with a wire, the tension applied on the wire during the wrapping (before the cool down) is 30 N. In the bottom right corner, the cumulative fraction of the stack cross section at the limiting value of shear stress is shown for the various cases considered. The colour code is the same of the plot on the left side.

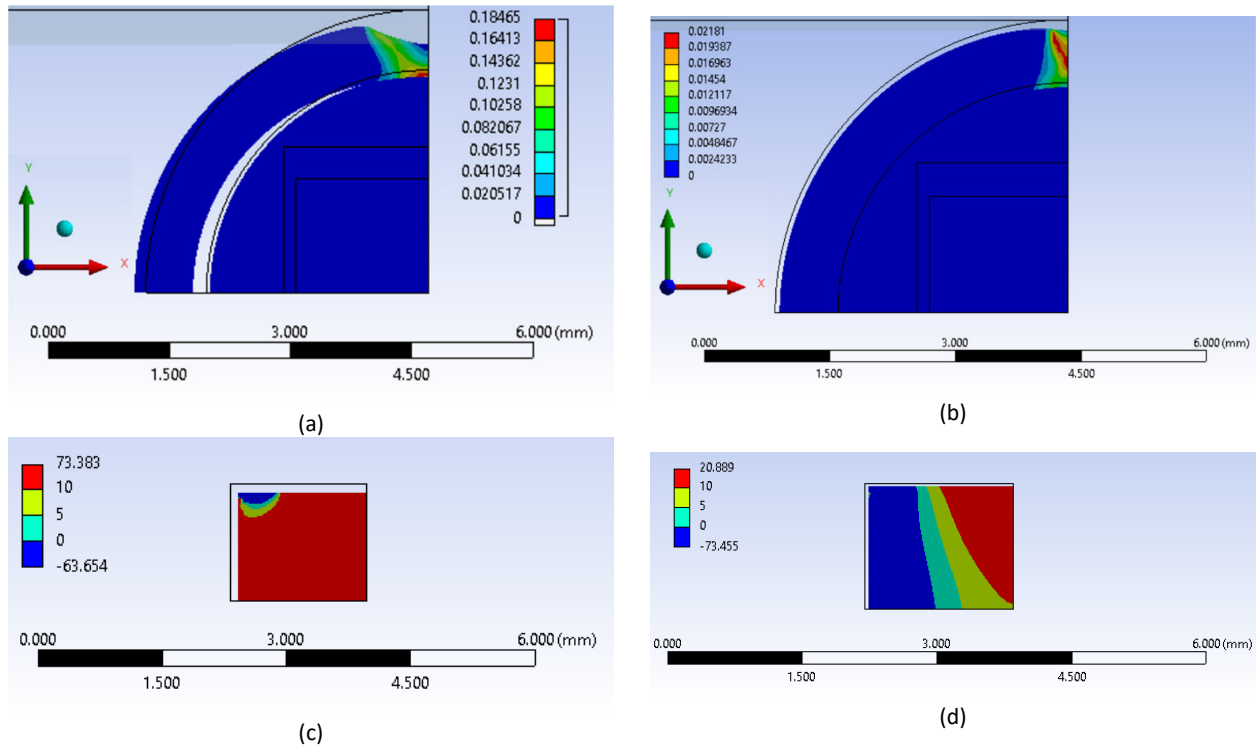


Figure 3:19 The plastic deformation in mm/mm in the wire and strand at the maximum force at 77 K in the case with 0.75 mm a) soft Alu alloy (100 MPa yield stress at 77 K) and b) with harder Alu alloy (324 MPa yield stress at 77 K). The undeformed wire shape (no pressure, RT) is shown (black line). The deformation is amplified 2.9 times. In figure a) it is possible to see that a gap opens. In c) the tension along the x axis in the stack in the case of soft Alu alloy wire, while in d) with the hard Alu alloy one, at the same temperature and force conditions of a) and b) picture.

The effect of the copper hardness is interesting (see Figure 3:20): the use of cold worked copper shells of 7 mm diameter, without wrapped wire, reduces the transverse stress in the stack cross section, but not in the range of interest (below 10 MPa). Instead, the transverse stress can be reduced by wrapping with a Alu wire (0.75 mm), with a reduced copper shell diameter (5.5 mm), see green line in Figure 3:20. If the soft copper is replaced by hard copper, the stack cross section exposed to a stress of >10 MPa is further reduced.

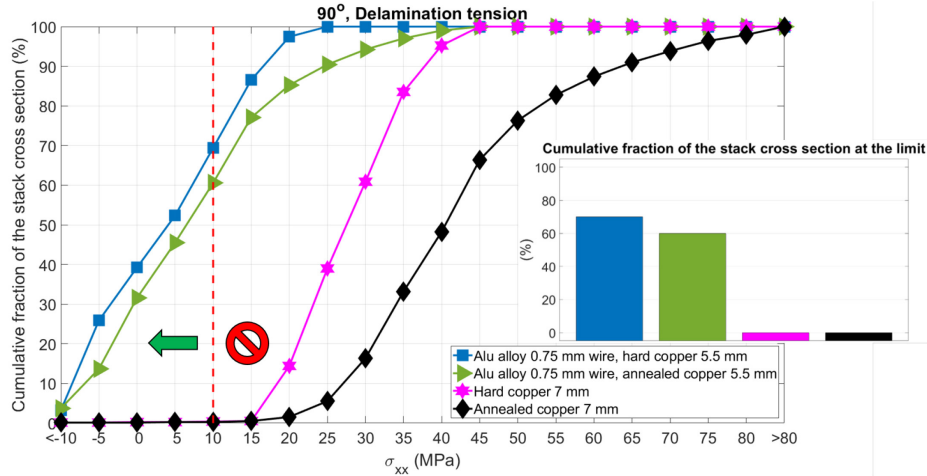


Figure 3:20 The cumulative of the fraction of the stack cross section vs the tensile strain along the x axis, in the 90° orientation exploring the effect of the annealing and the diameter of the copper shells and the wrapping of the strand with the Alu alloy wire. The dashed red line represents the limiting value of delamination tension for the tapes and it is taken from [25]. On the right, the cumulative fraction of the stack cross section at the limiting value of delamination tension is shown for the various cases considered. The colour code is the same of the plot on the left side.

3.4. Conclusions

The transverse pressure test was used as design decision tool for four cable designs proposed by SPC for the EU DEMO CS, to verify that the strands are able to withstand the operating Lorentz force. The transverse stress limits, the operational pressure values and the difference between the two for the various strands are summarised in Table 3:4. Out of the four strand designs, the 6 around 1 and the TSTS on the flat core passed the test, even if only by small margin. The beneficial effect of the solder filling, seen in the TSTC on the flat core, can be even more pronounced than what shown here, because it is supposed that the poorer performance of the edge case is due to local effect induced by the anvil print. It is postulated that the test could give a higher stress limit if the cable is fully enclosed in a jacket. Filling any void around the strands in the flat and round conductor may also be beneficial to reduce the strand deformation. However, the filling process should be carried out after coil winding, otherwise the peak tensile strain in the fully bonded scenario overcomes the 0.4 % of longitudinal tensile strain. In addition, a separate cooling channel should be included. It should be noted that solder filling in the case of the TSTS on the flat core, has two functions: to “immobilize” the stacks and to reduce the inter-tape resistance. In the case of the filling of a conductor made of round strands in which the stack is soldered, the solder filler has just a mechanical function.

Thanks to a mechanical analysis, design options were proposed to reduce the risk of the delamination of the stack in the soldered strand foreseen for the flat cable, without drastically changing the geometrical configuration. The radial precompression obtained during the cool down by difference in thermal contraction between Alu alloy and copper in the strands is beneficial, as it drastically reduces the transverse tensile stress that induces delamination.

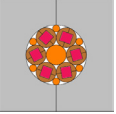
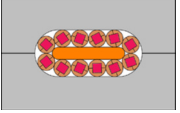

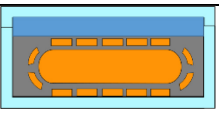
Cable design	Strand	Critical transverse stress (or load per unit)	Operational transverse stress (or load per unit length)	Difference between critical and operating values
 6 around 1	Cold-worked, Hard copper	60 MPa	48 MPa	12 MPa
 Copper-core Rutherford	Annealed, soft copper	15 MPa	23 MPa	-8 MPa
 Copper-core Rutherford	Reinforced+ not-soldered stack	133 kN/m	160 kN/m	-27 kN/m
 TSTS on a flat core	Solder-filled	24 MPa	19 MPa	5 MPa

Table 3:4 The list of the pressure limits and margin from the cable operating one for the different cable designed analysed.

Chapter 4 Conclusions

Reaching high magnetic field values in a pulsed tokamak like the EUROfusion DEMO can be beneficial both to reduce the Central Solenoid radius, thus reducing the overall size and cost of the machine, and to increase the generated magnetic flux, extending the plasma burn time, improving the power plant efficiency. REBCO coated conductors allow to generate fields beyond the Nb₃Sn limit of about 15-16 T. However, coated conductors are tapes with a strong mechanical anisotropy, preventing the transfer of cabling knowledge from LTS (round, isotropic wires) to HTS. At the SPC, so far the focus is on the Twisted Stack Tape Conductor concept.

An advantage of coated conductors is that they are stable against heat disturbances, because of the high temperature margin, reducing the likelihood of quench. Unfortunately, the low normal zone propagation velocity leads to a localized peak of the temperature. Since the normal zone propagates slowly, the total voltage rises slowly. If the current dump strategy is based on the voltage detection, the total voltage may reach the detection threshold already when the hot spot temperature is high enough to damage the conductor by thermal strain. The goal of the quench experiment in Chapter 2, was to understand how fast the temperature rises, as a function of the Twisted Stack Tape Conductor characteristics. The experiments show that the rate of the hot spot temperature increase is similar for the not-twisted and the twisted conductors (tens of K/s), while it is much slower for the solder filled conductor (in the order of K/s). A multi-physics model was built in THEA to simulate the experiments. It was possible to explain this difference in the temperature rising rate by the difference in thermal transverse resistance between jacket and cable, affirming the importance of this parameter for quench protection. The model has been used also to show that the short length of the uniform field in SULTAN does not allow the normal zone to propagate, at least when the quench is triggered by sending hot-helium in the conductor. It follows that the quench experiment in SULTAN cannot provide a relevant $V-T_{hot\ spot}$ characteristic for a case in which the magnetic field is uniform (large fusion magnet). Nevertheless, the Quench Experiment made possible to evaluate the hot spot evolution as function of the thermal transverse resistance between the jacket and cable. The experiment was extremely valuable to calibrate the model, which can be used to evaluate the voltage-temperature characteristic in more realistic conditions for a magnet. REBCO coated conductors can carry current till high temperature (60-70 K). As a consequence, the voltage rises very slowly (low current in the copper) but continuously (drift). The voltage threshold for a safe quench protection might be as low as 0.05 V, which is about half of the value considered for ITER. Nevertheless, it could be possible to measure at such low voltage by increasing the validation time. To confirm this, a study on the duration of the drift with respect to the energy deposited in the conductor and the cooling conditions is needed, together with the exponential current dump after the validation time.

In this thesis, different materials and cabling configurations were studied, to verify the strand endurance under transverse pressure, both experimentally and using a finite element mechanical model. It has been found that one of the key methods to increase the critical transverse pressure is to reduce the deformation of the stack, because stack deformation leads to shear stress and transverse tensile stress on the tapes, inducing delamination (and fracture) of the superconducting ceramic. Strand electromechanical tests in liquid nitrogen show that this could be done or by immobilizing the stack by solder filling or by using hard copper, which reduces the plastic deformation. The mechanical model indicates also a third way: the precompression obtained by the thermal shrinkage during the cool down of a wire (or a tube) wrapped around the soldered round strands. This reduces the fraction of the stack that is above the limiting tensile transverse tension on the stack. However, this concept does not help against the shear stress. The possibility of not soldering the tapes has been also considered: the tapes would be able to slide with respect to each other (stress-free) under the deformation. However, the transverse tests on a not-soldered strand wrapped by 0.5 mm stainless steel wire show that the high electrical thermal resistance between the tapes increases the scattering of the I_c . Therefore, this particular solution is not suitable. The results in this thesis indicate how to design a stronger strand, but a definitive proof will only be possible by the test of the full size conductor in relevant conditions, for example in the SULTAN facility.

Combining the conclusions of the thermal and mechanical analysis on HTS conductors, even though the solder filling brings clear advantages for the quench protection, the strands are fully bonded and they cannot slide during the winding process, leading to the maximum strain in the cable. A solution to this problem is to solder fill the cable after that the magnet is wound. The solder filling is adapt to other cable designs, like the TSTC on the flat core, presented in Chapter 3, were the strain is kept low because the tapes are already close to the neutral bending line.

Appendix A

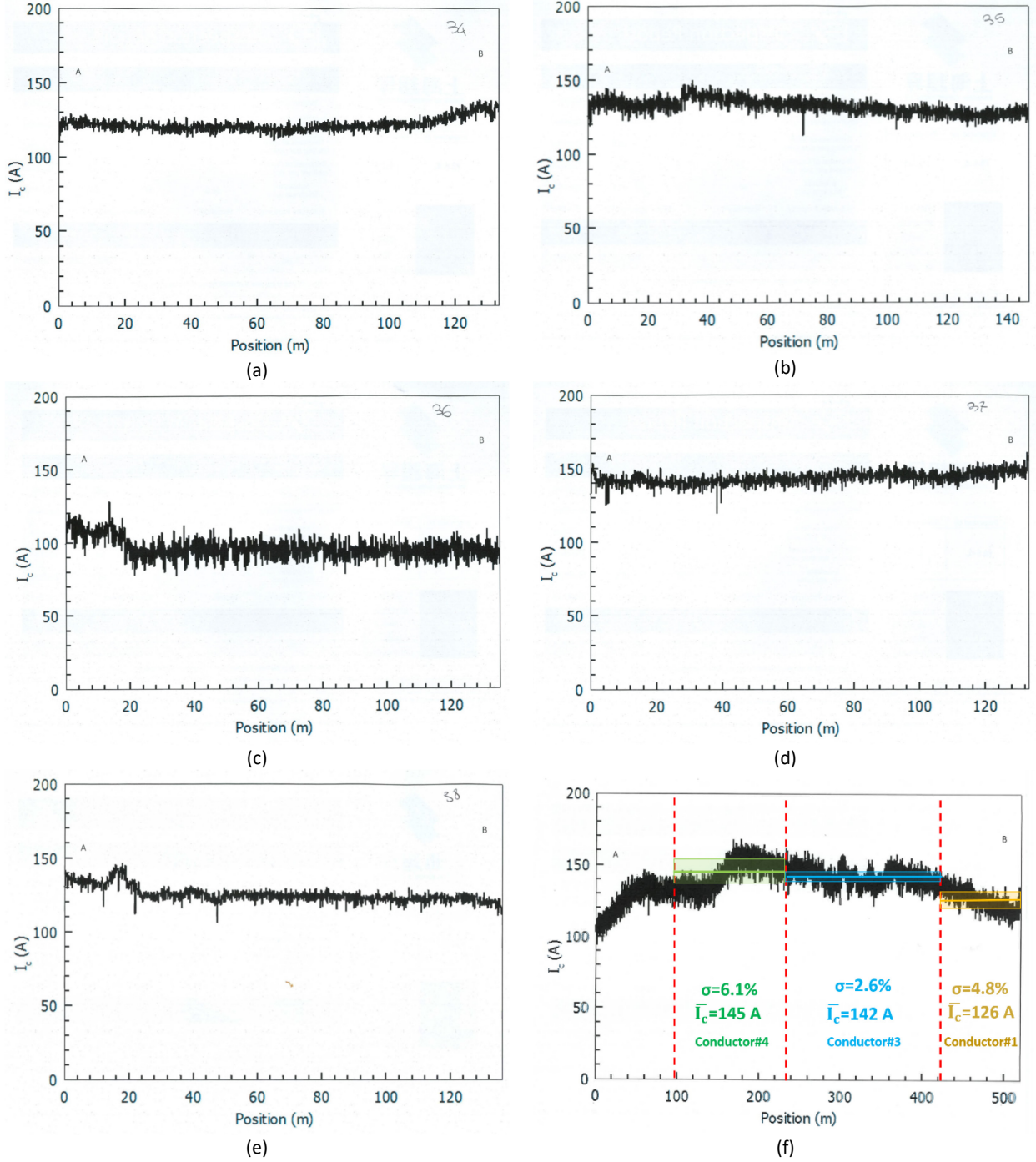


Figure A:0:1 The I_c along the length of the different REBCO spools, provided by the producer, used to manufacture the Quench Experiment conductors. The I_c is measured at 77 K, s.f.. a) spool #34, b) spool #35, c) spool #36, d) spool #37, e) spool #38, f) spool #39. Here, the length dedicated to each conductor is highlighted, together with the integral mean of the I_c and the standard variation.

References

- [1] Our World in Data, “Emissions by sector,” [Online]. Available: <https://ourworldindata.org/emissions-by-sector>.
- [2] IPCC, “Global Warming of 1.5 °C,” [Online]. Available: <https://www.ipcc.ch/sr15/>. [Accessed 2022].
- [3] Our World in Data, “How long before we run out of fossil fuels?,” [Online]. Available: <https://ourworldindata.org/how-long-before-we-run-out-of-fossil-fuels>. [Accessed 2022].
- [4] Working Group III of the Intergovernmental Panel on Climate Change, “IPCC Special Report on Carbon Dioxide Capture and Storage,” 2005.
- [5] J. P. Freidberg, “Plasma physics and fusion energy,” Cambridge University Press, Cambridge, 2007.
- [6] S. Tosti and C. Rizzello, “24 - Membranes for nuclear power applications,” *Advanced Membrane Science and Technology for Sustainable Energy and Environmental Applications*, pp. 769-791, 2011.
- [7] Yuhong Xu, “A general comparison between tokamak and stellarator plasmas,” *Matter and Radiation at Extremes*, vol. 192, 2016.
- [8] N. Mitchell and A. Devred, “The ITER magnet system: configuration and construction status,” *Fusion Engineering and Design*, vol. 123, no. 17-25, 2017.
- [9] P. Bruzzone, “Superconductivity and fusion energy—the inseparable companions,” *Superconductor Science and Technology*, vol. 28, 2014.
- [10] ITER, “THE ITER TOKAMAK,” [Online]. Available: <https://www.iter.org/mach>. [Accessed 10 1 2022].
- [11] Eurofusion. [Online]. Available: <https://www.euro-fusion.org/>. [Accessed 2022].
- [12] N. Mitchell et al., “Superconductors for fusion: a roadmap,” *Superconductor Science and Technology*, vol. 34, 2021.
- [13] T. Donné et al., “European Research Roadmap to the Realisation of Fusion Energy,” EUROfusion, Garching / Munich, Germany, 2018.
- [14] B. N. Sorbom et al., “ARC: A compact, high-field, fusion nuclear science facility and demonstration power plant with demountable magnets,” *Fusion Engineering and Design*, vol. 100, pp. 378-405, 2015.
- [15] V. Corato et al., “The DEMO magnet system – Status and future challenges,” *Fusion Engineering and Design*, vol. 174, 2022.
- [16] Y. Iwasa, *Case Studies in Superconducting Magnets*, New York, NY, USA: Springer, 2009.
- [17] C. Barth, *High temperature superconductor cable concepts for fusion magnets*, Karlsruhe (Germany): KIT Scientific Publishing, 2013.
- [18] J. van Nugteren, *High Temperature Superconductor Accelerator Magnets*, PhD thesis, University of Twente, The Netherlands, 2016.
- [19] E. Salazar et al., “Fiber optic quench detection for large-scale HTS magnets demonstrated on VIPER cable during high-fidelity testing at the SULTAN facility,” *Superconductor Science and Technology*, vol. 34, 2021.

- [20] R. Kang et al., "Detecting quench in HTS magnets with LTS wires -- a theoretical and numerical analysis," *Arxiv, Preprint*, 11 1 2022.
- [21] N. Bykovskiy et al., "Co-Wound Superconducting Wire for Quench Detection in Fusion Magnets," *IEEE Transactions on Applied Superconductivity*, vol. 32, no. 4, pp. 1-5, In press, 2022.
- [22] M. Marchevsky, "Quench Detection and Protection for High-Temperature Superconductor Accelerator Magnets," *Instruments*, vol. 5, 2021.
- [23] H. Hilgenkamp and J. Mannhart, "Grain boundaries in high-Tc superconductors," *Reviews of Modern Physics*, vol. 74, no. 2, pp. 485-549, 2002.
- [24] Y. L. Xu and D. Shi, "A Review of Coated Conductor Development," *Tsinghua Science and Technology*, vol. 8, no. 3, pp. 342-369, 2003.
- [25] H. Maeda et al., "Recent Developments in High-Temperature Superconducting Magnet Technology (Review)," *IEEE Transactions on Applied Superconductivity*, vol. 24, no. 3, 2014.
- [26] D. Uglietti et al., "Angular Dependence of Critical Current in Coated Conductors at 4.2 K and Magnet Design," *IEEE Transactions on Applied Superconductivity*, vol. 19, no. 3, pp. 2909-2912, 2009.
- [27] M. Takayasu et al., "HTS twisted stacked-tape cable conductor," *Superconductor Science and Technology*, vol. 25, 2011.
- [28] P. Bruzzone et al., "High temperature superconductors for fusion magnets," *Nuclear Fusion*, vol. 58, no. 10, 2018.
- [29] D. Uglietti, "A review of commercial high temperature superconducting materials for large magnets: from wires and tapes to cables and conductors," *Superconductor Science and Technology*, vol. 32, no. 5, 2019.
- [30] D. Uglietti et al., "Fabrication Trials of Round Strands Composed of Coated Conductor Tapes," *IEEE Transactions on Applied Superconductivity*, vol. 23, pp. 4802104-4802104, 2013.
- [31] N. Bykovsky, "HTS high current cable for fusion application," Switzerland, 2017.
- [32] N. Bykovsky et al., "Damage Investigations in the HTS Cable Prototype After the Cycling Test in EDIPO," *IEEE Transactions on Applied Superconductivity*, vol. 28, no. 4, 2018.
- [33] N. Bykovsky et al., "Performance evolution of 60 kA HTS cable prototypes in the EDIPO test facility," *Superconductor Science and Technology*, vol. 29, no. 084002, 2016.
- [34] N. Bykovsky et al., "Design Optimization of Round Strands Made by Twisted Stacks of HTS Tapes," *IEEE Trans. Appl. Supercond.*, vol. 26, no. 2, pp. 1-7, March 2016.
- [35] R. Wesche et al., "DEMO central solenoid design based on the use of HTS sections at highest magnetic field," *IEEE Trans. Appl. Supercond.*, vol. 28, no. 3, Apr. 2018.
- [36] M. J. Wolf et al., "HTS CroCo: A Stacked HTS Conductor Optimized for High Currents and Long-Length Production," *IEEE Transactions on Applied Superconductivity*, vol. 26, pp. 19-24, 2016.
- [37] G. Celentano et al., "Design of an Industrially Feasible Twisted-Stack HTS Cable-in-Conduit Conductor for Fusion Application," *IEEE Transactions on Applied Superconductivity*, vol. 24, pp. 1-5, 2014.
- [38] A. Augieri et al., "Electrical Characterization of ENEA High Temperature Superconducting Cable," *IEEE Transactions on Applied Superconductivity*, vol. 25, pp. 1-4, 2015.

- [39] D. Uglietti et al., "Test of 60 kA coated conductor cable prototypes for fusion magnets," *Superconductor Science and Technology*, vol. 28, no. 12, 2015.
- [40] D. Uglietti et al., "Design and Strand Tests of a Fusion Cable Composed of Coated Conductor Tapes," *IEEE Transactions on Applied Superconductivity*, vol. 24, no. 3, pp. 1-4, 2014.
- [41] R. Kang et al., "Quench Simulation of REBCO Cable-in-Conduit Conductor With Twisted Stacked-Tape Cable," *IEEE Transactions on Applied Superconductivity*, pp. 1-7, Jan. 2020.
- [42] A. Zappatore et al., "A new model for the analysis of quench in HTS cable-in-conduit conductors based on the twisted-stacked-tape cable concept for fusion applications," *Superconductor Science and Technology*, vol. 33, no. 6, May 2020.
- [43] A. Zappatore et al., "Modeling Quench Propagation in the ENEA HTS Cable-In-Conduit Conductor," *IEEE Trans. Appl. Supercond.*, vol. 30, no. 8, pp. 1-7, Dec. 2020.
- [44] M. Lewandowska et al., "Thermal-hydraulic analysis of an HTS DEMO TF coil," *Cryogenics*, vol. 96, pp. 125-132, Dec. 2018.
- [45] R. Heller et al., "Conceptual Design Improvement of a Toroidal Field Coil for EU DEMO Using High-Temperature Superconductors," *IEEE Trans. Appl. Supercond.*, vol. 26, pp. 1-5, 2016.
- [46] N. Yanagi et al., "Magnet design with 100-kA HTS STARS conductors for the helical fusion reactor," *Cryogenics*, vol. 80, pp. 243-249, 2016.
- [47] J. Van Nugteren et al., "Measurement and Analysis of Normal Zone Propagation in a ReBCO Coated Conductor at Temperatures Below 50 K," *Physics Procedia*, vol. 67, pp. 945-951, 2015.
- [48] J. Van Nugteren et al., "Toward REBCO 20 T+ Dipoles for Accelerators," *IEEE Transactions on Applied Superconductivity*, vol. 28, no. 4, pp. 1-9, June 2018.
- [49] A. Anghel, "The quench experiment on long length cable-in-conduit conductor (QUELL) in SULTAN," *Journal of Fusion Energy*, vol. 14, no. 1, p. 129-139, March 1995.
- [50] Z. S. Hartwig et al., "VIPER: an industrially scalable high-current high-temperature superconductor cable," *Supercond. Sci. Technol.*, vol. 33, no. 11, 2020.
- [51] O. Dicuonzo et al., "Upgrade and Commissioning of the SULTAN Facility to Host Quench Experiments on HTS High Current Conductors," *IEEE Transactions on Applied Superconductivity*, vol. 31, no. 5, pp. 1-5, 2021.
- [52] P. Bauer, "Review of material properties, past experiences, procedures, issues and results for a possible solder filled cable as Plan B conductor for the EFDA dipole magnet (Draft Vs 1)," 2007.
- [53] "Lake Shore Cryotronics," [Online]. Available: <https://www.lakeshore.com/products/categories/overview/temperature-products/cryogenic-temperature-sensors/cernox>. [Accessed 19 Oct. 2020].
- [54] "Swagelok," [Online]. Available: <https://www.swagelok.com/en/catalog/Fittings>. [Accessed 19 Oct. 2020].
- [55] K. J. Binns, P. J. Lawrenson and C. W. Trowbridge, *The analytical and numerical solution of electric and magnetic fields*, Wiley, 1993.
- [56] S. Wimbush, "A public database of high-temperature superconductor critical current data, . 27 (2017) 8000105.," *IEEE Trans. Appl. Supercond.*, vol. 27, pp. 1-5, 2017.

- [57] CryoSoft, "Solid Materials Database," CryoSoft, [Online]. Available: <https://supermagnet.sourceforge.io/solids.html>. [Accessed 3 2021].
- [58] N. Bagrets et al., "Low Temperature Thermal and Thermo-Mechanical Properties of Soft Solders for Superconducting Applications," *IEEE Transactions on Applied Superconductivity*, vol. 24, pp. 1-3, June 2014.
- [59] X. Wang et al., "Near-adiabatic quench experiments on short YBa₂Cu₃O_{7-δ} coated conductors," *J. Appl. Phys.*, vol. 101, p. 5, 2007.
- [60] X. Sarasola et al., "Progress in the Design of a Hybrid HTS-Nb₃Sn-NbTi Central Solenoid for the EU DEMO," *IEEE Trans. Appl. Supercond.*, vol. 30, no. 4, pp. 1-5, June 2020.
- [61] CryoSoft, "Thermal, hydraulic and electric analysis of superconducting cables," 2021. [Online]. Available: https://supermagnet.sourceforge.io/manuals/Thea_2.4.pdf.
- [62] L. Bottura et al., "A General Model For Thermal, Hydraulic and Electric Analysis of Superconducting Cables," *Cryogenics*, vol. 40, pp. 617-626, 2000.
- [63] R. Kang et al., "Modelling quench of a 50 kA REBCO conductor with soldered-twisted-stacked-tape-cable strands," *Cryogenics*, vol. 106, 2020.
- [64] L. Bottura, "Heat Transfer Correlations," CryoSoft Internal Note CRY0/98/010, 1998.
- [65] L. Bottura, "Friction Factor Correlations," CryoSoft Internal Note CRY0/98/009, 1998.
- [66] K. Sedlak et al., "Results and analysis of the hot-spot temperature experiment for a cable-in-conduit conductor with thick conduit," *Cryogenics*, vol. 72, pp. 9-13, 2015.
- [67] M. Bonura and C. Senatore, "An equation for the quench propagation velocity valid for high field magnet use of REBCO coated conductors," *Appl. Phys. Lett.*, vol. 108, 2016.
- [68] N. Bykovsky et al., "Cyclic load effect on round strands made by twisted stacks of HTS tapes," *Fusion Engineering and Design*, vol. 124, pp. 6-9, 2017.
- [69] B. J. a. G. Pasztor, "Fabrication of high current Nb₃Sn forced flow conductors and coils for the SULTAN III test facility," *Fusion Technology*, pp. 872-876, 1993.
- [70] ANSYS Mechanical, "<https://www.ansys.com/products/structures/ansys-mechanical>," [Online].
- [71] Robert J. Corruccini and John J. Gniewek, Thermal Expansion of Technical Solids at Low Temperatures, A Compilation From the Literature, 1961.
- [72] Nathaniel C. Allen et al., "Structural Finite Element Evaluation of Twisted Stacked-Tape Cables for High-Field Magnets," *IEEE Trans. Appl. Supercond.*, vol. 27, 2017.
- [73] Copper Development association Inc., "Low temperature properties of copper and copper alloys".
- [74] Shanghai Superconductor Technology. [Online]. Available: <http://www.shsctec.com/en/index>. [Accessed 11 Oct. 2020].

Curriculum Vitae

Ortensia
Dicuonzo

Address: Stadtbachstrasse 9
5400 Baden
Switzerland
Phone: +41784061646
Email: ortensiadicuonzo@gmail.com



Education & Work Experience

2017 – P.T. **PhD in Physics** "Electromechanical investigations and quench experiments on sub-size HTS cables for high field EU-DEMO Central Solenoid" under supervision of Davide Uglietti and Ambrogio Fasoli at EPFL – Swiss Plasma Center, Lausanne, Switzerland. Exam date: 10/03/2022.

2017 **Apprenticeship in Radiation Protection**. Alpha spectrometry with silicon detectors, at U-Series, Bologna, Italy.

2014 – 2016 **MSc in Energy and Nuclear Engineering – Nuclear Technologies and Applications**. Master thesis: "Simulations of experimental measurements in the TAPIRO reactor by Monte Carlo and deterministic methods" under supervision of Sandra Dulla and Piero Ravetto at Politecnico di Torino, Torino, Italy. Score: 110/110 and honors.

Skills & Knowledge

Experimental:	<ul style="list-style-type: none">• $I_c(B, T)$ measurements: 4 points probe at cryogenic conditions (liquid helium and nitrogen).• Transverse pressure test.• Quench Experiment in high field on HTS cables.• Manufacturing of soldered twisted stack of tapes strands.
Numerical:	<ul style="list-style-type: none">• I_c and T_{cs} performance assessment.• Mechanical Finite Element analysis• Quench simulations• Reduction of large datasets• Parametric analysis
Programming:	<ul style="list-style-type: none">• MATLAB (Advanced)• Fortran (intermediate)• Ansys Workbench-Static structural (intermediate)• THEA (intermediate)• Office (intermediate)
Languages	<ul style="list-style-type: none">• Italian (native)• English (advanced)• German (intermediate)

References

Dr. Davide Uglietti

Senior scientist at the superconductivity group at
Swiss Plasma Center (EPFL)
5232 Villigen-PSI, Switzerland
Davide.uglietti@psi.ch

Prof. Ambrogio Fasoli

Director of Swiss Plasma Center (EPFL)
1015 Lausanne, Switzerland
Ambrogio.fasoli@psi.ch

Publications

- [1] V. Corato *et al.*, "The DEMO magnet system – Status and future challenges," *Fusion Engineering and Design*, vol. 174, Jan. 2022, Art. No. 112971, doi: 10.1016/j.fusengdes.2021.112971.
- [2] O. Dicuonzo *et al.*, "Upgrade and Commissioning of the SULTAN Facility to Host Quench Experiments on HTS High Current Conductors," *IEEE Transactions on Applied Superconductivity*, vol. 31, no. 5, pp. 1-5, Aug. 2021, Art no. 9500505, doi: 10.1109/TASC.2021.3063997.
- [3] K Sedlak *et al.*, "Advance in the conceptual design of the European DEMO magnet system," *Superconductor Science and Technology*, vol. 33, Feb. 2020, Art. no. 044013
- [4] R. Wesche *et al.*, "Hybrid HTS-Nb₃Sn-NbTi DEMO CS coil design optimized for maximum magnetic flux generation," *Fusion Engineering and Design*, vol. 146, Part A, 2019, pp 10-13, doi: /10.1016/j.fusengdes.2018.10.027.
- [4] R. Zanino *et al.*, "Development of a Thermal-Hydraulic Model for the European DEMO TF Coil," *IEEE Transactions on Applied Superconductivity*, vol. 26, no. 3, pp. 1-6, April 2016, Art no. 4201606, doi: 10.1109/TASC.2016.2523241.